Coupling measurement of the Higgs boson and search for heavy Higgs like bosons via the decay channel $H \to WW^{(*)} \to \ell\nu\ell\nu$ with the ATLAS experiment.

Dissertation der Fakultät für Physik
der Ludwig-Maximilians-Universität München

vorgelegt von
Christian Meineck
geboren in Neuburg an der Donau
München, 11. November 2014

Erstgutachter: PD Dr. Johannes Elmsheuser
Zweitgutachter: Prof. Dr. Martin Faessler
Tag der mündlichen Prüfung: 18. Dezember 2014

"I like to imagine that God has a giant computer - controlled factory, which takes Lagrangians as input and delivers the universe they represent as output. Usually God's computer has no difficulty - when you feed in the Maxwell Lagrangian, Equation 10.35, for example, it immediately creates an electromagnetic universe of interacting electrons, positrons, and photons. Sometimes it takes a little longer - the Lagrangian in Equation 10.105, for instance, confuses it at first, until it deciphers the 'hidden' mass term. And occasionally it returns an error message: 'this Lagrangian does not describe a possible universe; please check for syntax errors or incorrect signs'. That's what it would do for example, if you fed it the Lagrangian in Equation 10.108 without the λ term."

David Griffiths

Zusammenfassung

Diese Arbeit präsentiert zwei Analysen des Zerfallskanals $H \to WW^{(*)} \to \ell\nu\ell\nu$ mit den Daten des ATLAS experiments am LHC. Die analysierten Daten wurden im Jahr 2011 bzw. 2012 bei einer Schwerpunktsenergie von $\sqrt{s} = 7\,\text{TeV}$ bzw. $8\,\text{TeV}$ aufgezeichnet und es wurde eine integrierte Luminosität von $25\,\text{fb}^{-1}$ erreicht. Die beiden Analysen unterscheiden sich im analysierten Phasenraum, der von der Massen m_H des Higgs boson Signals abhängt. Die Analyse für Massen $m_\text{H} < 200\,\text{GeV}$ wurde über die letzten Jahre optimiert, um in der Lage zu sein, eine Präzisions Messung der Kopplungen einer Resonanz bei $m_\text{H} \approx 125\,\text{GeV}$ durchzuführen. Dabei wird ein Likelihood Fit der transversalen Masse $m_\text{T} = \sqrt{(E_T^{\ell\ell} + P_T^{\nu\nu})^2 - |\vec{P_T^{\ell\ell}} + \vec{P_T^{\nu\nu}}|^2}$ angewendet. Mit einer statistischen Signifikanz von 6.1σ konnte ein $H \to WW^{(*)} \to \ell\nu\ell\nu$ Signal bei einer Masse $m_\text{H} = 125.36 \pm 0.41\,\text{GeV}$ beobachtet werden. Die Messung der Signalstärke, dem Verhältniss von experimentell bestimmtem Produktionswirkungsquerschnitt mal Verzweigungsverhältnis zur theoretischen Prognose, ergab folgenden Wert:

$$\mu = 1.08\,^{+0.16}_{+0.15}(\text{stat.})\,^{+0.16}_{-0.14}(\text{syst.}),$$

was im Einklang mit der Standard-Modell-Vorhersage steht. Die Skalierung der Kopplungen des Higgs bosons an Fermionen und Bosonen wurden bestimmt zu:

$$\kappa_F = 0.92\,^{+0.30}_{-0.23}$$
$$\kappa_V = 1.04\,^{+0.10}_{-0.11}.$$

Zur Suche nach schweren, Higgs boson artigen Teilchen wurde die Analyse des $H \to WW^{(*)} \to \ell\nu\ell\nu$ Zerfallskanals für Massen $m_\text{H} > 200\,\text{GeV}$ optimiert. Auch im hohen Massenbereich wird ein Likelihood Fit an der Verteilung der transversalen Masse m_T durchgeführt. Es wurden obere Grenzen auf Produktionswirkungsquerschnitt mal Verzweigungsverhältnis für drei Szenarien bestimmt: Standard-Model-Higgs-Boson im Massenbereich $200 \leq m_\text{H} \leq 1\,\text{TeV}$, Higgs boson artige Resonanz mit einer Zerfallsbreite von $1\,\text{GeV}$ im Massenbereich $200 \leq m_\text{H} \leq 2\,\text{TeV}$ und das elektroschwache Singlet Szenario im Massenbereich $200 \leq m_\text{H} \leq 1\,\text{TeV}$, bei dem die Zerfallsbreite zusätzlich zur Masse variiert wird. Es konnte in keinem getesteten Szenario ein statistisch signifikanter Datenüberschuss beobachtet werden und darüberhinaus konnte ein Standard Modell artiges Higgs Boson bis zu einer Masse von $m_\text{H} = 661\,\text{GeV}$ ausgeschlossen werden.

Abstract

Two analyses of the decay channel $H \to WW^{(*)} \to \ell\nu\ell\nu$ using the data of the ATLAS experiment at LHC are presented here. The data was recorded in the years 2011 and 2012 with a center of mass energy of $\sqrt{s} = 7\,\text{TeV}$ and $8\,\text{TeV}$, respectively, with a total integrated luminosity of $25\,\text{fb}^{-1}$ reached. The two presented analyses differ in the analyzed phase space, which depends on the mass m_H of the analyzed Higgs boson signal. The analysis for masses $m_\text{H} < 200\,\text{GeV}$ is optimized to perform a high precision measurement of the couplings of the resonance at $m_\text{H} \approx 125\,\text{GeV}$. A binned likelihood fit of the transverse mass distribution $m_\text{T} = \sqrt{(E_T^{\ell\ell} + P_T^{\nu\nu})^2 - |\vec{P}_T^{\ell\ell} + \vec{P}_T^{\nu\nu}|^2}$ is used to obtain the results. A signal originating from a Standard Model Higgs boson with a mass $m_\text{H} = 125.36 \pm 0.41\,\text{GeV}$ has been observed at a statistical significance of 6.1σ. The signal strength, defined as the ratio of the measured production cross section times branching ratio over the theoretical prediction, is:

$$\mu = 1.08\,^{+0.16}_{+0.15}(\text{stat.})\,^{+0.16}_{-0.14}(\text{syst.}),$$

which is in good agreement with the data and with the Standard Model prediction. The scaling factors of the couplings of the Higgs boson to fermions and bosons have been measured as:

$$\kappa_F = 0.92\,^{+0.30}_{-0.23}$$
$$\kappa_V = 1.04\,^{+0.10}_{-0.11},$$

which is also in good agreement with the Standard Model prediction. In order to search for heavier Higgs like particles, the analysis of $H \to WW^{(*)} \to \ell\nu\ell\nu$ decays is also optimized for masses $m_\text{H} \geq 200\,\text{GeV}$. As in the analysis optimized for $m_\text{H} < 200\,\text{GeV}$, a binned likelihood fit of the transverse mass m_T is used. Upper limits on the product of production cross section and branching ratio have been obtained for three scenarios: Standard Model Higgs boson in the mass range $200 \leq m_\text{H} \leq 1\,\text{TeV}$, a Higgs like particle with a decay width of $1\,\text{GeV}$ in the mass range $200 \leq m_\text{H} \leq 2\,\text{TeV}$ and the electroweak singlet scenario in the mass range $200 \leq m_\text{H} \leq 1\,\text{TeV}$ with the decay width being an additional free parameter. No statistically significant excess of the observed data over the expectation is observed, and a heavy Standard Model Higgs boson is excluded up to a mass of $m_\text{H} = 661\,\text{GeV}$.

Contents

1. Introduction

The Higgs boson was the last missing particle of the Standard Model of particle physics for a long time. In July 2012, both the ATLAS [1] and CMS [2] collaboration reported about the observation of a new resonance at roughly 125 GeV with a statistical significance of five standard deviations. Since then, the properties such as spin [3] [4], mass [5] [6] and the couplings [7] [6] of this resonance have been measured and to this day all measurements are in good agreement with the prediction of the Standard Model. The resonance seems to be a scalar particle which couples to the other particles described by the Standard Model proportional to their masses. The mass of the particle has been precisely measured to $m_{\mathrm{H}} = 125.36 \pm 0.41\,\mathrm{GeV}$ [5].

The Higgs boson is dominantly produced at hadron colliders via the gluon-gluon fusion process at which gluons interact via a top-quark loop to produce a resonant Higgs boson. Furthermore, the Higgs boson can be produced via the fusion of vector bosons which are predominantly radiated by interacting quarks and in association with a W or a Z boson. The decay of the Higgs boson in two W bosons which subsequently decay into a lepton neutrino pair, provides a sensitive experimental signature in order to exploit its properties. The branching ratio for a Higgs boson with unknown mass to decay into a W boson pair is the dominant decay channel for Higgs boson masses $m_{\mathrm{H}} > 140\,\mathrm{GeV}$ hence this decay channel can be used to search for heavier Higgs-like particles.

This thesis focuses on the analysis of the decay channel $H \to WW^{(*)} \to \ell\nu\ell\nu$ with the ATLAS experiment in order to exploit the couplings of the 125.36 GeV resonance and to search for heavier Higgs-like particles, which could be utilized to extend the Standard Model of particle physics. The Standard Model can not be complete since it does not provide answers to fundamental questions such as the origin of the masses of neutrinos, the origin and nature of dark matter, the striking mass difference of the elementary particles, just to mention a few examples. Searching for a second Higgs like particle and measuring the couplings of the Higgs boson with high precision can help to further develop and fine tune the theory.

The outline of this work is as follows: in chapter 2 the theoretical framework of particle physics, known as the Standard Model is introduced briefly. Chapter 3 provides an overview about the LHC and the functionality of the ATLAS detector. Followed by this, the datasets used in this thesis are introduced in chapter 4. In chapter 5, the definitions of the reconstructed physics objects such as electrons, muons, missing transverse energy

and jets are introduced. In order to separate the $H \to WW^{(*)} \to \ell\nu\ell\nu$ signal process from various Standard Model background process, cuts on various kinematical variables are applied. The kinematical variables as well as the selection criteria are presented in chapter 6. One crucial aspect in the data analysis is a precise understanding and estimation of the various background processes which can create a detector signature similar to $H \to WW^{(*)} \to \ell\nu\ell\nu$ events. In chapter 7 those background processes as well as their data driven estimation is discussed. Systematic uncertainties arising from detector effects as well as from theoretical calculations are introduced in chapter 8. In order to perform measurements, a proper statistical treatment of the observed data is crucial. This statistical procedure is discussed in chapter 9 and in chapter 10 and 11 the results of it will be presented. The thesis closes with a conclusion and a short outlook in chapter 12.

Part I.

Theory and Experiment

2. Theoretical background

This chapter provides a brief overview of the theoretical framework of this thesis. First of all, the known particle content as well as three fundamental forces will be introduced. Furthermore, the mechanism of the dynamic electroweak symmetry breaking as well as the couplings of the Higgs boson are discussed. The proton as a compound state and the hadronization of quarks resulting from a hard scattering process is introduced and at the end of the chapter some possible extension of the very successful Standard Model will be discussed.

2.1. The Standard Model of particle physics

The Standard Model (SM) of particle physics is the theoretical framework which helps us to understand the interactions between sub-atomic particles. The theory was developed in the 1960s and 1970s [8], [9], [10], [11], [12] and stands for *the theory* of particle physics [13]. It is the result of the interplay between experimental data and mathematical concepts like group theory, quantum field theory, gauge invariance and the ideas of the general theory of relativity [14]. The big success of the Standard Model is based on the fact that it provided a range of predictions (like the Z^0-boson, top quark or the Higgs boson) which have been verified in particle accelerator experiments like LEP, TeVatron or the LHC.

The language of the Standard Model is the quantum field theory. Similar to classical mechanics one can describe a system of single or multiple mass points using the Lagrange density, fields $\phi_i(\vec{x}, t)$ are used instead of simple space-time coordinates. The Lagrange density of a single scalar (spin-0) field can be written as

$$\mathscr{L} = \frac{1}{2}(\partial_\mu \phi)(\partial^\mu \phi) - \frac{1}{2}m^2\phi^2 \tag{2.1}$$

Applying the Euler-Lagrange equations one can obtain the Klein-Gordon equation

$$\partial_\mu \partial^\mu \phi = m^2 \phi \tag{2.2}$$

which then can be used to obtain the equations of motion for a spin-0 field.

The Standard Model of particles physics provides a modern understanding of the electromagnetic, weak and strong interactions of all known subatomic particles. The three interactions are described by the exchange of spin-1 bosons amongst spin-$\frac{1}{2}$ particles with a certain coupling strength. The central attribute of the Standard Model (SM) is the local gauge invariance with respect to the gauge group $SU(3)_C \times SU(2)_L \times U(1)_Y$. The specific gauge bosons associated with the generators of the algebra of the group are [13]:

> $SU(3)_C \rightarrow 8\, G_\mu^\alpha$ with $\alpha = 1, ..., 8$. The eight massless, spin-1 *gluons*. The subscript C indicates the presence of *color* charges.
>
> $SU(2)_L \rightarrow 3\, W_\mu^a$ with $a = 1, 2, 3$ three spin-1 bosons. The subscript L reflects that only left handed fermions and right handed anti fermions participate in the interaction.
>
> $U(1)_Y \rightarrow B_\mu$ a spin-1 boson. The subscript Y abbreviates the coupling of the boson of this part of the gauge group to fermions which carry the so called *weak hypercharge* Y as a quantum number [13].

The gravity as the fourth fundamental interaction is not covered by the Standard Model hence the SM cannot be considered as complete.

Strong force
The strong force is described by the gauge group $SU(3)_C$. The index C indicates that the interaction of the strong force happens via the coupling to color charged particles where each color charged fermion has one of the three possible values (red, green or blue). Those color charged fermions are known as the six massive quarks: u, d, s, c, b and t. The gluons, which are considered as spin-1 bosons, are assumed to be massless, electrically neutral and color charged which has been in agreement with all experimental data so far. They always carry a color and an anti color for example the tuple $(red, \overline{blue})$. So far free quarks have not been observed in nature, they have been only seen in bound, color neutral states called mesons (one quark and one anti quark) or baryons (three quarks) which form together the family of hadrons. The strong force keeps the building blocks of nucleons of everyday atoms together, for example, a proton is a bound state of two up-quarks u and one down-quark d. Since quarks appear only in bound states, they leave a special signature in the detector, the so called Jets (see sections 2.3, 3.3.3 & 5.3).

Electroweak force
The gauge group $SU(2)_L \times U(1)_Y$ describes the electroweak force, while the name *electroweak* is based on the fact that from the theoretical point of view this force is the unification of the weak and the electromagnetic force. The theory of electroweak inter-

actions introduces four bosons as exchange particles. Namely the three massive spin-1 bosons Z^0, W^- and W^+ and one massless spin-1 boson, the photon γ. One naive way of distinguishing between the electromagnetic and the weak part of the electroweak force is looking at which charges the exchange bosons couple to. The photon, as the force carrier of the electromagnetic force, couples to the electric charge $q_{el.}$ whereas the three weak force carriers couple to the so called weak hypercharge Y_W. Applying the Gell Mann Nishijima formula [15], [16] one can calculate Y_W for each fermion via their electric charge $q_{el.}$ and the third component of the isospin I_3

$$Y_W = 2(q_{el.} - I_3).$$

Particles taking part in this interaction are the quark fields introduced earlier and the leptons fields which both form isospin doublets. The up-type quarks ($I_3 = +\frac{1}{2}$) (u, c, t) carry an electric charge of $+\frac{2}{3}$ and the down-type quarks (d, s, b) ($I_3 = -\frac{1}{2}$) carry an electric charge of $-\frac{1}{3}$. The second set of isospin doublets taking part in the electroweak interactions are the the three leptons and the three neutrinos. The three leptons ($I_3 = -\frac{1}{2}$) which carry an electric charge of -1 are the electron e, the muon μ and the tauon τ and the three neutrinos ($I_3 = +\frac{1}{2}$) which are electrically neutral: the electron neutrino ν_e, the muon neutrino ν_μ and the tau neutrino ν_τ. All of the leptons and neutrinos do not carry any color charge therefore they do not interact strongly. As mentioned earlier, only left handed fermions and right handed anti fermions participate in the electroweak interaction.
Since the physical properties of the fermions differ only by their masses[1] one usually arranges the twelve fermionic quantum fields[2] in three generations. Table 2.1 summarizes all known spin-$\frac{1}{2}$ particles of the Standard Model. The masses of quarks and leptons are taken from Ref. [17].

	first generation	second generation	third generation
quarks	$m = 2.7^{+0.7}_{-0.5}\,\mathrm{MeV}$ u	$m = 1.275 \pm 0.025\,\mathrm{GeV}$ c	$m = 173.2 \pm 0.9\,\mathrm{GeV}$ t
	$q_{\mathrm{el.}} = +\frac{2}{3}e$ up-quark	$q_{\mathrm{el.}} = +\frac{2}{3}e$ charm-quark	$q_{\mathrm{el.}} = +\frac{2}{3}e$ top-quark
	$m = 4.8^{+0.7}_{-0.3}\,\mathrm{MeV}$ d	$m = 95 \pm 5\,\mathrm{MeV}$ s	$m = 4.18 \pm 0.03\,\mathrm{GeV}$ b
	$q_{\mathrm{el.}} = -\frac{1}{3}e$ down-quark	$q_{\mathrm{el.}} = -\frac{1}{3}e$ strange-quark	$q_{\mathrm{el.}} = -\frac{1}{3}e$ bottom-quark
leptons	$m < 2\,\mathrm{eV}$ ν_e	$m < 190\,\mathrm{keV}$ ν_μ	$m < 18.2\,\mathrm{MeV}$ ν_τ
	$q_{\mathrm{el.}} = 0$ electron-neutrino	$q_{\mathrm{el.}} = 0$ muon-neutrino	$q_{\mathrm{el.}} = 0$ tau-neutrino
	$m = 0.511 \pm 11 \cdot 11^{-9}\,\mathrm{MeV}$ e	$m = 105.66 \pm 3.5 \cdot 10^{-6}\,\mathrm{MeV}$ μ	$m = 1776.82 \pm 0.16\,\mathrm{MeV}$ τ
	$q_{\mathrm{el.}} = -1e$ electron	$q_{\mathrm{el.}} = -1e$ muon	$q_{\mathrm{el.}} = -1e$ tauon

Table 2.1.: The Table summarizes all known fermionic particles with a spin of $\frac{1}{2}$. The upper two rows show the color charged quark fields, the lower two rows show the color neutral leptons. All those particles are known to be massive.

[1] For particles with identical charges.
[2] Actually, there are $6 + 18 = 24$ fields. Each quark can carry one of the three color charges.

The mass increases with the generation and can vary by several orders of magnitudes: $\frac{m_{\text{top-quark}}}{m_{\text{up-quark}}} \approx 75{\cdot}10^3$. As mentioned earlier, forces are mediated by vector (= spin-1) bosons. The force carrier particles are summarized in Table 2.2. The Higgs boson (the excitation of the Higgs-background field) is also presented there, which is a scalar particle hence it is supposed to be a spin-0 boson. The masses of the force carrier particles are taken from Ref. [17] and the mass of the Higgs boson is taken from Ref. [5]. The Higgs boson or rather its source will be discussed in the next section.

$m < 1 \cdot 10^{-18}\,\text{ev}$	γ
$q_{\text{el.}} < 1 \cdot 10^{-35} e$	Photon
$m = 91.1876 \pm 0.0021\,\text{GeV}$	Z^0
$q_{\text{el.}} = 0$	Z-boson
$m = 80.385 \pm 0.0015\,\text{GeV}$	$W^{\pm}$
$q_{\text{el.}} = \pm 1e$	W-boson
$m = 0$	g
$q_{\text{el.}} = 0$	gluon
$m = 125.36 \pm 0.41\,\text{GeV}$	H
$q_{\text{el.}} = 0$	Higgs boson

Table 2.2.: In this Table all known force carrier particles are listed together with their masses and electrical charges. Those particles are bosons with spin-1. Also the Higgs boson, a spin-0 particle, is presented here and will be discussed in see section 2.2).

Taking into account the fermionic particle content as well as the discussed forces and the *Brout-Englert-Higgs* mechanism (see section 2.2), the full Standard Model Lagrange

density can be written as:

$$\begin{aligned}\mathscr{L} = &\sum_j i\bar{q}_j\gamma_\mu(D^\mu - ig_sG^\mu)q_j - \frac{1}{4}G^\alpha_{\mu\nu}G^{\alpha\mu\nu} \\ &+ \sum_k i\bar{\psi}_k\gamma_\mu D^\mu\psi_k - \frac{1}{4}W^{a\mu\nu}W^a_{\mu\nu} - \frac{1}{4}B^{\mu\nu}B_{\mu\nu} \\ &- (D_\mu\phi)^\dagger(D^\mu\phi) - \lambda[\phi^\dagger\phi - \frac{\mu^2}{2\lambda}]^2 \\ &- \sum_j c_j\bar{q}_j\phi q_j - \sum_k f_k\bar{\psi}_k\phi\psi_k,\end{aligned} \tag{2.3}$$

where the Dirac spinors ψ_k denote the lepton fields and the Dirac spinors q_j the quark fields. The summation indices j and k stand for the three particle generations. The field strength tensors $G^\alpha_{\mu\nu}$ represent the gluon fields, the tensors $W^a_{\mu\nu}$ and $B_{\mu\nu}$ represent the electroweak gauge fields. The electroweak interactions between the gauge fields and the fermion fields are condensed in the covariant derivatives

$$D_\mu = \partial_\mu - ig\frac{\vec{\sigma}}{2}\vec{W}_\mu - ig'\frac{Y_W}{2}B_\mu \tag{2.4}$$

with the coupling constants g_s for the strong interaction and g' and g for the electroweak interactions. The scalar field ϕ in the Lagrange density in eq. (2.3) stands for a complex scalar doublet known as the Higgs field. It is worth highlighting that in the Standard Model Lagrange density eq. (2.3) no explicit mass terms appear because the Lagrange density is required to be gauge invariant under the gauge group $SU(3)_C \times SU(2)_L \times U(1)_Y$.

2.2. The BEH-Mechanism

The absence of mass terms in the Lagrange density implies that all particles in the Standard Model are massless which is, however, not supported by the experimental data. Introducing static mass terms in the Lagrange density, would break the gauge symmetry explicitly. To solve this issue, a group of theorists (R. Brout, F. Englert and P. Higgs)[3] introduced the idea to create the masses of the elementary particles dynamically [19], [20]. The main motivation of the BEH mechanism is the generation of

[3] Nobel Prize 2013 in physics for F. Englert and P. Higgs: *"for the theoretical discovery of a mechanism that contributes to our understanding of the origin of mass of subatomic particles, and which recently was confirmed through the discovery of the predicted fundamental particle, by the ATLAS and CMS experiments at CERN's Large Hadron Collider" [18]*

gauge boson masses, later on the mechanism was utilized to give rise to fermion masses via the introduction of the Yukawa interactions.

One crucial idea of the dynamic symmetry breaking is the introduction of a single complex scalar doublet

$$\phi = \begin{pmatrix} \phi^+ \\ \phi^0 \end{pmatrix}. \tag{2.5}$$

The ground state of this field can be written in the simplest form as

$$\phi = \frac{1}{\sqrt{2}} \begin{pmatrix} 0 \\ v + H(x) \end{pmatrix}. \tag{2.6}$$

where $H(x)$ is a real field and v is a real constant which minimizes the potential $V(\phi^\dagger\phi) = \lambda[\phi^\dagger\phi - \frac{\mu^2}{2\lambda}]^2$ of the scalar field hence $v^2 = \mu^2/\lambda^2$. The real field $H(x)$ is also known as the *Higgs boson*. Inserting (2.6) in

$$\begin{aligned} &- (D_\mu\phi)^\dagger(D^\mu\phi) - \lambda[\phi^\dagger\phi - \frac{\mu^2}{2\lambda}]^2 \\ &- \sum_j c_j \bar{q_j}\phi q_j - \sum_k f_k \bar{\psi}_k \phi \psi_k, \end{aligned} \tag{2.7}$$

while using the definiton of D_μ eq. (2.4) and evaluating Y_W accordingly, gives

$$\begin{aligned} \mathscr{L}_{\text{Higgs}} = &-\frac{1}{2}\partial_\mu H \partial^\mu H - \lambda v^2 H^2 - \lambda v H^3 - \frac{\lambda}{4} H^2 \\ &- \frac{1}{8} g'^2 (v + H)^2 |W_\mu^1 - i W_\mu^2|^2 \\ &- \frac{1}{8}(v + H)^2(-g'^2 v^2 W_\mu^3 + g B_\mu)^2 \\ &- \frac{1}{\sqrt{2}}(\sum_j c_j \bar{q_j}(v + H) q_j) \\ &- \frac{1}{\sqrt{2}}(\sum_k f_k \bar{\psi_k}(v + H)\psi_k) \end{aligned} \tag{2.8}$$

from which the mass terms of the bosons can be identified directly. For the spin-1 bosons the relevant term is

$$-\frac{1}{8} g'^2 v^2 |W_\mu^1 - i W_\mu^2|^2 - \frac{1}{8} v^2 (-g' W_\mu^3 + g B_\mu)^2. \tag{2.9}$$

Keeping in mind that the $W^\pm$-boson is a super position of the gauge fields W_μ^1 and W_μ^2,

namely $W_\mu^\pm = \frac{1}{\sqrt{2}}(W_\mu^1 \mp iW_\mu^2)$, the mass of the W-boson can be identified to be

$$M_{W^+} = M_{W^-} = \frac{g'v}{2} \tag{2.10}$$

Like the W-boson also the Z-boson is a combination of the gauge fields of the $SU(2)_L \times U(1)_Y$ group. It can be written as $Z_\mu = \frac{-gB_\mu + g'W_\mu^3}{\sqrt{g^2+g'^2}} = W_\mu^3 \cos\theta_W - B_\mu \sin\theta_W$ with the usual definition of the weak-mixing-angle $\cos\theta_W = \frac{g'}{\sqrt{g^2+g'^2}}$ and $\sin\theta_W = \frac{g}{\sqrt{g^2+g'^2}}$. The mass of the Z-boson can then be read as

$$M_Z^2 = \frac{1}{4}(g^2 + g'^2)v^2. \tag{2.11}$$

Moreover, the photon is a combination of the $SU(2)_L \times U(1)_Y$ group namely $A_\mu = W_\mu^3 \sin\theta_W + B_\mu \cos\theta_W$. No such term is present in eq. (2.8) hence the photon is a massless particle which is in agreement with the experimental data (see Table 2.2). The same argumentation holds for the eight gluon fields. The only spin-0 boson in the SM is the Higgs boson. Comparing (2.8) with the standard form of a mass term $-\frac{1}{2}m_H^2 H^2$ gives

$$m_H^2 = 2\lambda v^2 = 2\mu^2. \tag{2.12}$$

The full derivation of the fermion masses is beyond the scope of this thesis hence only the results will be discussed. The last two terms in eq. (2.8) have to be decomposed in particles with weak isospin $+1/2$ (e.g. up-type quarks and neutrino-like leptons) and $-1/2$ (e.g. down-type quarks and electron-like leptons). For the fermions one can find that the mass terms are

$$\begin{aligned} m_i^{\text{up-type quarks}} &= \frac{1}{\sqrt{2}} g_i v \\ m_i^{\text{down-type quarks}} &= \frac{1}{\sqrt{2}} h_i v \\ m_i^{\text{neutrino-like}} &= 0 \\ m_i^{\text{electron-like}} &= \frac{1}{\sqrt{2}} f_i v \end{aligned} \tag{2.13}$$

where for each particle mass an individual Yukawa parameter g_i, f_i or h_i is needed. The index i runs over the three particle generations. It is worth emphasizing that for neutrinos the Yukawa coupling is conventionally set to zero.

2.3. Interactions in the SM

In the Standard Model Lagrangian or rather in equation (2.8) there are terms which describe the coupling of the Higgs boson with the spin-1 $W^{\pm}$ and Z bosons:

$$\begin{aligned}\mathscr{L} &= -\frac{1}{8}g'^2(2vH+H^2)|W^1_\mu - iW^2_\mu| - \frac{1}{8}(2vH+H^2)(-g'W^3_\mu + gB_\mu)^2 \\ &= -(\frac{H}{v}+\frac{H^2}{2v})(2M^2_{W^\pm}W^+_\mu W^{-\mu} + M^2_Z Z_\mu Z^\mu),\end{aligned} \tag{2.14}$$

with the term $\frac{2M^2_{W^\pm}}{v}HW^+_\mu W^{-\mu}$ being the most interesting one in this thesis. It describes the coupling or the decay of a Standard Model Higgs boson into two W-bosons. As long as $m_H < 2M_{W^\pm}$ one of the two W-bosons is an off-shell (virtual) particle, whereas for masses $m_H > 2M_{W^\pm}$ the two W-bosons are on-shell and the extra energy from the Higgs boson mass is propagated to the two W-bosons in the form of kinetic energy. The W-boson can decay into a lepton-neutrino pair with a probability of roughly $32.40 \pm 0.18\%$ or a quark-anti-quark pair which happens in roughly $67.60 \pm 0.27\%$ of the cases [17]. In this thesis only events are analyzed where the Higgs boson decays into two W-bosons which then both decay into a lepton-neutrino pair. In Figure 2.1 the Feynman diagram for such $H \to WW^{(*)} \to \ell\nu\ell\nu$ decays is shown.

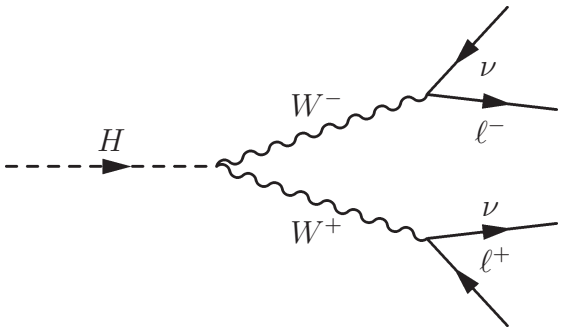

Figure 2.1.: Higgs boson decaying into two W-bosons which both decay leptonically.

The possible decays of the Standard Model Higgs boson depend on its mass m_H. Figure 2.2 shows the branching ratio for the Standard Model Higgs boson for the mass-range $80\,\text{GeV} \leq m_H \leq 1\,\text{TeV}$. Owing to the fact that the mass of the Standard Model Higgs boson is measured to be $125.36 \pm 0.41\,\text{GeV}$, the actual branching ratio of this particle is known. One part of this thesis is the search for additional Higgs-like bosons (see section 2.4) which are assumed to have a similar branching ratio distribution as for the Standard Model Higgs. The decay into two W-bosons is the dominant mode for masses above $m_H \gtrsim 140\,\text{GeV}$ and is therefore well suited to analyze the decays of very heavy Higgs(-like)-bosons.

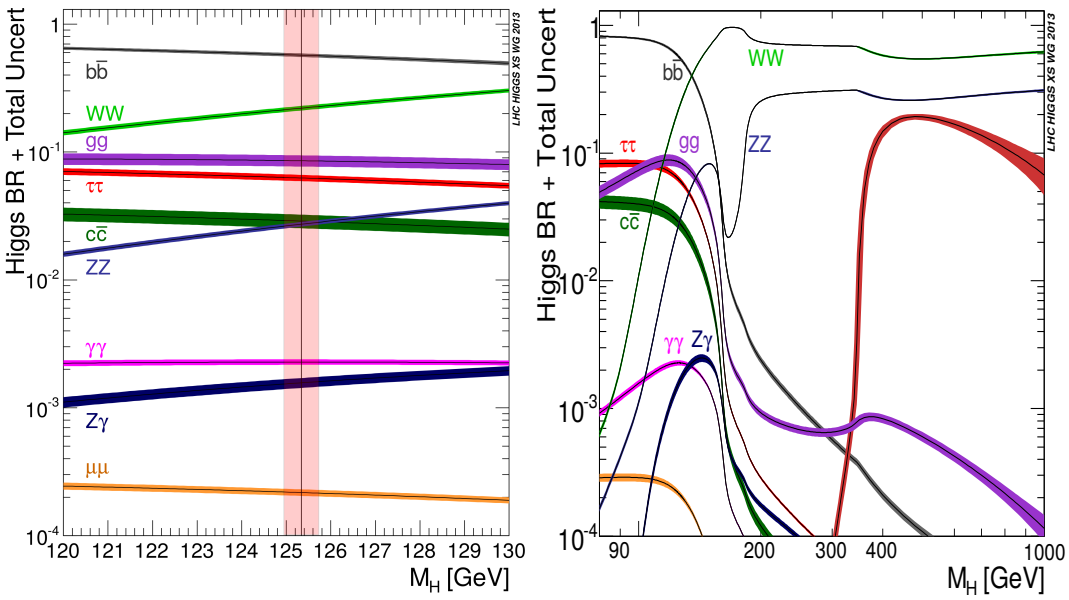

Figure 2.2.: Branching ratio of the Standard Model Higgs boson depending on its mass m_H [21].

The Higgs boson couples only to massive particles like fermions (not neutrinos) and $W^{\pm}$ and Z bosons. In a proton-proton collider like the LHC it can therefore be produced via the fusion of two gluons in a quark loop (ggF), the fusion of two massive vector bosons which are radiated from quarks (VBF), in association with a massive vector boson[4] (WH or ZH) or via the annihilation of two top-quarks originating from the decay of two gluons (ttH). In Figure 2.3 the Feynman diagrams of those four production mechanisms are shown.

[4] Also known as Higgs-Strahlung.

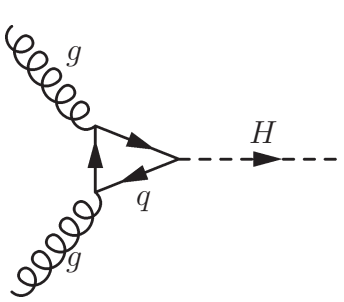

(a) The gluon-fusion production mode: ggF

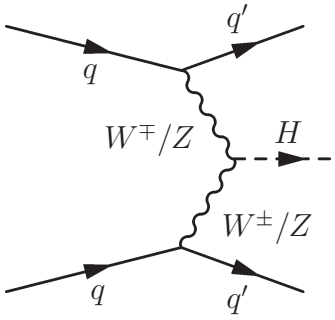

(b) The vector boson fusion process: VBF.

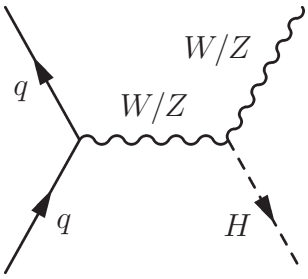

(c) The production of a Higgs boson in association with a W or Z-boson: WH or ZH.

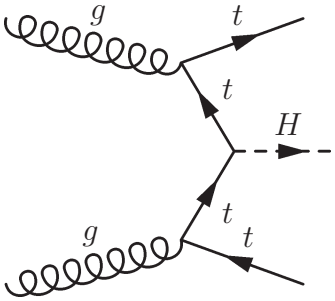

(d) The production of a Higgs boson from the annihilation of two top quarks originating from the decay of two gluons: ttH.

Figure 2.3.: Feynman diagrams of the production mechanisms of the Standard Model Higgs boson at a hadron-hadron collider such as the LHC.

The production mechanism changes the particle content in the final state. In this thesis only the ggF and VBF production play an important role. Those two modes are the dominant production mechanisms in the analyzed mass-range of m_H. Figure 2.4 shows the cross section of the production mechanism depending on the mass of the Higgs boson for a center of mass energy $\sqrt{s} = 8\,\text{TeV}$.

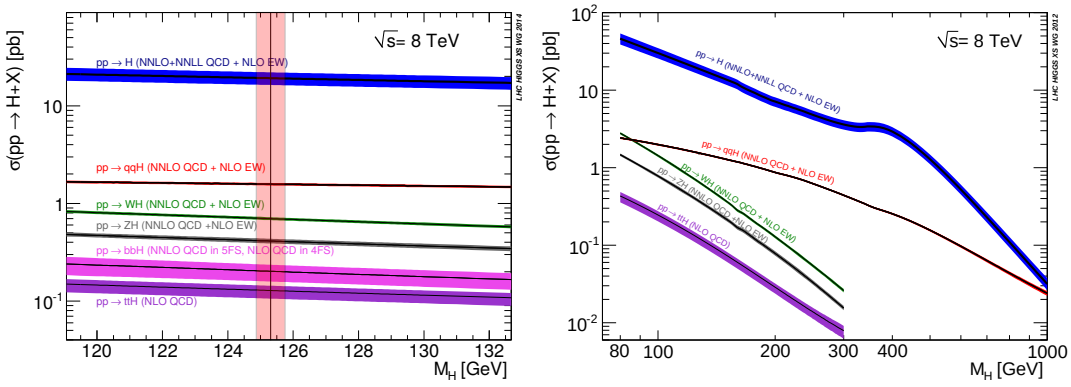

Figure 2.4.: Production cross section of the Standard Model Higgs boson depending on its mass m_H at a center of mass energy $\sqrt{s} = 8\,\text{TeV}$. The colored bands around the theory curves show the uncertainty arising from the theoretical calculations on the cross-section. The uncertainty of the ggF production mode (blue area) is one of the leading uncertainties in the measurement of the couplings of a Standard Model Higgs bosons with a mass $m_H = 125.36 \pm 0.41\,\text{GeV}$ (see chapter 8) [21].

Background processes

Besides the coupling of the Higgs boson to the other particles in the Standard Model, also couplings between the gauge bosons and fermions play an important role for the analysis of $H \to WW^{(*)} \to \ell\nu\ell\nu$ events. Each process producing two leptons and two neutrinos in the final state is interesting in the analysis of $H \to WW^{(*)} \to \ell\nu\ell\nu$ events. One set of processes which can produce such a final state is the production of two W-bosons which can originate from a quark-anti-quark initial state or from a gluon-gluon initial state. The Feynman diagrams of those processes are shown in Figure 2.5.

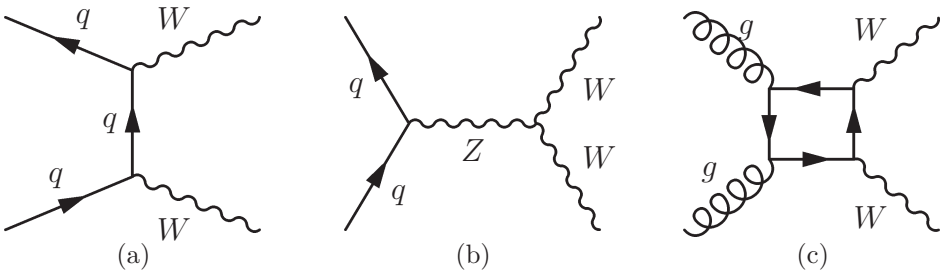

Figure 2.5.: WW production at the LHC via the modes $qq \to WW$ and $gg \to WW$. The presented diagrams only show the dominant contributions.

Other processes where two leptons and neutrinos are produced can also enter the analysis. In Figure 2.6 the Feynman diagram of a top-anti-top pair decay as well as a single

top decay in association with a W-boson is presented as further examples of background processes in the analysis of $H \to WW^{(*)} \to \ell\nu\ell\nu$ decays. Further backgrounds relevant for the analysis of $H \to WW^{(*)} \to \ell\nu\ell\nu$ events will be discussed in chapter 7.

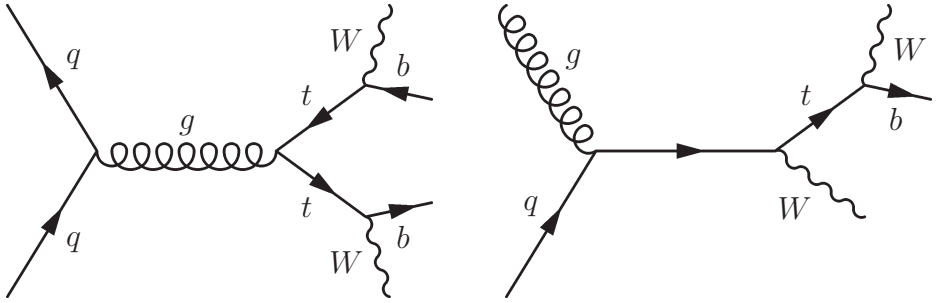

(a) top-anti-top pair production and decay (b) single top production and decay

Figure 2.6.: Feynman diagrams for the production and decay of a top-anti-top pair and for a single top.

In a proton-proton collider the probability of a certain inital state to be present (in the example of Figure 2.5 qq or gg) depends on the center of mass energy. The proton is a composite object which means each parton of the proton carries a fraction of the proton momentum specified by the Bjorken scale variable $x = \frac{p_{\text{parton}}}{p_{\text{proton}}}$. The partons of the proton can be a valence quark (two u-quarks, one d-quark), a sea-quark or a gluon. The sea quarks of the proton are the result of QCD pair production inside the proton. The momentum fractions of the partons change with increasing energy which is illustrated in Figure 2.7. With augmenting energy the fractions of gluons and sea-quarks increase while the fractions of the valence quarks decrease.

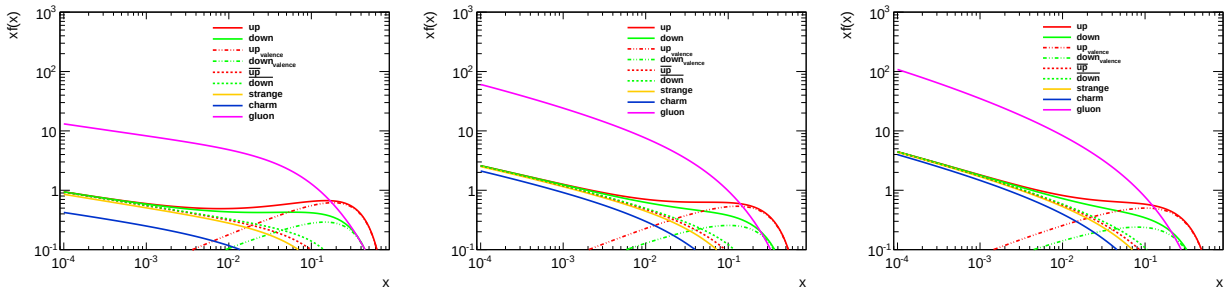

(a) $Q^2 = 10\,\text{GeV}^2$ (b) $Q^2 = 1000\,\text{GeV}^2$ (c) $Q^2 = 100000\,\text{GeV}^2$

Figure 2.7.: Parton distribution functions for the proton as a function of the Bjorken variable x. The PDFs are shown for three different scales $Q^2 = 10\,\text{GeV}^2$, $Q^2 = 1000\,\text{GeV}^2$ and $Q^2 = 100000\,\text{GeV}^2$. No uncertainties on the parton fractions are plotted in the distributions. The data in the plots is taken from the CTEQ10 PDF set as published on the hepdata homepage [22].

Hadronization

As mentioned earlier quarks do not appear as single particles in nature. They are only present in color neutral bound states called hadrons. The formation process of those colorless objects from color charged particles is called hadronization. If two quarks are formed as the result of a hard scattering process as indicated in Figure 2.8, the energy density between those two quarks increases as they drift apart. The cause of this is that the strong potential is proportional to the distance between two color charged particles (quarks). The quarks are accompanied by gluon and photon emission. Those emission processes are implemented as perturbative corrections in the theoretical treatment which can be approximated by the parton shower approach. The showering of two (or more) quarks originating from a hard or soft scattering process is stopped, once a fixed energy scale is reached. The gluons and the photons in these showering processes can convert into quark-anti-quark pairs from which the bound color neutral states can then be formed.

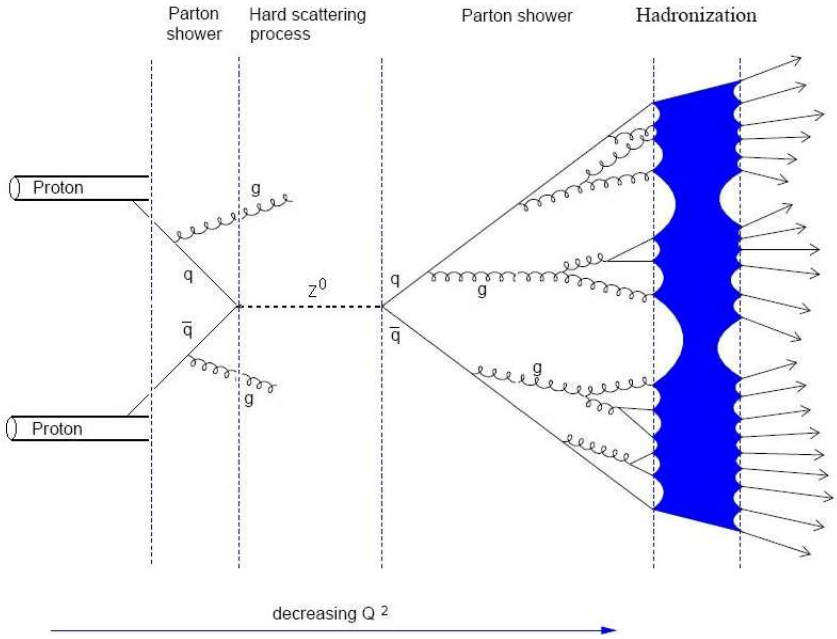

Figure 2.8.: Two quarks from protons scatter hard and produce a Z boson which decays again into a quark-anti-quark pair. The two quarks as the result of the hard scattering process decay into color-neutral hadrons. The process of the two quarks decaying into color neutral hadrons is called hadronization.

2.4. Possible extensions of the SM with further Higgs-like bosons

The discovery of the Higgs boson by the ATLAS [1] and CMS [2] collaboration completes the particle spectrum of the Standard Model of particle physics. Up to this day, measurements of the properties of the Higgs boson like resonance at around 125 GeV are in full agreement with the theoretical predictions. But those measurements do not establish the particle as the only Higgs boson. A possible extension of the Standard Model with an extended Higgs sector remains possible. The analysis presented in this thesis is used to test three different scenarios.

Standard Model Higgs boson
In the first scenario, no assumption about the resonance at $\approx 125\,\text{GeV}$ are made hence the search for a Standard Model Higgs boson is performed over the full accessible mass range up to 1 TeV. The search for a Standard Model Higgs boson is in this thesis abbreviated as the Standard Model like (or shortened SM-like) scenario. The decay width of the Standard Model Higgs boson increases with the mass which is shown in Figure 2.9.

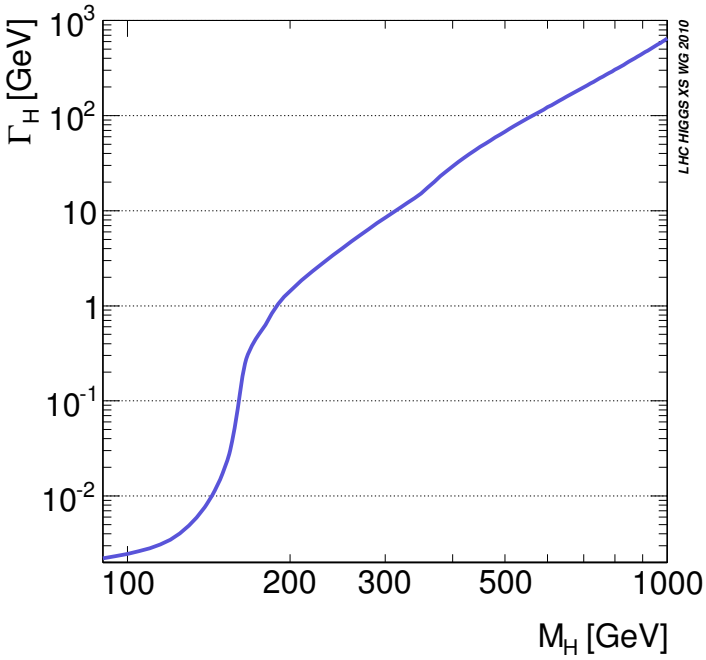

Figure 2.9.: Width of the Higgs boson Γ_H as a function of its mass [21].

Due to the very large width of the Higgs boson at high masses the interference between the non-resonant $gg \to WW$ background (see Figure 2.5c) and the Higgs signal is a non negligible effect for masses $m_H \geq 400\,\text{GeV}$.

Narrow width approximation
A different approach in the search for further Higgs-like bosons is the narrow width approximation (NWA). For the NWA scenario the width of the hypothetical heavy Higgs boson is fixed to 1 GeV and its line shape is treated as a Breit-Wigner over the full mass range. Within the scope of this thesis the search for a NWA scenario is a model independent search. Such a heavy Higgs boson, however, can find implementation in super symmetry (SUSY) models like the minimal supersymmetric Standard Model (MSSM) [23]. For the NWA signal the interference with the non-resonant WW background is negligible. A NWA Higgs signal is searched in the mass range $200\,\text{GeV} \leq m_H \leq 2\,\text{TeV}$.

Electroweak singlet
The simplest model incorporating the SM Higgs boson sector as well as an additional Higgs-like particle is called the "125 GeV Higgs + a real electroweak singlet" (EWS) model [24]. The additional electroweak singlet mixes to the SM Higgs doublet field in order to complete the unitarization of WW scattering at high energies [25],[26],[27]. The singlet field also acquires a non-vanishing vacuum expectation value, which means an additional neutral resonance is added to the particle content of the SM. The process of dynamically breaking the $SU(2)_L \times U(1)_Y$ group gives rise to two CP-even Higgs bosons, the resonance at 125 GeV, denoted as H and a heavier resonance denoted as h. It is assumed that the couplings of the SM Higgs H and those of the additional EWS Higgs h scale with respect to the couplings of the SM Higgs by common scaling factors κ and κ' for H and h, respectively. From unitarity follows that

$$\kappa^2 + \kappa'^2 = 1. \tag{2.15}$$

The limit $\kappa' \to 0$ corresponds to the SM-only case. In the further analysis it is assumed that the decay modes of H and h are identical. The production cross section and the decay rates of H are modified according to:

$$\begin{aligned} \sigma_H &= \kappa^2 \times \sigma_{H,\text{SM}} \\ \Gamma_H &= \kappa^2 \times \Gamma_{H,\text{SM}} \\ \text{BR}_{H,i} &= \text{BR}_{H,\text{SM},i}. \end{aligned} \tag{2.16}$$

The index i stands for the different decay modes. The heavier Higgs h can have additional decay modes like $h \to HH$. The production cross section and the decay rates are modified with respect to those of a SM Higgs with a mass m_H equal to the mass of the EWS Higgs m_h.

$$\begin{aligned} \sigma_h &= \kappa'^2 \times \sigma_{H,\text{SM}} \\ \Gamma_h &= \frac{\kappa'^2}{1 - \text{BR}_{h,\text{new}}} \times \Gamma_{H,\text{SM}} \\ \text{BR}_{h,\text{new},i} &= (1 - \text{BR}_{h,\text{new}}) \times \text{BR}_{H,\text{SM},i} \end{aligned} \tag{2.17}$$

where $\mathrm{BR}_{h,\mathrm{new}}$ denotes all additional decay modes. It is assumed that the event kinematics of the EWS Higgs are similar to those of the SM Higgs. The EWS model is used as a benchmark to search for physics beyond the Standard Model where the width of h (see eq. (2.17)) can be larger or smaller than the width of the SM Higgs. A scan of the plane m_h vs. Γ_h is performed where the mass range between 200 GeV and 1 TeV is explored and the width Γ_h is varied from $0.2 \times \Gamma_H$ to $1.0 \times \Gamma_H$ with a step size of 0.2[5].

[5]The NWA scenario can be seen as the lower extreme case in the sense of low width in the EWS model.

3. The ATLAS experiment & The LHC

The LHC is a hadron collider located at CERN and it is the largest particle accelerator worldwide. It is designed to reach a center of mass energy of $\sqrt{s} = 14\,\text{TeV}$ while the datasets used in this thesis were recorded with $\sqrt{s} = 7\,\text{TeV}$ and $\sqrt{s} = 8\,\text{TeV}$. The following chapter summarizes the functionality of the large hadron collider LHC and the ATLAS detector. The ATLAS experiment is one of four experiments located at the interaction points of the two beams in the LHC. The four experiments are: CMS, ATLAS, ALICE and LHCb. CMS and ATLAS are multipurpose detectors whereas ALICE and LHCb are designed to analyze specific physics processes. The goals of the CMS and ATLAS experiment is to perform high-precision measurements of the Standard Model and to search for signatures of new physics at the TeV scale. The ALICE experiment studies the properties of the quark-gluon plasma [28] and LCHb is a dedicated b-physics precision experiment. In order to exploring the properties of the quark-gluon plasma with ALICE, heavy ions such as lead get injected in the LHC. In LHCb very rare decays of charm and beauty-flavored hadrons as well as CP-violating observables are analyzed [29].

3.1. The Large Hadron Collider

The LHC at CERN it the biggest particle storage ring with a circumference of 27 km. It is on average 100 m below the ground, located in an area near the Swiss city Geneva. The protons entering LHC get accelerated via a complex system of pre-accelerators located at CERN, see Figure 3.2. They start at a linear accelerator LINAC with an energy of 50 MeV and getting then subsequently accelerated via a group of circular accelerators to 1.4 GeV, 25 GeV and finally 450 GeV [30]. In the LHC the protons get accelerated to the center of mass energy $\sqrt{s}$ required by the experiments which was $\sqrt{s} = 7\,\text{TeV}$ in 2011, $\sqrt{s} = 8\,\text{TeV}$ in 2012 and is planned to be $\sqrt{s} = 13\,\text{TeV}$ in 2015 and finally $\sqrt{s} = 14\,\text{TeV}$ (the design energy of the LHC) in 2016 or 2017.

The protons in the LHC are injected as bunch of particles containing about $\approx 1.5 \cdot 10^{11}$ protons. Those bunches are squeezed down to about 64 μm in diameter and about 8 cm in

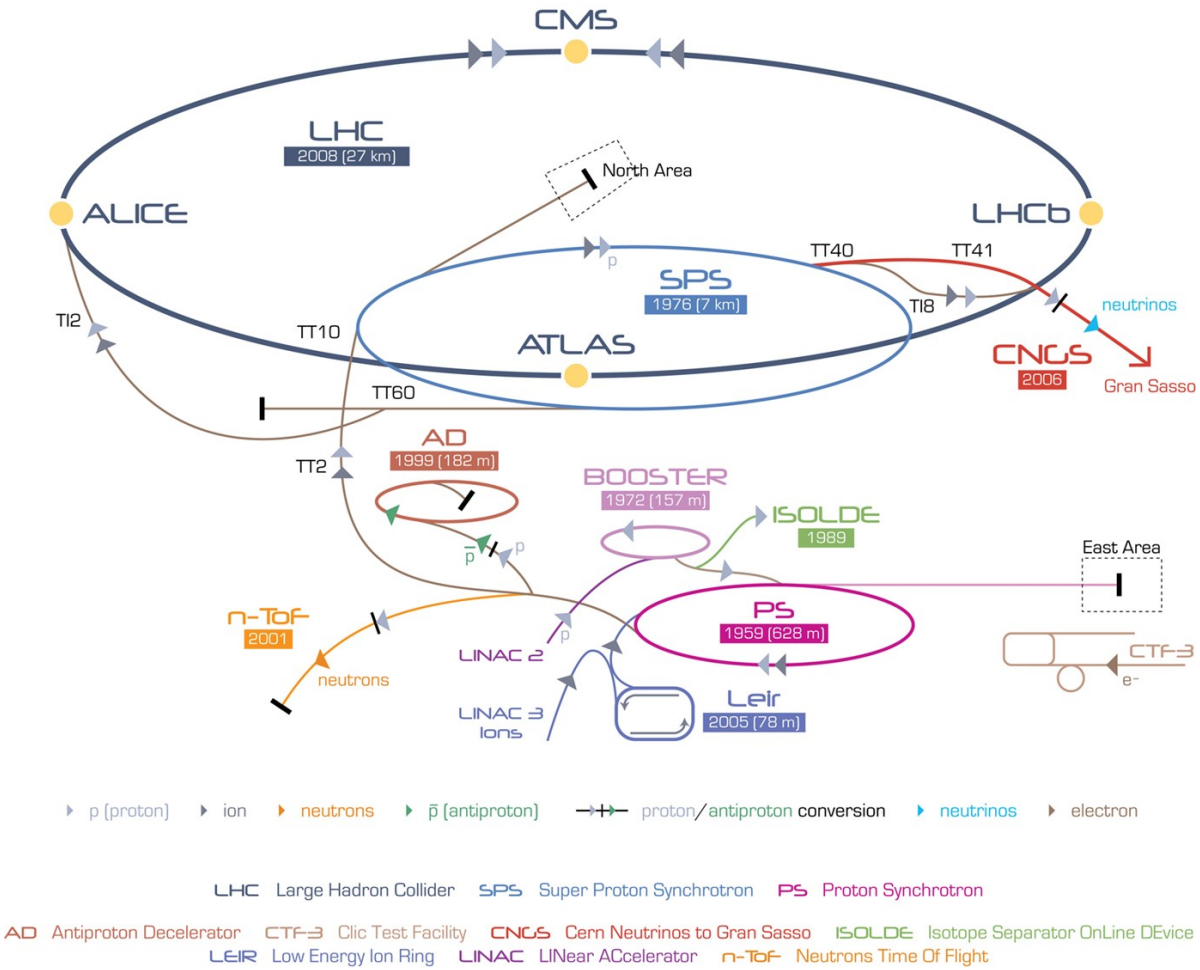

Figure 3.1.: The CERN accelerator complex [31].

length at the interaction points in the experiments. In 2012 the bunch spacing was set to 50 ns leading to a brunch-crossing rate of 20 MHz. In order to guide the proton bunches their way around the LHC, superconducting dipole magnets are installed around the LHC ring. The proton beams are focused using superconducting quadrapole magnets. The magnetic field strength in each of those magnets is up to 8.5 T which is achieved via strong electrical currents. Those strong currents are transported via superconducting cables which are cooled down to a temperature of roughly 1.9 K (or −271.3 °C) [32].

3.2. The ATLAS detector

The ATLAS[1] experiment at the LHC (see Figure 3.2) is designed to search for new physics beyond the SM as well as to perform high-precision measurements of the Stan-

[1] **A** Toroidial **LHC** Apparatu**S**

dard Modell. The detector is constructed in four radial-symmetric layers around the beam axis or rather around the interaction point within ATLAS. It can be divided into four segments:

1. Inner detector and tracker

2. Electromagnetic calorimeters

3. Hadronic calorimeters

4. Muon spectrometer.

The full detector is about 25 m in height and about 44 m in length.

ATLAS coordinate system
The origin of the ATLAS coordinate system is located at the interaction point in the center of the detector. The $xy-$plane is perpendicular to the proton beam, the x-axis points to the center of the LHC ring and the y-axis points into the opposite direction of the gravitational field of the earth hence upwards. The z-axis points in the direction of the proton beam where the positive z direction is determined via the requirement to have a right handed coordinate system. Due to the cylindric form of ATLAS, cylindric coordinates are used where the azimuthal angle ϕ is measured in the xy-plane[2] and the spherical angle θ is measured relatively to the z-axis. The angle θ is used to define the pseudorapidity:

$$\eta = -\ln(\tan\frac{\theta}{2}) \tag{3.1}$$

which allows to divide the sub-detectors of ATLAS in so called end-cap segments and barrel segments where each sub-detector has a different coverage in $|\eta|$.

[2] $\phi = 0$ corresponds to the positive x-axis.

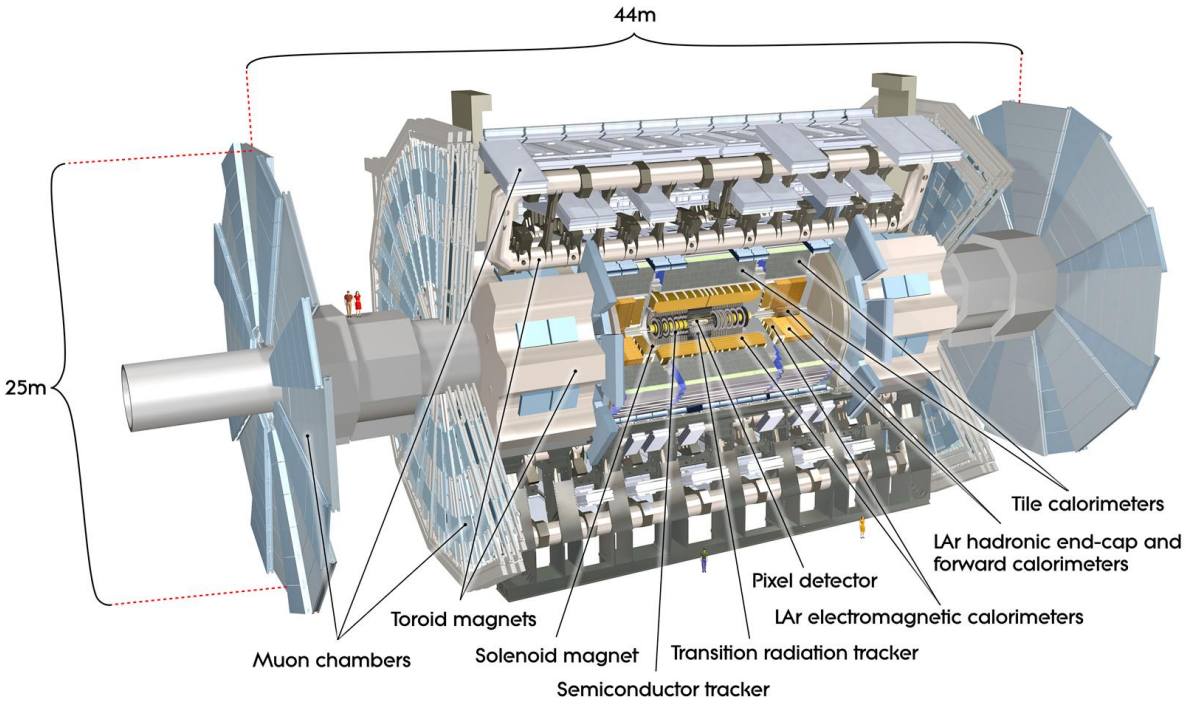

Figure 3.2.: The ATLAS detector at the LHC.

During the data taking two magnetic fields are present in the ATLAS detector. The inner detector is built-in within a solenoid coil which produces a magnetic field of roughly 2 T and the muon spectrometer of ATLAS is within a toroidal magnetic field produced by 8 superconducting coils. The toroidal field strength is about 0.5 T [33], [34].

3.2.1. Inner Detector

The inner detector (ID) of ATLAS (see Figure 3.3) has a cylindrical form with a length of 7 m and a diameter of 2.3 m. It is the detector which is closest to the interaction point hence it receives the most hard radiation. As mentioned earlier the ID is located within a 2 T solenoidal magnetic field. Due to the magnetic field the trajectories of charged particles get bent proportional to the particle momentum. One of the main tasks of the ID is to measure the tracks of charged particles and consequently the particle momentum. The transverse momentum resolution in the inner detector for charged particles is $\frac{\Delta p_{\mathrm{T}}}{p_{\mathrm{T}}} = 0.0004 \cdot p_{\mathrm{T}} \oplus 0.02$ (p_{T} in GeV) [33], [34].

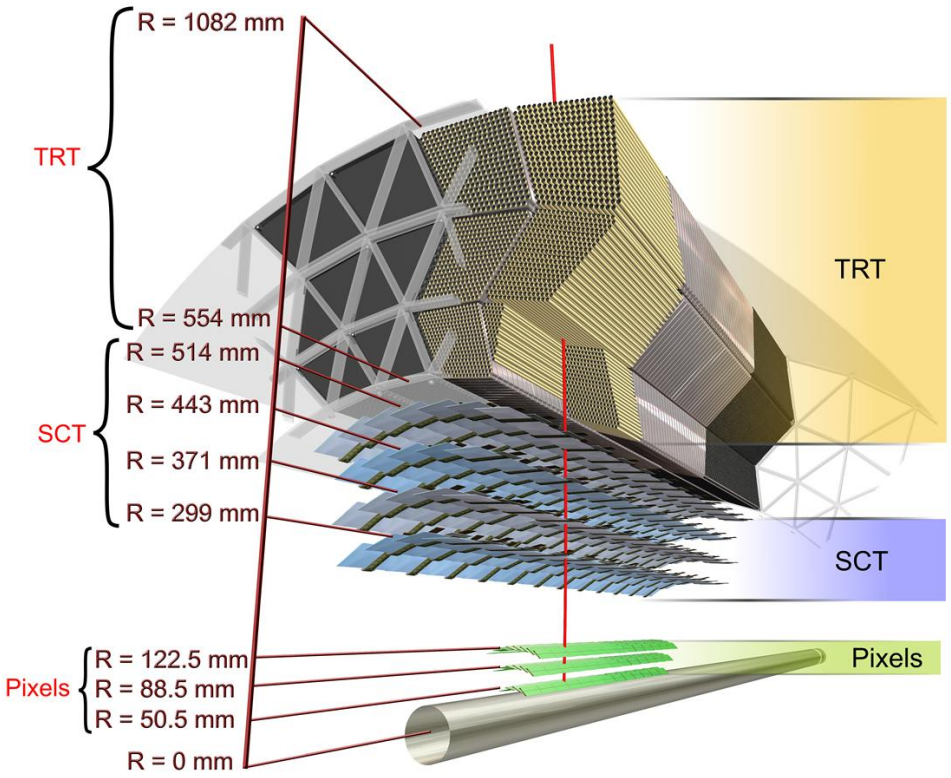

Figure 3.3.: The inner detector of the ATLAS experiment.

The inner detector is constructed of three segments:

Pixel detector

The pixel detector consists of 2100 silicon sensor modules arranged in three layers. Each module is 62.4 mm long and 21.4 mm wide. The coverage of each module is 24×160 pixels with a pixel size of $50 \times 400\,\mu$m. The main task of the pixel detector is the reconstruction of secondary vertices and related to this the b-tagging of jets [33], [34].

Semi conductor Tracker (SCT)

The SCT is built of eight layers of PIN silicon micro-strip detectors where the tracks of particles are reconstructed with high-precision. The resolution is $17\,\mu$m in the $R - \phi$ plane and $580\,\mu$m in the z-direction [33], [34].

Transition radiation tracker (TRT)

The TRT is built of radiators and straw tubes. The straw-tubes are drift tubes with a diameter of 4 mm, made from wound Kapton and reinforced with thin carbon fibres. In the center of each straw-tube a gold-plated tungsten wire with a diameter of 31 μm is located and the straw-tubes are filled with a gas mixture of 70 % Xe, 20 % CO_2 and 10 % CF_4. The particles drifting through the TRT pass through materials with alternating optical density which cause a charged particle to emit photons once it passes through the boundary between two layers with different optical density. Those photons ionize the gas in the straw-tubes where the amount of free charges of the ionization process is measured which helps to determine the type of particle passing through the TRT. Furthermore, the tracks of charged particles get measured [33], [34].

3.2.2. Electromagnetic Calorimeter

Calorimeters are used to measure the energy of single particles. The electromagnetic (EM) calorimeter is divided into a barrel and an end-cap segment. It consists of Kapton electrodes and absorber plates made of iron and lead. In order to maximize the fiducial volume of the calorimeter, the segments are arranged in a so called accordion structure in which liquid Argon is injected between the electrodes and the absorbers. If a high-energetic particle passes through the calorimeter it interacts with the absorber plates, creating a shower of low-energetic particles such as electrons, positrons or photons. The shower of low-energetic particles ionizes the liquid Argon and the produced free charges are measured at the Kapton electrodes. The amount of measured charge is proportional to the energy of the high-energetic particles entering the calorimeter. The energy resolution of the electromagnetic calorimeter is $\Delta E/E = 0.115/\sqrt{E} \oplus 0.005$ (E in GeV), the coverage of the EM barrel calorimeter is $|\eta| < 1.52$ and the EM calorimeter in the end-caps have a coverage of $1.375 < |\eta| < 3.2$ [33], [34].

3.2.3. Hadronic Calorimeter

The hadronic calorimeter is used to measure the energy of hadrons such as π-mesons, neutrons or protons. The energy resolution of the hadronic calorimeters is $\Delta E/E = 0.50/\sqrt{E} \oplus 0.3$. It is divided into three areas:

- The **tile calorimeter** is built of scintillator and absorber plates made of steel. It covers the region $|\eta| < 1.7$. Like in the electromagnetic calorimeter, particles passing through the calorimeter interact with the absorber plates and produce a shower

of low-energetic particles. Those particles produce photons in the scintillator plates which are transported via wavelength-shifting fibers to photon multipliers where the total photon energy is measured [33], [34].

- The **liquid Argon calorimeters in the forward and end-cap region** of ATLAS have a functionality very similar to the electromagnetic calorimeter. The end-cap calorimeter covers the region $1.5 < |\eta| < 3.2$ and the forward calorimeter has a coverage of $3.1 < |\eta| < 4.9$ [33], [34].

In Figure 3.4 a detailed illustration of the ATLAS calorimeter system is presented.

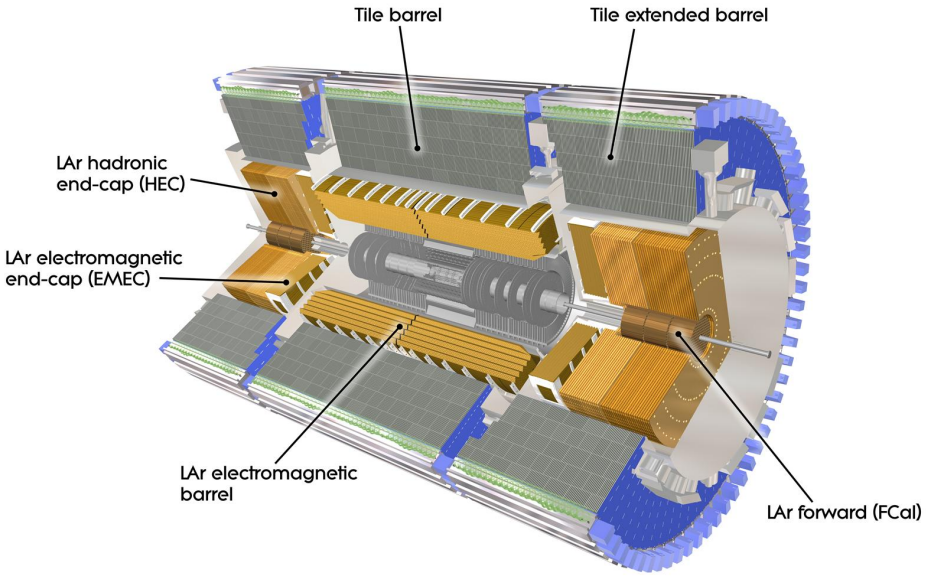

Figure 3.4.: The calorimeters of the ATLAS detector.

3.2.4. Muon Spectrometer

The largest component of the ATLAS detector is the muon spectrometer with an inner radius of about 5 m and an outer radius of about 11 m. At the energy scale present in the ATLAS detectors, muons are minimal ionizing particles, hence they pass through the whole ATLAS detector. The muon spectrometer is therefore the outermost part of ATLAS. As mentioned earlier the muon spectrometer is within the toroidal magnetic field of the ATLAS detector which causes the muon trajectories to bend. Like in the ID the tracks of the particles get measured in the muon spectrometer and consequently the curvature of the particle which is proportional to the particle momentum. The spectrometer is assembled from four different types of muon chambers: monitored drift tubes

(MDT), resistive plate chambers (RPC), thin gab chambers (TGC) and cathode strip chambers (CSC). The structure of the muon spectrometer is shown in Figure 3.6 [33], [34].

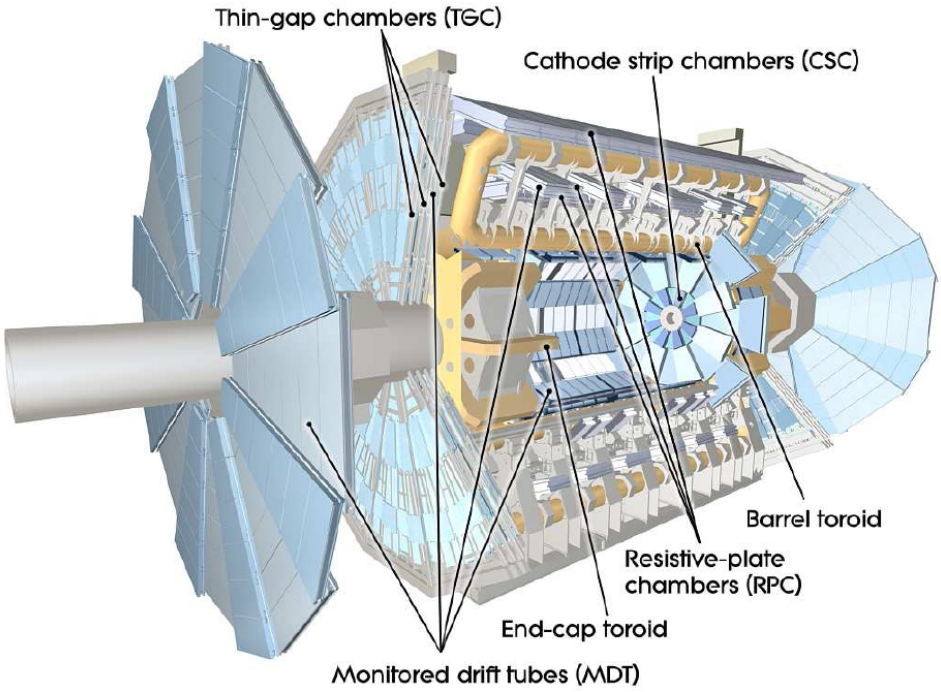

Figure 3.5.: Structure of the ATLAS muon spectrometer.

The RPCs and TGCs main task is triggering as well as measuring the muon coordinates orthogonal to the MDTs and CSCs while the MDTs and CSCs are used to measure the tracks of the muons with high precision [34]. The momentum resolution of the muon spectrometer as a function of the muon transverse momentum is presented in Figure 3.6.

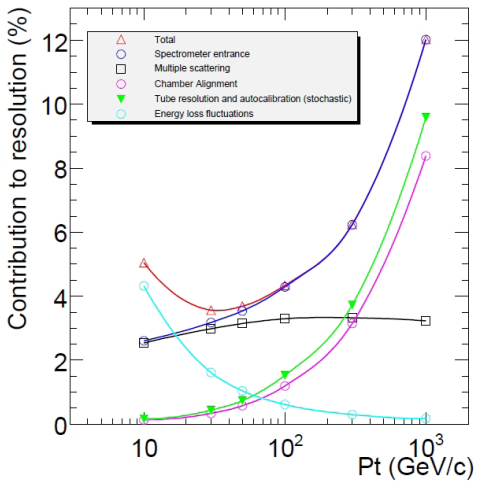

Figure 3.6.: Momentum resolution for muons with $|\eta| < 1.5$. The different constituents of the resolution are shown.

3.3. Object reconstruction

The information obtained from the measurements of the individual segments of the ATLAS detector get combined to reconstruct physical objects which are photons, electrons, muons, taus, jets and missing transverse energy. In the following the object reconstruction procedure of the objects which are of interest for the $H \to WW^{(*)} \to \ell\nu\ell\nu$ analysis will be introduced briefly.

3.3.1. Electron reconstruction

Electrons get reconstructed via three different reconstruction algorithms depending on the electron energy and pseudorapidity η. For the reconstruction of high energetic electrons, in a first step, clusters of calorimeter cells in the EM calorimeter are formed. The threshold for an EM cluster to be considered is 3 GeV and the cluster building efficiency is 95 % for electrons with $E_{\mathrm{T}} = 7\,\mathrm{GeV}$, 99 % for $E_{\mathrm{T}} = 15\,\mathrm{GeV}$ and 99.9 % for an electron $E_{\mathrm{T}} = 45\,\mathrm{GeV}$ [35]. A cluster corresponds to a region in the $\eta \times \phi$ plane hence it is a collection of calorimeter cells. Once the EM cluster is defined, the reconstruction software tests if at least one track of the inner detector points toward a EM cluster in a given $\eta \times \phi$ region. If the latter is not the case and no track can be fitted to an EM cluster, it is very likely that the energy deposit in the EM calorimeter is from an uncharged particle, for example a photon. In the case of low energetic electrons the reconstruction algorithm works the other way around. Tracks from the inner detector get extrapolated into the EM calorimeter and consequently a cluster of energy deposits in the EM calorimeter is

formed around the extrapolated track. It is then checked whether the integrated energy is above a certain threshold. The reconstruction of high- and low-energetic electrons is limited to $|\eta| < 2.5$ due to the dimension of the inner detector. For electrons in the forward region ($2.5 < |\eta| < 4.9$) of the ATLAS detector only the information of the EM calorimeter is used. Depending on the geometry (e.g. shower width) of the clustered energy deposit, the track quality (e.g. number of hits in the ID), the energy deposit in the hadronic calorimeter and the quality of the track extrapolation, the reconstructed electrons are categorized into different sets of quality criteria. Those quality criteria are then used in the later analysis of the ATLAS data (see section 5.1) [36].

3.3.2. Muon reconstruction

The reconstruction of muon tracks is achieved using the four different types of muon chambers in the spectrometer and the tracking information of the inner detector, while precision measurements of muon tracks in the largest part of the η-region are performed executed by the MDTs. The principle of the muon track reconstruction in the MDTs will be discussed briefly. The MDT chambers consist of two multilayer of drift tubes which are filled with a gas mixture of argon and carbon dioxide. In the center of a drift tube sits a tungsten-rhenium wire which is on high voltage and forms the anode while the grounded cylindric tube forms the cathode. A muon passing through the drift tubes ionizes the gas and the resulting free electrons get accelerated towards the wire in the center of the drift tube. Due to the high-voltage in the drift tube, the electrons ionize further gas atoms and create an avalanche of free electron ion pairs. The amount of free charges measured is proportional to the distance between the wire in the center of the drift tube and track of the muon passing through the drift tube. In each drift tube the distance of the muon track from the central wire is reconstructed as a radius. Since the MDTs are constructed of at least two multilayers of drift tubes, the muon track can be reconstructed using the measured drift radii in each drift tube. Like for the electron reconstruction also the muon reconstruction makes use of three different algorithms which are: *Standalone muons*, *combined muons* and *tagged muons* [37]. In the following they will be discussed shortly.

Standalone muons:

As the name “standalone” already indicates, for this type of muon reconstruction only one part of the detector is used. The information used is obtained from the muon spectrometer exclusively where the muon track is extrapolated to the interaction point in order to determine impact parameters. The energy loss of the muon in the calorimeters is incorporated in the extrapolation [37].

Combined muons:

For combined muons, both the information from the ID and from the muons spectrometer are used. A track measured in the muon spectrometer is fitted to a suitable track measured in the ID [37].

Tagged muons:

Tagged muons are similar to combined muons, with the main difference being in the fit direction. For tagged muons the track from the ID is extrapolated to the muon spectrometer. If a track measured in the muon spectrometer is in accordance with the extrapolated ID track, a muon is identified [37].

3.3.3. Jet reconstruction

Color charged particles hadronize (see section 2.3) into color neutral mesons or baryons. The hadronization of color charged particles leads to the fact that a color charged particle originating from a hard scattering process is reconstructed as a so called jet. A jet is the collection of color neutral compound states originating from the hadronization of the color charged particle. In the later described $H \rightarrow WW^{(*)} \rightarrow \ell\nu\ell\nu$ analysis, the anti-k_t algorithm is used to reconstruct those particle jets. The algorithm evaluates the resolution variable $d_{k\mathrm{B}}$, which is the distance in momentum-space between an object k and the beam jet B, i.e. proton remanent and the variable d_{kl} as the distance in momentum-space between an object k and and object l:

$$d_{k\mathrm{B}} = p_{\mathrm{T}k}^{-2}, \qquad d_{kl} = min(p_{\mathrm{T}k}^{-2}, p_{\mathrm{T}l}^{-2}) \times \frac{\Delta R_{kl}^2}{R^2} \\ \text{with } \Delta R_{kl}^2 = (\eta_k - \eta_l)^2 + (\phi_k - \phi_l)^2. \tag{3.2}$$

In this work, the distance parameter R is set to 0.4. The objects k and l are energy deposits above a certain noise threshold in combined topological clusters of the calorimeters of the ATLAS detector. The algorithm determines the minimum of all $d_{k\mathrm{B}}$ and d_{kl}. If the minimal value is the distance between two objects d_{kl}, the two objects k and l are merged together. If otherwise $d_{k\mathrm{B}}$ is minimal, the object k is considered as a jet and is removed from the list of objects considered in the iterative determination of the minimum $min(d_{k\mathrm{B}}, d_{kl})$. One advantage of the anti-k_t algorithm is its infrared as well as its collinear safeness [38], [39] ,[40].

3.3.4. Missing transverse energy

In a hypothetically perfect particle detector all energies and momenta of all objects, present in a given event, can be measured. Since ATLAS is a real detector, not all

objects can be reconstructed. For example, it is not practicable to measure the energy and momenta of neutrinos and particles which are not covered by the Standard Model may also interact in a way which is not noticeable by the sub-detectors of ATLAS. Owing to this fact a quantity called missing transverse energy $\not{E}_{\mathrm{T}}^{\mathrm{miss}}$ is defined reflecting all not-measurable particles and objects. The $\not{E}_{\mathrm{T}}^{\mathrm{miss}}$ is calculated from the measurements of all transverse momenta and energies deposits of all objects (electrons, muons, photons, jets, etc.) present in a given event. The vectorial sum of all measured transverse momenta and $\not{E}_{\mathrm{T}}^{\mathrm{miss}}$ should be equal to zero which reflects energy and momentum conservation in the transverse plane [17]:

$$\not{E}_{\mathrm{T}}^{\mathrm{miss}} = | - \sum \vec{p}_{\mathrm{T}}^{\,\text{reconstructed objects}} |. \tag{3.3}$$

In the reconstruction of the missing transverse energy, all visible particles are included hence all detector parts of ATLAS are relevant. For energy deposits and particle tracks which are not assigned to any reconstructed physics objects, a soft term is added to the $\not{E}_{\mathrm{T}}^{\mathrm{miss}}$ definition. In order to not include detector noise in the $\not{E}_{\mathrm{T}}^{\mathrm{miss}}$ calculation a certain minimal energy threshold is required. The vectorial sum of the transverse momenta of all reconstructed objects can be either determined from the calorimeter information, the track information or the combination of both detector parts. In the analysis of $H \to WW^{(*)} \to \ell\nu\ell\nu$ decays the only expected electrically neutral particles from the signal process are the neutrinos. The two leptons are electrically charged particles and leave a track in the ID of ATLAS hence for the $\not{E}_{\mathrm{T}}^{\mathrm{miss}}$ reconstruction only the track information of the physical objects can be used.

3.4. Trigger and Data Acquisition

During the data taking in 2012 the bunch crossing rate was roughly 20 million per second and on average about 20 interaction per bunch crossing happened. Each bunch crossing corresponds to an event detectable by ATLAS with a data volume of about 1.5 MB. It is not possible to store this enormous data stream efficiently onto hard disks, tape or any other commercial data storage device. Due to this large data stream, ATLAS uses a three-layered trigger system to filter physically interesting events. The functionality of the trigger system will be briefly introduced in the following.

- **Level 1 trigger (L1)**

  The first trigger level is a hardware based trigger system which makes use of the deposits in the calorimeters and the measurements of the RPCs (barrel) and TGCs (end-caps). The RPCs and TGCs fire if the measured momentum is greater than a certain threshold. The deposits in the calorimeters are combined with a granularity of $\Delta\eta \times \Delta\phi = 0.1 \times 0.1$ in so called calorimeter towers. If the integrated energy

in such a calorimeter tower or in the RPCs and TGCS is greater than a certain threshold, a region of interest (RoI) is defined which is consequently passed to the next trigger level. The level 1 trigger reduces the event rate to a maximum of 75 kHz [33], [34].

- **Level 2 trigger (L2)**

  The L2 trigger is a software based trigger. The selection algorithms are implemented in a server cluster with roughly 500 quad-core CPUs. The information of the detector parts within a window around the RoI, defined in the L1, are analyzed to reach a decision if an event contains interesting physical objects or not while the information of the ID is incorporated in the L2. The level 2 trigger reduces the event rate to a maximum of 1 kHz [33], [34].

- **Event filter trigger (EF)**

  The final trigger stage is the software based event filter trigger. The EF algorithms are installed in a server cluster with roughly 1800 Quad-Core CPUs. In the EF the first particle trajectories and objects get reconstructed to reach a decision if an event is of interest for a further, detailed analysis. An event passing through the event filter selection, gets stored onto tape. The maximum event output rate of the EF is roughly 600 Hz [33], [34].

With the output rate of roughly 600 Hz the amount of data produced by ATLAS in one year is on the order of a petabyte (=10^{15} byte). To handle such large data volumes a powerful computing environment is necessary: The worldwide LHC computing grid (WLCG) [41]. The raw data of ATLAS is processed in a computing center called "tier-0" located at CERN at which all physical objects present in an event get reconstructed and the data is reprocessed into different file types. The reprocessed data (as well as the Monte Carlo simulations, see chapter 4) is distributed to eleven large computing centers around the globe called "tier-1"s where the data is further reprocessed. From the "tier-1"s the datasets are further distributed to more than 160 "tier-2"s and "tier-3"s.

3.4.1. Measurement of Trigger efficiencies

The author has been involved in the measurement of the efficiency of event filter single electron triggers with an electron E_T threshold of 12 GeV[42]. In the following, the data driven *Tag&Probe* method will be introduced and the obtained results of the trigger efficiency measurement will be presented.

The *Tag&Probe* method:
For the measurement of a single electron trigger efficiency $Z \rightarrow ee$ events can be used

which have the advantage that all particles in the final state can be reconstructed. One of the reconstructed electrons is selected by a single trigger signature and is used as a reference (the *tag*) while the other electron in the final state is used to compute the efficiency (the *probe*) of the trigger signature in question. The well known Z boson resonance is used since it provides a good source of isolated *probe* particles with a high purity. To select such $Z \to ee$ events, only events which have fired a reference single electron trigger are considered. The reference trigger can be any single electron trigger. Moreover, only events which have two reconstructed electrons with an invariant mass (see section 6.2) of $70\,\text{GeV} < m_{ee} < 100\,\text{GeV}$ are analyzed and it is furthermore required that at least one of the two reconstructed electrons can be matched to the single electron reference trigger. The matching of the offline objects to the online objects is achieved via the requirement that $\Delta R = \sqrt{\Delta\eta^2 + \Delta\phi^2}$ of the two objects should be smaller than 0.15. The other electron may or may not pass the trigger selection and is defined as the *probe*. The efficiency of a single electron trigger is computed by the fraction of probes which can be matched to an online electron fulfilling the trigger selection of the trigger in question [42].

Results:
The efficiency of a single electron trigger with a E_T threshold of 12 GeV was measured in the 2011 dataset as a function of p_T and η. The reference trigger for the *tag* electrons was the highest unprescaled trigger in the 2011 data taking which had a E_T threshold of 20 GeV in the first data-taking periods and 22 GeV in the later data taking. To reduce the contribution of background events in the analyzed m_{ee} window, events with both electrons carrying the same charge were subtracted from the dataset. The systematic uncertainty of the measured efficiency was obtained via changing the invariant mass cut to $65\,\text{GeV} < m_{ee} < 110\,\text{GeV}$ and to $75\,\text{GeV} < m_{ee} < 100\,\text{GeV}$, alternating the matching requirement from $\Delta R < 0.15$ to $\Delta R < 0.1$ or $\Delta R < 0.2$ and varying the reconstruction quality criteria of the *tag* electron. The impact on the trigger efficiency from pile-up events was estimated by separating the data sample into a high pile-up (> 10 primary vertices) and low pile-up (≤ 10 primary vertices) sample and computing the efficiency in the two samples separately. The uncertainty arising from pile-up was found to be negligible. In Figure 3.7 the trigger efficiency for the single electron trigger with a E_T threshold of 12 GeV is presented, the suffix *medium* refers to the reconstruction quality criteria (see section 3.3.1 and section 5.1) and the abbreviation *T* and *Tvh* refers to selection criteria on the online object in order to remove electron candidates with a certain amount of energy deposit in the hadronic calorimeters (=hadronic leakage). The efficiency was found to be greater than 95 % for an electron $p_\text{T} \geq 20\,\text{GeV}$ and the total systematic uncertainty was found to be smaller than 1 % over the full analyzed p_T and η range (see also section 8.1) [42]. More details can be found in Ref. [42].

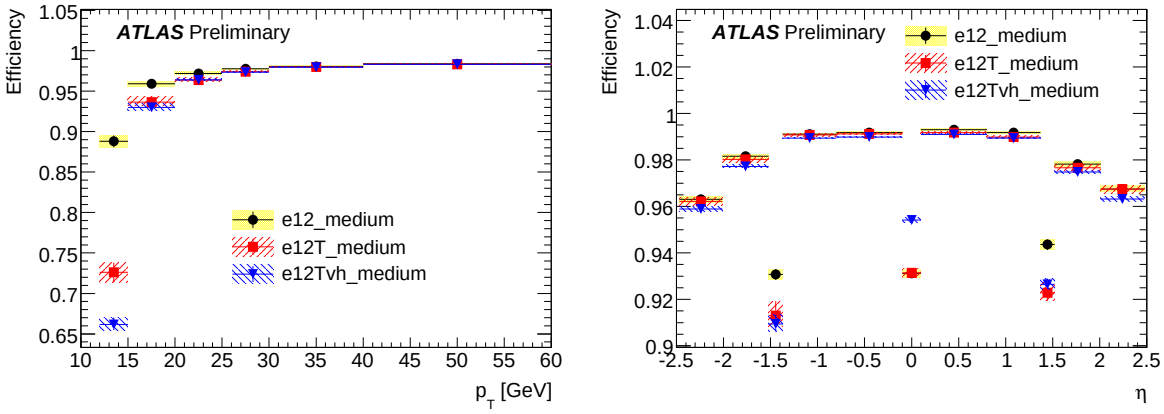

Figure 3.7.: Trigger efficiency for a single electron trigger with a E_{T} threshold of 12 GeV as a function of p_{T} and η [42]. The efficiency of the electron triggers as a function of η reflects the construction of ATLAS. The drops of the efficiency at $\eta \approx 0$ and $|\eta| \approx 1.5$ are caused by the transition regions between the end-cap and barrel segments of the electromagnetic calorimeter.

3.5. Pile-up

In each bunch crossing at LHC multiple protons can interact via elastic or inelastic scattering processes. The hard scattering processes may produce high energetic particles which are selected by the ATLAS trigger chain. The whole event or rather the full detector information present in such an event is then stored onto tape. The term "pile-up" (or in this case in-time event pile-up) refers to all the additional hard or soft scattering processes in a bunch crossing which may or may not have produced a high energetic particle selected by the ATLAS trigger. Moreover, the measurement information of energy deposits originating from previous bunch crossings can still be present in the ATLAS detector readout buffer. Those deposits can be wrongly associated with an event triggered by a subsequent bunch crossing. Such energy deposits are referred to as out-of-time or detector pile-up. To investigate the impact of the pile-up conditions two observables are defined:

- Number of primary vertices: N_{Vtx}.

  The information of primary vertices is determined from the tracking information and reflects the in-time event pile-up conditions.

- Average number of interactions per bunch crossing[3]: μ.

  The number of interactions per bunch crossing is an observable proportional to the total inelastic proton-proton cross section. It is obtained using luminosity measurements and reflects both the in-time as well as the out-of-time pile-up conditions.

It has been observed that the N_{Vtx} is roughly a factor two smaller than the average number of interactions per bunching. The Monte Carlo samples used in this thesis (see chapter 4) were simulated with fixed pile-up condition. To model the pile-up conditions during data taking correctly, the simulated μ distribution was rescaled to $0.9 \cdot \mu$. More details on the μ rescaling as well details on the treatment of pile-up effects on physics objects such as $\not{E}_{\mathrm{T}}^{\mathrm{miss}}$ can be found in Ref. [43].

[3]The signal strength in the likelihood fit (see chapter 9) is also denoted as μ.

Part II.

Analysis

4. Data Sets

The Monte Carlo samples used for background and signal are introduced in this chapter as well as the data analyzed. The data was recorded in 2011 and 2012. The main focus of this thesis lies on the 2012 data but in some of the final results measurements based on the 2011 datasets are incorporated. For various background and signal samples different Monte Carlo (MC) generators are used, some generators are specialized for processes like GG2WW3.1.2 which is used for the simulation of $gg \to WW$ decays [44]. But there are also multi-purpose generators like PYTHIA or HERWIG. The generator HERWIG simulates hard lepton-lepton, lepton-hadron and hadron-hadron scattering at leading order (LO) [45]. Also PYTHIA simulates multi particle collisions at LO and is used as an interface for other generators (like POWHEG+PYTHIA for the signal samples and WW background or ACERMC+PYTHIA for t-channel single top decays) to simulate initial and final state radiation, hadronization and further decays [46], [47]. The two versions of PYTHIA (PYTHIA6 and PYTHIA8) used in this analysis differ mainly by the programming language used in the implementation. Version 6 of PYTHIA is implemented in `Fortran` and the newer version 8 is written in `C++`. ALPGEN calculates matrix elements also at LO for various multiparton interactions [48]. The ACERMC generator is specialized for processes with top or bottom quarks in the final state [49]. SHERPA is another multipurpose generator and is able to simulated high energy reactions of particles for lepton-lepton, lepton-photon, photon-photon and hadron-hadron collisions [50]. The POWHEG generator (or rather the POWHEG method) is a tool to calculate matrix elements at next-to-leading-order for various processes [51]. The specialized GG2ZZ generator is used to simulated the NLO loop-induced gluon fusion process $gg \to ZZ \to 4\ell$ [52]. The events generated by the various MC generators are passed through a GEANT4 [53] simulation of the ATLAS detector. The following section will highlight which MC generator was used for which process.

4.1. Monte Carlo signal samples

Regarding the low and high mass analysis (see section 6.4), the signal samples in the $H \to WW$ analysis are slightly different. Depending on the mass of the Higgs boson the description of the lineshape differs. For Higgs masses below 400 GeV it is valid to use a Breit-Wigner (BW) to describe the lineshape but it could be shown [54], [55], [56]

that for masses $m_{\mathrm{H}} \geq 400\,\mathrm{GeV}$ a BW is not valid anymore. For those samples a more correct approach to describe the Higgs lineshape has been adopted which is known as the Complex Pole Scheme (CPS). Another effect becomes more and more dominant with an increasing mass namely the interference between signal and the non-resonant WW background [56], [57], [58]. This effect changes both the production cross section as well as kinematic distributions. The inclusion of the interference effect is crucial for $m_H \geq 400\,\mathrm{GeV}$. Regardless of the mass of the Higgs signal, the generators used are Powheg+Pythia8 for signal originating from the gluon-fusion and from the vector boson fusion process. For Higgs bosons produced in association with a W or Z boson Pythia8 is used. The samples for the narrow width approximation scenario are simulated using the same generators.

4.1.1. Interference between signal and non-resonant WW background

As mentioned earlier, the interference between the signal and the non-resonant WW background is found to be not negligible for $m_H \geq 400\,\mathrm{GeV}$ due to the large decay width. In Ref. [59], the interference effect as well as a prescription of the computation of theoretical uncertainties is addressed. It is known at leading order (LO) in QCD but is not included in the Powheg+Pythia8 gluon- and vector boson fusion samples used. Consequently, both the ggF and VBF signal samples are weighted to account for the interference. For the ggF signal the interference weights were computed at LO using MCFM 6.3 [60] and were rescaled to the NNLO cross section. The interference weights for the VBF signal were extracted using REPOLO (REweighting POwheg events at Leading Order), a tool provided by the authors of VBFNLO [59], [61], [62]. In Figure 4.1 the transverse mass m_{T} (see section 6.2) is presented for a 400 GeV, a 700 GeV and a 1 TeV Higgs signal. The difference in the signal kinematics due to the applied interference weights is evident. Furthermore, the estimated uncertainty envelopes of the interference weights are shown. For the narrow-width-approximation (NWA) samples the width of the Higgs boson is fixed to 1 GeV for all mass-points hence no interference weights are applied. The NWA samples are also generated with Powheg+Pythia8 for ggF and VBF.

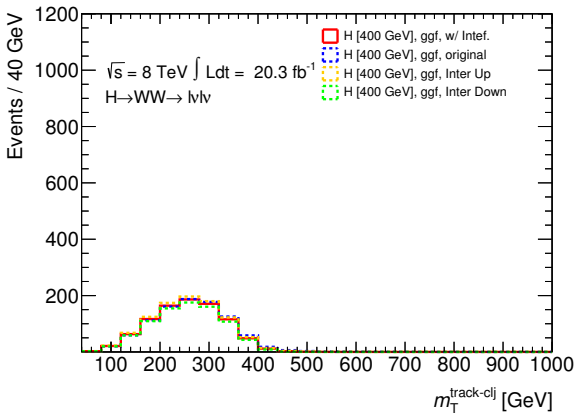

(a) m_{T} for a SM-like 400 GeV Higgs, production: ggF

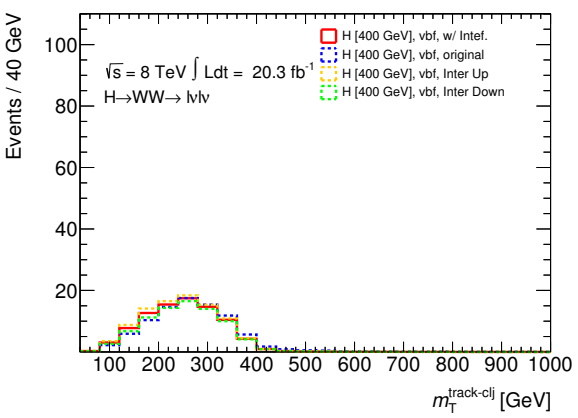

(b) m_{T} for a SM-like 400 GeV Higgs, production: VBF

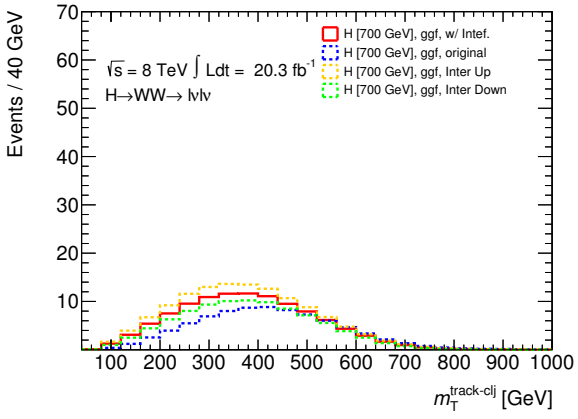

(c) m_{T} for a SM-like 700 GeV Higgs, production: ggF

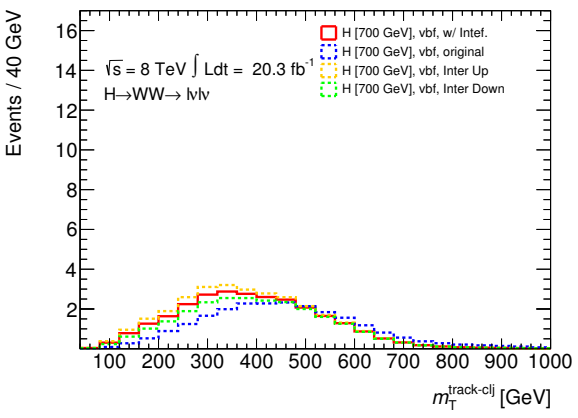

(d) m_{T} for a SM-like 700 GeV Higgs, production: VBF

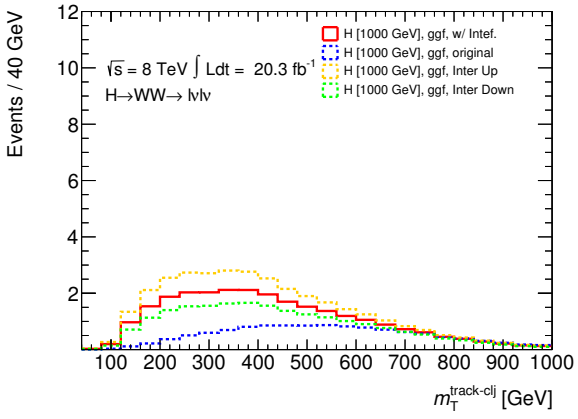

(e) m_{T} for a SM-like 1 TeV Higgs, production: ggF

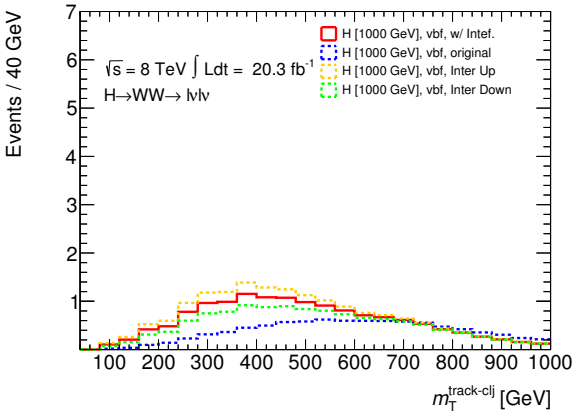

(f) m_{T} for a SM-like 1 TeV Higgs, production: VBF

Figure 4.1.: The distributions show the transverse mass m_{T} (see section 6.2) for a Standard Model like Higgs boson with a mass of 400 GeV, 700 GeV and 1 TeV. The plots on the left show the signal produced via the gluon-fusion process, the plots on the right are for VBF produced Higgs signal. The blue dashed line corresponds to the unweighted MC sample, the red solid line is the signal with the interference weight applied, the orange and green dashed line represent the interference weight uncertainty envelope.

4.1.2. Electroweak singlet signal

For the EWS (see section 2.4) scenario besides the interference effect also the scaling of the width Γ has to be taken into account. The scaling of the couplings κ' varies the width Γ_{SM} of the signal as well as the production cross section $\sigma = \kappa' \cdot \sigma_{H,\mathrm{SM}}$. Since the width of the signal has an effect on the interference between signal and non-resonant WW background, the interference weights used also depend on κ'^2 for $m_H \geq 400$ GeV. Technically speaking for the EWS signal the SM(-like) signal is weighted twice: Once to vary the width between $0.1 \times \Gamma_{\mathrm{SM}}$ and $1.0 \times \Gamma_{\mathrm{SM}}$ and a second weight for the interference effect individually for each value of κ'. The event weights which affect the decay width of the signal were obtained using the POWHEG generator with a running width BW propagator [63]. Figure 4.2 shows the m_{T} distributions for ggF and VBF produced Higgs signal for $m_H = 200$ GeV, 600 GeV and 1 TeV. The width of the signal is re-weighted to $0.1 \times \Gamma_{\mathrm{SM}}$, $0.5 \times \Gamma_{\mathrm{SM}}$ and $0.9 \times \Gamma_{\mathrm{SM}}$. For 600 GeV and 1 TeV the corresponding interference weights are applied.

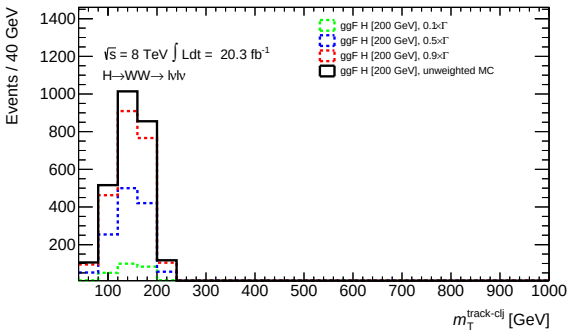

(a) m_{T} for a 200 GeV Higgs, production: ggF

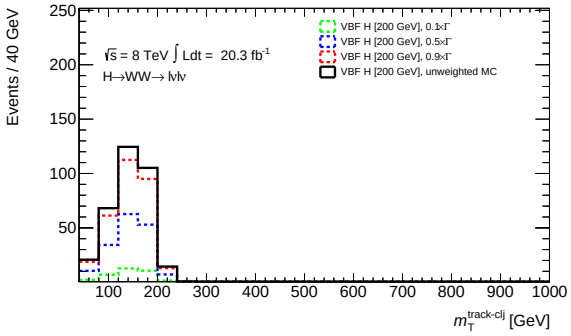

(b) m_{T} for a 200 GeV Higgs, production: VBF

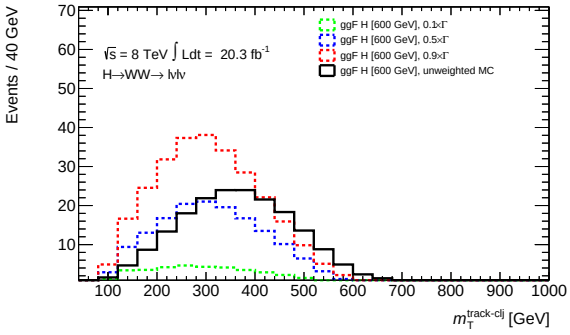

(c) m_{T} for a 600 GeV Higgs, production: ggF

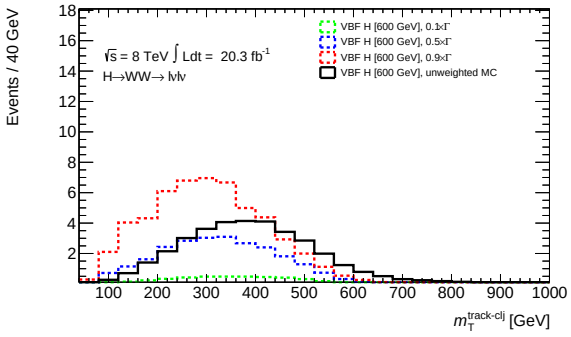

(d) m_{T} for a 600 GeV Higgs, production: VBF

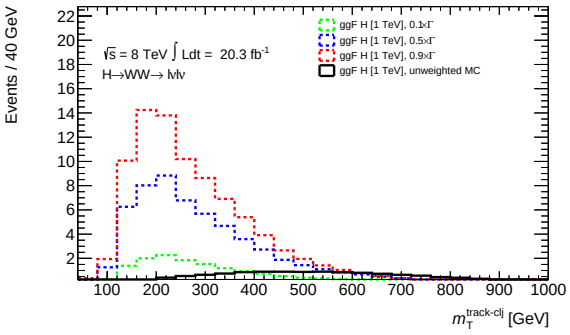

(e) m_{T} for a 1 TeV Higgs, production: ggF

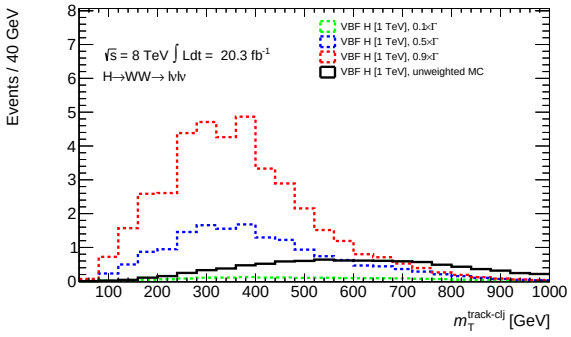

(f) m_{T} for a 1 TeV Higgs, production: VBF

Figure 4.2.: The plots show the transverse mass distribution for the mass hypothesis 200 GeV, 600 GeV and 1 TeV. The width of the signal samples is weighted to $0.1 \times \Gamma_{\mathrm{SM}}, 0.5 \times \Gamma_{\mathrm{SM}}$ and $0.9 \times \Gamma_{\mathrm{SM}}$. For the masses $m_{\mathrm{H}} \geq 400\,\mathrm{GeV}$ the corresponding interference weights are applied. The latter also depend on the weighting of the signal width $\kappa' \times \Gamma_{\mathrm{SM}}$. Moreover, the unweighted (no interference weighs and no width weights applied) MC sample is shown.

4.2. Monte Carlo background samples

WW background
The $qq \to WW \to \ell\nu\ell\nu$ processes are simulated using POWHEG+PYTHIA6. For $gg \to WW \to \ell\nu\ell\nu$ GG2WW3.1.2 is used. One sample of the WW background is simulated using SHERPA which covers the processes $WW \to \ell\nu\ell\nu + 2$ jets.

top background
For the $t\bar{t}$ background the POWHEG+PYTHIA interfaces are used. The single top s-channel diagrams as well as the $Wt \to \ell\ell$ decays are simulated using POWHEG+PYTHIA6. The t-channel single top background contribution is simulated using the ACERMC+PYTHIA6 interface.

Z+jets background
The $Z \to ee/\mu\mu/\tau\tau +$ NpX samples are simulated using the ALPGEN+HERWIG Monte Carlo generator. The abbreviation NpX indicates the number of additional associated partons in the Monte Carlo sample where the number of additional partons 'X' runs from 0 to ≥ 5. In the high mass analysis (see section 6.4) additional ALPGEN+HERWIG $Z \to \ell\ell$+NpX samples are introduced. Those samples have more than 5 million events for $m_{\mathrm{Z}}^{\mathrm{truth}} > 100\,\mathrm{GeV}$ (high $m_{\ell\ell}$ region) and should help to minimize statistical uncertainties arising from Z+jets background in the phase space of the high mass analysis. The $Z \to ee/\mu\mu/\tau\tau + \gamma$ processes incorporated in the analysis are simulated via SHERPA. A set of samples where a Z boson is produced via the vector boson fusion process is included. Those $Z \to ee/\mu\mu/\tau\tau + 2$ jets samples are also generator using SHERPA.

Non-WW background
The Non-WW background covers decays of WZ,ZZ,$W\gamma$ or $W\gamma^*$. The ZZ processes are generated using POWHEG+PYTHIA8 for $qq \to ZZ \to 2\ell 2\nu/4\ell$, SHERPA for $ZZ \to 2\ell 2\nu + 2$ jets and $ZZ \to 4\ell + 2$ jets and GG2ZZ for $gg \to ZZ \to 4e/4\mu/2e2\mu$. The WZ decays are simulated via POWHEG+PYTHIA8 and SHERPA for $WZ \to 3\ell\nu + 2$ jets. Decays originating from $W\gamma^\star$ processes have been generated using SHERPA and $W\gamma$ with ALPGEN+HERWIG.

4.3. Data taken with the ATLAS detector

There are two data samples used in the $H \to WW^{(*)} \to \ell\nu\ell\nu$ analysis. In 2011 the center of mass energy of the LHC was $\sqrt{\mathrm{s}} = 7\,\mathrm{TeV}$ while for the 2012 dataset it was increased to $\sqrt{\mathrm{s}} = 8\,\mathrm{TeV}$. For the 2011 run the average number of interactions per bunch crossing $< \mu >$ is shown in the left part of Figure 4.3. After a technical stop in September 2011

β^*[1] was changed from 1.5 m to 1.0 m. The recorded analyzed integrated luminosity of the 2011 dataset is $\int \mathcal{L}dt = 4.5\,\text{fb}^{-1}$ [64]. For the 2011 data set two bunch spacings were used: 25 ns and 50 ns. The runs at which the bunch spacing was 25 ns only delivered very few good physics runs. Therefore, the runs at 25 ns are not used, hence the difference of integrated luminosity between Figure 4.3 and the $4.5\,\text{fb}^{-1}$ used. For the $\sqrt{s} = 8\,\text{TeV}$ the bunch spacing was fixed to 50 ns for the full data taking period. The right part of Figure 4.3 shows the mean interactions per bunch crossing for 2012. The analyzed recorded integrated luminosity for the $\sqrt{s} = 8\,\text{TeV}$ dataset is $\int \mathcal{L}dt = 20.3\,\text{fb}^{-1}$. Only data which fulfills a certain set of data quality requirement is used in the analysis. Those data quality requirements reflect the functionality of the various subdetectors of the ATLAS experiment (see chapter 3). The amount of luminosity is obtained from a so called "good run list" (GRL) using the standard ATLAS luminosity tool [65].

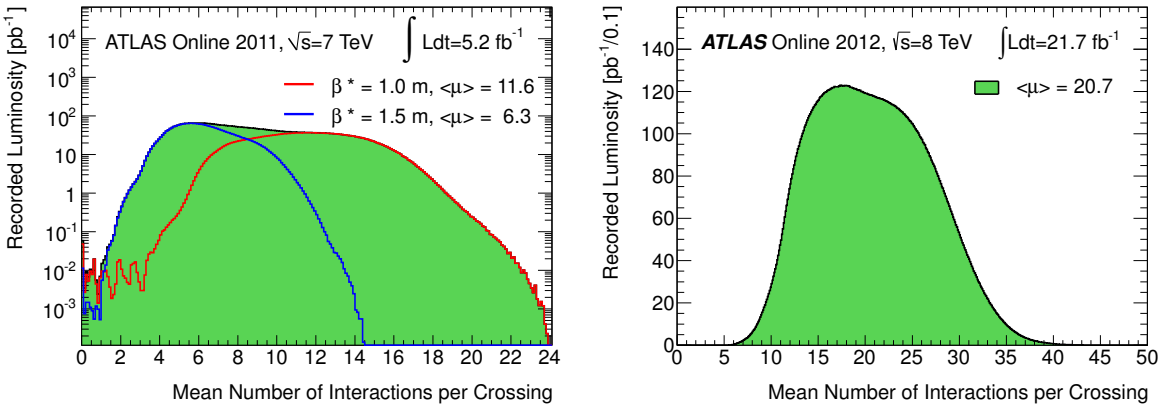

(a) $< \mu >$ for the 2011 $\sqrt{s} = 7\,\text{TeV}$ data recording (b) $< \mu >$ for the 2012 $\sqrt{s} = 8\,\text{TeV}$ data recording

Figure 4.3.: The distributions show the mean number of interactions per bunch crossing for the 2011 (left) and 2012 (right) dataset.

4.3.1. Triggers used

The triggers in the $H \to WW$ analysis play an important role since they define the lowest possible lepton p_{T}. For the 2012 $H \to WW^{(*)} \to \ell\nu\ell\nu$ analysis both single- and di-lepton triggers were used. In 2011 the trigger setup used, depends on the data taking period[2]. Only single electron triggers were used in 2011, whereas in the 2012 dataset single and di-lepton triggers were used as a combination. Both were combined with an logical "OR" which means that either a single-, a di-lepton or both are required to have fired. Table 4.1 summarizes the trigger menus used for 2011, Table 4.2 shows the 2012 trigger setup. The numbers in the trigger names represent the p_{T} threshold in GeV. The suffixes *loose*,

[1] The distance from the focus point of the beam where the beam is twice as wide as at the focus point.
[2] A data taking period is usually on the order of a month

medium and *tight* represent the object quality criteria used (see chapter 5) for the trigger object. The object quality criteria used in the trigger setup has no direct influence on the analysis objects. The abbreviation *vh* and *Tvh* for some 2011 and 2012 triggers reflect selection criteria to reduce hadronic leakage. Some of the 2012 triggers have an *i* in the name which indicates the necessity of the trigger object to be isolated [66].

Period	ee channel	$\mu\mu$ channel	eμ channel
B - I	$e\,p_{\mathrm{T}} > 20\,\mathrm{GeV}$, medium	$\mu\,p_{\mathrm{T}} > 18\,\mathrm{GeV}$	$e\,p_{\mathrm{T}} > 20\,\mathrm{GeV}$, medium || $\mu\,p_{\mathrm{T}} > 18\,\mathrm{GeV}$
J	$e\,p_{\mathrm{T}} > 20\,\mathrm{GeV}$, medium	$\mu\,p_{\mathrm{T}} > 18\,\mathrm{GeV}$, medium	$e\,p_{\mathrm{T}} > 20\,\mathrm{GeV}$, medium || $\mu\,p_{\mathrm{T}} > 18\,\mathrm{GeV}$, medium
K	$e\,p_{\mathrm{T}} > 20\,\mathrm{GeV}$, medium	$\mu\,p_{\mathrm{T}} > 18\,\mathrm{GeV}$, medium	$e\,p_{\mathrm{T}} > 20\,\mathrm{GeV}$, medium || $\mu\,p_{\mathrm{T}} > 18\,\mathrm{GeV}$, medium
L - M	$e\,p_{\mathrm{T}} > 22\,\mathrm{GeV}$, vh, medium	$\mu\,p_{\mathrm{T}} > 18\,\mathrm{GeV}$, medium	$e\,p_{\mathrm{T}} > 22\,\mathrm{GeV}$, vh, medium || $\mu\,p_{\mathrm{T}} > 18\,\mathrm{GeV}$, medium

Table 4.1.: Trigger setup for the 7 TeV data set. The notation "||" represents a logical OR.

ee channel	$e\,p_{\mathrm{T}} > 24\,\mathrm{GeV}$, vhi, medium || $e\,p_{\mathrm{T}} > 60\,\mathrm{GeV}$, medium || $2 \cdot e\,p_{\mathrm{T}} > 12\,\mathrm{GeV}$, Tvh, loose
$\mu\mu$ channel	$\mu\,p_{\mathrm{T}} > 12\,\mathrm{GeV}$, tight || $\mu\,p_{\mathrm{T}} > 36\,\mathrm{GeV}$, tight || $\mu\,p_{\mathrm{T}} > 8\,\mathrm{GeV}\&\mu\,p_{\mathrm{T}} > 18\,\mathrm{GeV}$, tight
$e\mu$ & μe channels	$e\,p_{\mathrm{T}} > 24\,\mathrm{GeV}$, vhi, medium || $e\,p_{\mathrm{T}} > 60\,\mathrm{GeV}$, medium || $\mu\,p_{\mathrm{T}} > 24\,\mathrm{GeV}$, i, tight || $\mu\,p_{\mathrm{T}} > 36\,\mathrm{GeV}$, tight || $e\,p_{\mathrm{T}} > 12\,\mathrm{GeV}$, Tvh, medium & $\mu\,p_{\mathrm{T}} > 8\,\mathrm{GeV}$

Table 4.2.: Trigger setup for the 8 TeV data set. The notation "||" represents a logical OR.

The di-lepton triggers were added in 2012 because they allow to lower the leading lepton p_{T} threshold from 25 GeV to 22 GeV. The signal acceptance increases due to the di-lepton triggers and the related loosened lepton p_{T} threshold depending on the lepton flavors. The increase is about 18.5 % in the $\mu\mu$ channel, 9.1 % in the ee channel, 8.3 % in the $e\mu$ channel and 8.2 % in the μe channel [66].

5. Object Definitions

This section describes the object definitions of the $H \rightarrow WW$ analysis. There are no differences in selection criteria between the two separate mass regions $m_H \leq 200\,\text{GeV}$ and $m_H > 200\,\text{GeV}$.

5.1. Electrons

To maximize the sensitivity of the $H \rightarrow WW$ analysis, the selection of leptons has been optimized. Choices on the lepton identification have an impact on the analysis primarily through the rejection of the W+jets and QCD backgrounds with a corresponding trade-off in signal efficiency [66]. The reconstruction of electrons makes use of the inner detector and calorimeter clusters. For a large enough energy deposit in the LAr calorimeter the cluster is matched to a track from the ID. The transverse energy E_{T} of the reconstructed electrons has to be greater than 10 GeV. For the electron identification criteria both approaches, a cut-based and a multivariate technique, are available in ATLAS [66], [67]. Electrons in the $H \rightarrow WW$ analysis use the "Very Tight Likelihood" ("VTLH") definitions for $E_t < 25\,\text{GeV}$ and follow the so called Medium++ cut-based definitions for $E_t > 25\,\text{GeV}$. It is required for all electrons with $|\eta| < 2.37$ to have a hit in the innermost pixel layer, the "b-layer" and the so called conversion flag[1] is required to be false. To further reject W+jets and QCD background, the impact parameter and isolation criteria have been derived as a function of E_t. Discriminating variables on the isolation of a reconstructed electron are:

- the sum of energy deposited in the calorimeter inside a cone[2] of 0.3 in the $\eta - \phi$ plane around the electron: E_T^{cone30}
- the sum of track momentum in a cone of 0.3 or 0.4 around the electron track: p_T^{cone30} and p_T^{cone40}

[1] The conversion flag indicates if it is likely that a photon converted into a pair of electrons. The value of the conversion flag is determined in the ATLAS reconstruction during the track matching of tracks from the inner detector to EM calorimeter deposits.

[2] $\Delta\text{R} = \sqrt{\Delta\eta^2 + \Delta\phi^2}$

For selecting the correct vertex, a requirement on the longitudinal impact parameter $z_0 \cdot \sin\Theta$ (Θ being the angle between the beam axis and the electron track) and on the transverse impact parameter d_0 over the uncertainty on d_0 $\frac{d_0}{\sigma_{d_0}}$ is applied. Table 5.1 summarizes the electron selection criteria for 8 TeV [66], [43].

Table 5.1.: Electron selection as a function of E_T. "CBL" refers to the conversion flag and b-layer hit requirements extended to all η (within the electron acceptance coverage) [66].

E_T (GeV)	electron ID	calo. isolation topoEtConeCor	track isolation Ptcone	impact parameters
10-15	Very Tight LH	$E_T^{cone30}/E_T < 0.20$	$p_T^{cone40}/E_T < 0.06$	$d_0/\sigma_{d_0} < 3.0$, $z_0 \sin\theta < 0.4$ mm
15-20		$E_T^{cone30}/E_T < 0.24$	$p_T^{cone30}/E_T < 0.08$	
20-25		$E_T^{cone30}/E_T < 0.28$	$p_T^{cone30}/E_T < 0.10$	
> 25	Medium++ with "CBL"			

5.2. Muons

Muons are reconstructed via tracks from the inner detector and from the muon spectrometer. The information of both detector parts is combined via the so called STACO algorithm [68] for muon tracks within $|\eta| < 2.5$. Similar to electrons the transverse momentum of muons is required to be greater than 10 GeV. A set of requirements on the quality of inner detector information is applied:

- the sum of hits in the pixel detector and dead pixel sensors crossed by the track must be > 0,
- the sum of SCT hits and dead SCT sensors crossed by the track must be greater than four,
- the number of missing hits in a crossed sensor which is not dead must be less than three,
- a successful TRT extension must be found if the track is within the acceptance of the TRT.

The reconstructed muon is required to fulfill a set of isolation cuts as well as cuts on the impact parameter. The same discriminating isolation variables as for electrons are used for muons. The cuts on the impact parameter help to reject cosmic muons. Table 5.2 summarizes the p_T dependent muon selection [66], [43].

Table 5.2.: Muon selection as a function of E_T [66].

p_T (GeV)	calo. isolation EtConeCor	track isolation Ptcone	impact parameters
10-15	$E_T^{cone30}/E_T < 0.06$	$p_T^{cone40}/E_T < 0.06$	$d_0/\sigma_{d_0} < 3.0$, $z_0 \sin\theta < 1.0$ mm
15-20	$E_T^{cone30}/E_T < 0.12$	$p_T^{cone30}/E_T < 0.08$	
20-25	$E_T^{cone30}/E_T < 0.18$	$p_T^{cone30}/E_T < 0.12$	
> 25	$E_T^{cone30}/E_T < 0.30$		

5.3. Jets

Since the $H \to WW$ analysis is binned in the number of jets (0 jets / 1 jets / $\geq$2 jets), those objects are an important part of the object definitions. Furthermore, identifying a jet as a b-jet originating from a top decay is a crucial part in rejecting the top background.
The nominal analysis jets in the $H \to WW$ analysis are reconstructed following the jet requirements of the anti-k_T 4 LCW+JES collections. The jets are reconstructed from topological clusters in the calorimeters using the anti-k_T algorithm (see section 3.3.3) with a distance parameter $R = 0.4$. The local cluster weighting (LCW) method is applied with the aim to reduce fluctuations in the response of the ATLAS calorimeters. The corrections factors are applied depending on energy density and longitudinal shower depths of the jet. They correct for calorimeter non-compensation, energy losses in non-instrumented regions and signal losses due to threshold effects [66], [43]. So called "LOOSER" jet cleaning cuts are applied on the jets. The jets are required to be within $|\eta| < 4.5$. Jets in the central part of the detector ($|\eta| < 2.4$) are required to have a transverse momentum $p_T > 25\,\text{GeV}$, jets in the forward part of ATLAS ($|\eta| \geq 2.4$) should have a $p_T > 30\,\text{GeV}$. To suppress pile up events, the jet vertex fraction[3] (JVF) is required to be > 0.5 for jets with $p_T < 50$ and $|\eta| < 2.4$. [66]
To identify jets originating from a top quark decay tracking is essential. Due to this, the reconstruction of b-jets is limited to the central part of ATLAS $|\eta| < 2.4$. The MV1 algorithm at a working point of 85% efficiency is applied which uses a multivariate analysis technique seeded from the tracking information to determine if a jet could possibly be a b-jet [43]. In order to maximize the rejection power of the b-veto[4], the p_T threshold for the b-jets is lowered to 20 GeV.

[3] The jet vertex fraction JVF is a discriminating variable between pile up and hard scatter jets, it ranges from zero to one and reflects the probability that the hard jet originated from the primary vertex.
[4] The requirement to have exactly zero b-jets in an event.

5.4. Missing Transverse Energy

Given the event topology of $H \to WW^{(*)} \to \ell\nu\ell\nu$ decays, neutrinos are expected to be present. The ATLAS detector is not able to detect those neutrinos directly. Therefore, the missing transverse energy $\not{E}_{\mathrm{T}}^{\mathrm{miss}}$ is an important observable. Most of the backgrounds in the $e\mu + \mu e$ final state contain neutrinos and hence $\not{E}_{\mathrm{T}}^{\mathrm{miss}}$. In the $ee + \mu\mu$ final state one of the major backgrounds, the Drell-Yan process (Z/DY), does not involve any real neutrinos. In the $H \to WW^{(*)} \to \ell\nu\ell\nu$ analysis many $\not{E}_{\mathrm{T}}^{\mathrm{miss}}$ flavors are investigated. Missing transverse energy can be reconstructed either from the calorimeter (from now referred to as $E_{\mathrm{T}}^{\mathrm{miss}}$), from the tracking ($p_{\mathrm{T}}^{\mathrm{miss}}$) or from the combination of both detector parts ($p_{\mathrm{T}}^{\mathrm{miss,J-TRK}}$). For $p_{\mathrm{T}}^{\mathrm{miss,J-TRK}}$ the jet objects in $p_{\mathrm{T}}^{\mathrm{miss}}$ are replaced by the corresponding calorimeter information [66]. One way to reduce possible effects on $\not{E}_{\mathrm{T}}^{\mathrm{miss}}$ from miss-measured objects (leptons and jets) is to project the missing transverse energy onto a axis defined by the closest hard object:

$$E_{\mathrm{T,rel}}^{\mathrm{miss}} = \not{E}_{\mathrm{T}}^{\mathrm{miss}} \times \sin\Delta\phi \quad \text{, for } \Delta\phi < \frac{\pi}{2}$$
$$E_{\mathrm{T,rel}}^{\mathrm{miss}} = \not{E}_{\mathrm{T}}^{\mathrm{miss}} \quad \text{, otherwise}$$

The angle $\Delta\phi$ here is between the $\not{E}_{\mathrm{T}}^{\mathrm{miss}}$ and the nearest reconstructed analysis object (the same methodology for the relative $\not{E}_{\mathrm{T}}^{\mathrm{miss}}$ is applied to calorimeter based $E_{\mathrm{T}}^{\mathrm{miss}}$ and track based $p_{\mathrm{T}}^{\mathrm{miss}}$ hence $E_{\mathrm{T,rel}}^{\mathrm{miss}}$and $p_{\mathrm{T,rel}}^{\mathrm{miss}}$). For various final states different combinations of MET flavors were chosen based on the following consideration:

- for $e\mu + \mu e$ channels, the $\not{E}_{\mathrm{T}}^{\mathrm{miss}}$ with the best resolution was chosen: $p_{\mathrm{T}}^{\mathrm{miss,J-TRK}}$ [66]
- for $ee + \mu\mu$ channels, the $\not{E}_{\mathrm{T}}^{\mathrm{miss}}$ with the best rejection of Z/DY was chosen: $p_{\mathrm{T,rel}}^{\mathrm{miss}}$ [66]
- for VBF dominant channels, ($N_{\mathrm{jet}} \geq 2$) a combination of calorimeter $E_{\mathrm{T}}^{\mathrm{miss}}$ and $p_{\mathrm{T}}^{\mathrm{miss,J-TRK}}$ gives the best performance [66].

Table 5.3 summarizes the $\not{E}_{\mathrm{T}}^{\mathrm{miss}}$ objects used for the various analysis bins. In the $m_H > 200\,\mathrm{GeV}$ analysis an additional cut on $E_{\mathrm{T}}^{\mathrm{miss}}$ for the $e\mu + \mu e$ VBF channel is introduced.

5.5. Overlap removal

To avoid double counting of objects in the case where two objects were reconstructed closely in the $\eta - \phi$ plane, the following overlap removal strategy is applied:

- For muon-electron overlap within $\Delta R < 0.1$: keep the muon, remove the electron. A

jet bin	$\not{E}_{\mathrm{T}}^{\mathrm{miss}}$ flavour	description
0j $e\mu + \mu e$	$p_{\mathrm{T}}^{\mathrm{miss,J-TRK}}$	track-based $E_{\mathrm{T}}^{\mathrm{miss}}$ with calorimeter jets
0j $ee + \mu\mu$	$p_{\mathrm{T,rel}}^{\mathrm{miss}}$, $E_{\mathrm{T,rel}}^{\mathrm{miss}}$	projections of the track- and calo-based $\not{E}_{\mathrm{T}}^{\mathrm{miss}}$
1j $e\mu + \mu e$	$p_{\mathrm{T}}^{\mathrm{miss,J-TRK}}$	track-based $E_{\mathrm{T}}^{\mathrm{miss}}$ with calorimeter jets
1j $ee + \mu\mu$	$p_{\mathrm{T,rel}}^{\mathrm{miss}}$, $E_{\mathrm{T,rel}}^{\mathrm{miss}}$	projections of the track- and calo-based $\not{E}_{\mathrm{T}}^{\mathrm{miss}}$
2j/VBF $e\mu + \mu e$	only for $m_H > 200\,\mathrm{GeV}$ $E_{\mathrm{T}}^{\mathrm{miss}}$	calo-based $\not{E}_{\mathrm{T}}^{\mathrm{miss}}$
2j/VBF $ee + \mu\mu$	$\not{E}_{\mathrm{T}}^{\mathrm{miss}}$, $p_{\mathrm{T}}^{\mathrm{miss,J-TRK}}$	calo-based and track-based $\not{E}_{\mathrm{T}}^{\mathrm{miss}}$ with calorimeter jets

Table 5.3.: Different $\not{E}_{\mathrm{T}}^{\mathrm{miss}}$ flavours used in the $H \to WW^{(*)} \to \ell\nu\ell\nu$ analysis.

muon passing through the ATLAS detector leaves a relatively small energy deposit in the calorimeters which can be misidentified together the muon track in the ID as an electron.

- In cases of an electron being within $\Delta R < 0.05$ of any muon, the whole event is removed.
- for electron-electron overlap within $\Delta R < 0.3$: keep the electron with higher p_T.
- A high energetic electron can be reconstructed as a jet hence if an electron is within $\Delta R < 0.3$ of a jet candidate: keep the electron, remove the jet.
- For muon-jet overlap within $\Delta R < 0.3$: keep jet, remove muon.

The ΔR is defined in the $\eta - \phi$ metric as $\Delta R = \sqrt{\Delta\eta^2 + \Delta\phi^2}$ [66].

6. The $H \to WW \to \ell\nu_\ell\ell\nu_\ell$ Analysis

The decay channel $H \to WW^{(*)} \to \ell\nu\ell\nu$ is interesting for many reasons. As can be seen in Fig. 2.2 the branching ratio for a Standard Model (-like) Higgs boson decay into two W Bosons is comparatively large over the full mass range. Given the fact that the ATLAS and CMS collaboration both have found a particle with a mass m_H of roughly 125 GeV which is up to this day in full agreement with the SM prediction, the $H \to WW^{(*)} \to \ell\nu\ell\nu$ channel gives an interesting opportunity to measure the Spin properties as well as the size of the couplings of the 125 GeV state. It is worth highlighting here that the $H \to WW^{(*)} \to \ell\nu\ell\nu$ decay channel is one of the three[1] major so called search channels at the LHC. The $H \to WW$ decay channel gives a very clear signal in the detector where two reconstructed leptons, missing transverse energy and depending on the production mechanism 0, 1 or ≥ 2 jets are required.

6.1. Event Topologies

The event topology in $H \to WW^{(*)} \to \ell\nu\ell\nu$ decays mainly depends on four components: production mechanism, decay width, mass and spin[2] of the Higgs boson(-like particle). Independent of those four factors, it is required to have exactly two well reconstructed leptons with different charge in an event and a certain amount of missing transverse energy. The appearance of jets in the events depends on the production mechanism. For the gluon fusion (ggF) process it is expected to have exactly zero jets, for the vector boson fusion (VBF) events with at least two jets are considered. Since jets can be missed in the reconstruction process and since there is the possibility of so called initial state radiation, events with one jet in the final state are also being analyzed. That jet bin is usually dominated by the ggF production. Figure 6.3 shows the jet multiplicity after requiring to have exactly two leptons and a minimum of $m_{\ell\ell}$. The composition of backgrounds varies with the number of jets in the final state.

[1] The other two are $H \to \gamma\gamma$ and $H \to ZZ$

[2] Theoretically the parity of the Higgs boson also plays an important role. But the effect on the event topology from different parity assignments is usually washed out by the detector resolution. To entangle such effects, a specialized analysis which uses multivariate analysis techniques is designed.

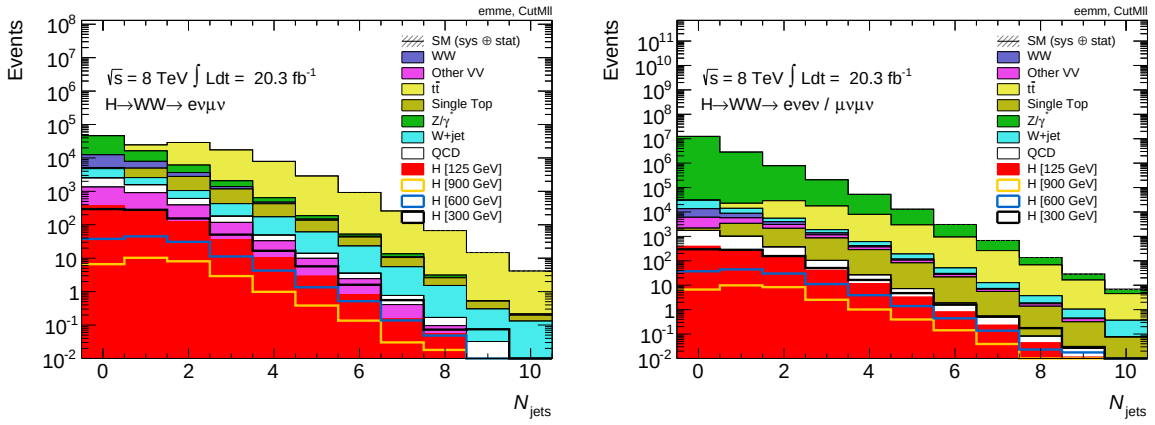

(a) $e\mu + \mu e$ (b) $ee + \mu\mu$

Figure 6.1.: Jet multiplicity at pre-selection level indicating the various background compositions depending on the number of jets in the event. The left plot shows the jet multiplicity for $e\mu + \mu e$ events, the right plot for $ee + \mu\mu$ events. The cuts applied are the pre-selection cuts up to $m_{\ell\ell} > 10, 12\,\text{GeV}$ (see section 6.3).

The two reconstructed leptons in the final state are either electrons or muons. Tauons enter the analyzed events only indirectly via the decays $\tau \to \bar{\nu}_\tau \ell \nu_\ell$ where ℓ can be either an electron or an muon. Given those lepton flavors in the final state the events usually get categorized into two classes:

1. Same flavor events (SF), where both leptons are electrons or muons

2. Different flavor events (DF), where both leptons are of different flavor i.e. one electron and one muon.

The same flavor channel is dominated by Z+jets events originating from the Drell-Yan process (see section 7.4) while in the different flavor channel the top background followed by the Z+jets background play an important role. The irreducible WW background is more or less independent of the final state flavor combination ($e\mu + \mu e$ and $ee + \mu\mu$). Figure 6.2 indicates the dependence of the signal event topology on the Higgs mass m_H as well as the dependence on the spin of the Higgs Boson. The analysis used to investigate the spin will not be discussed in this thesis and further on each Higgs-like boson is supposed to have spin-0.

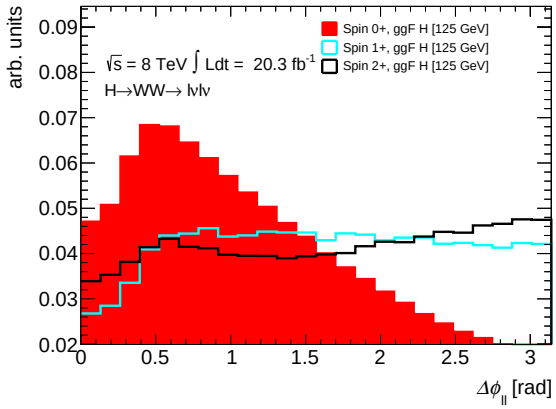

(a) Spin dependence

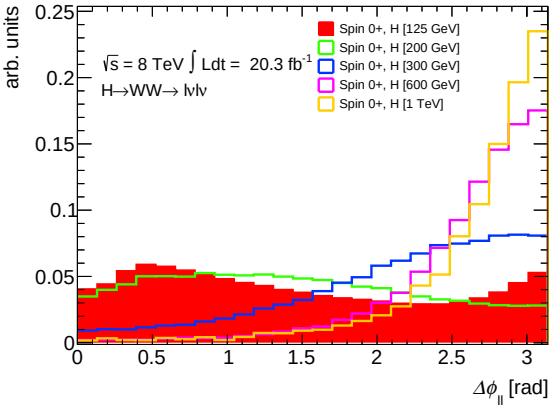

(b) Mass dependence

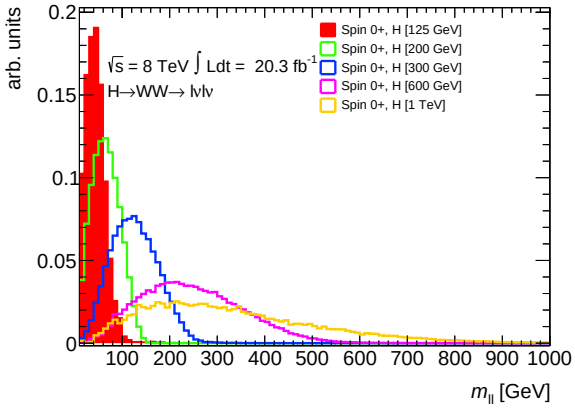

(c) Mass dependence

Figure 6.2.: The distributions show the opening angle of the two leptons in the final state in the transverse plane $\Delta\phi_{\ell\ell}$ for various spin hypothesis and various Higgs boson masses. In the distribution indicating the spin dependence Fig. 6.2a, only signal produced via the gluon fusion process is shown. In addition the invariant dilepton mass $m_{\ell\ell}$ is shown for various Higgs Boson masses. All distributions are normalized to unity. It is evident that the event topology varies with m_H as well as with the spin of the Higgs boson.

Two possible scenarios are analyzed in this thesis in which further Higgs like bosons are added to the particle content of the Standard Model (see section 2.4). The major difference between the signals of the SM-like Higgs boson, the NWA scenario and the EWS scenario is the decay width Γ of the Higgs like particle for a mass m_{H}. With an increasing decay width, the influence of the interference between the signal and the non-resonant WW background gets more dominant for the SM-like and the EWS scenario. In Figure 6.3 this relationship is illustrated. The plot shows the transverse mass m_{T} distribution (see section 6.2) for a SM-like Higgs signal and a NWA signal with a mass

of $m_{\mathrm{H}} = 300\,\mathrm{GeV}$, $600\,\mathrm{GeV}$ and $1\,\mathrm{TeV}$. The SM-like scenario and the NWA scenario are the two extreme cases in the terms of width of the signal. Due to the increasing decay width of the SM-like signal, the interference between the signal and the non-resonant WW background gets more dominant which affects the shape as well as the production cross section of the signal process. The signal is shifted towards smaller values in m_{T} due to the interference.

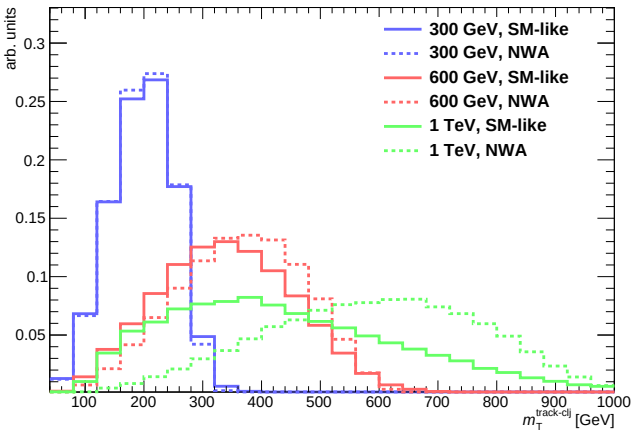

Figure 6.3.: Transverse mass for a SM-like Higgs signal and a NWA signal for the masses $m_{\mathrm{H}} = 300\,\mathrm{GeV}$, $600\,\mathrm{GeV}$ and $1\,\mathrm{TeV}$. The distributions are normalized to unity.

6.2. Kinematic variables

In order to discriminate a signal from background events, a set of kinematic variables is used. Moreover, some variables are needed to separate control regions from signal regions. This section should help to highlight the most important variables in the $H \to WW^{(*)} \to \ell\nu\ell\nu$ analyses. All distributions presented in this chapter show in the last bin of any histogram the integrated number of events from the lower bin boundary of the last bin up to infinity.

- **Lepton transverse momentum p_{T}:**

  Since one is looking at events with two leptons in the final state, the transverse momenta p_T of the two individual leptons is a very important variable. Especially if looking at higher Higgs masses, cutting harder on this variable can help to reject background events. On the other hand, if going to lower masses or trying to analyze the 125 GeV state respectively, the cut on the lepton p_{T} is required to be as soft as possible. In Figure 6.4 the leading and sub-leading lepton p_{T}

distributions are shown for the different and same flavor category. The pre-selection cuts up to $m_{\ell\ell} > 10,12\,\text{GeV}$ (see section 6.3) are applied to the MC events in those distributions.

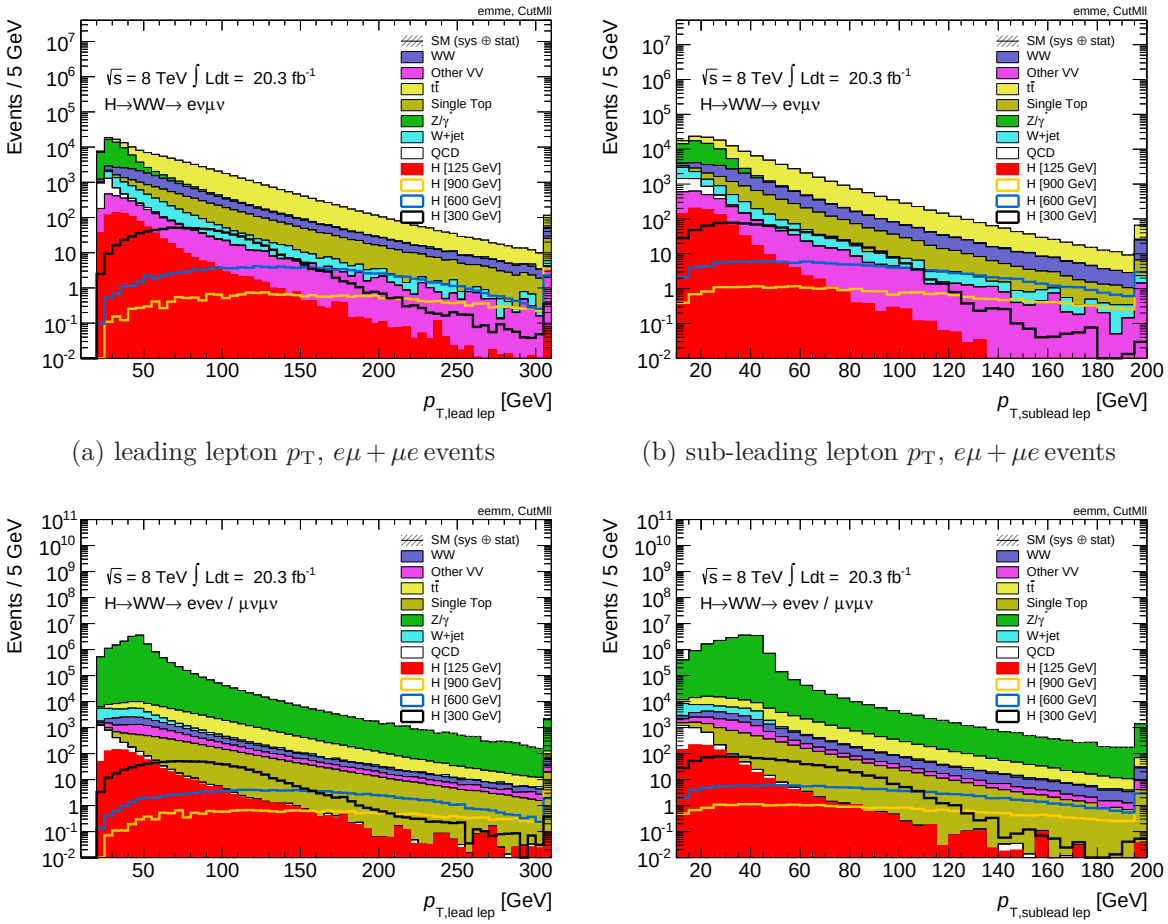

(a) leading lepton p_{T}, $e\mu + \mu e$ events

(b) sub-leading lepton p_{T}, $e\mu + \mu e$ events

(c) leading lepton p_{T}, $ee + \mu\mu$ events

(d) sub-leading lepton p_{T}, $ee + \mu\mu$ events

Figure 6.4.: The distributions show the leading and sub-leading lepton p_{T} for the different flavor (upper row) and same flavor category (lower row). The cuts applied are the pre-selection cuts up to the cut on $m_{\ell\ell} > 10,12\,\text{GeV}$ (see section 6.3).

- **Dilepton transverse momentum $p_T^{\ell\ell}$:**

  The reconstructed four vectors of the individual leptons $\begin{pmatrix} E^{\ell} \\ \overrightarrow{p^{\ell}} \end{pmatrix}$ are added to define the four vector of the dileptonic system $\begin{pmatrix} E^{\ell\ell} \\ \overrightarrow{p^{\ell\ell}} \end{pmatrix}$. From the four vector of the dileptonic system one can obtain the transverse momentum. The dilepton transverse

momentum is shown in Figure 6.5 for different and same flavor.

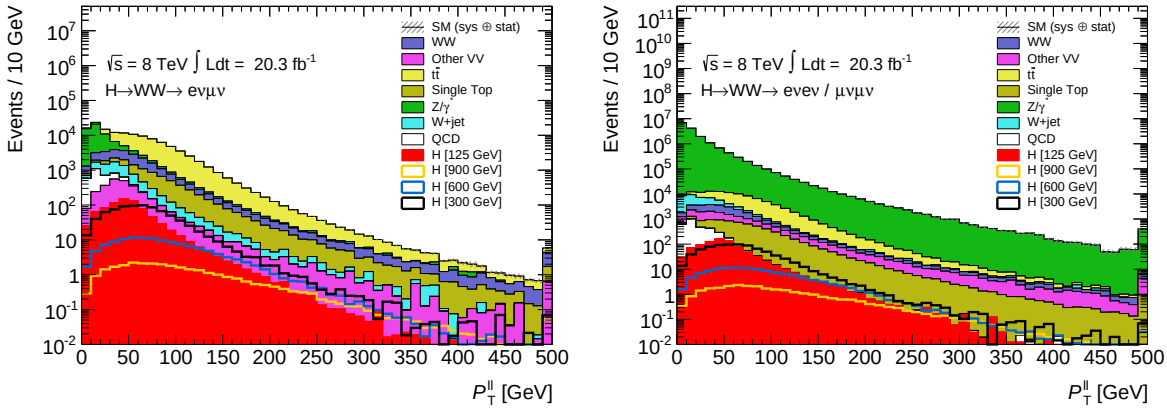

(a) $p_T^{\ell\ell}$ in $e\mu + \mu e$ events

(b) $p_T^{\ell\ell}$ in $ee + \mu\mu$ events

Figure 6.5.: The distributions show the transverse momentum of the dileptonic system $p_T^{\ell\ell}$ for the different flavor (left) and same flavor category (right). The cuts applied are the pre-selection cuts up to the cut on $m_{\ell\ell} > 10, 12\,\text{GeV}$ (see section 6.3).

- **Invariant dilepton mass $m_{\ell\ell}$:**

  The invariant dilepton mass $m_{\ell\ell} = \sqrt{(E_1^\ell + E_2^\ell)^2 - (\vec{p}_1^{\,\ell} + \vec{p}_2^{\,\ell})^2}$ is of course helpful to reject background events but also to define control regions for various Standard Model backgrounds. For small m_H[3] the signal is usually broadly distributed in the $m_{\ell\ell}$ range below $m_H/2$. In Figure 6.6 the dilepton invariant mass is shown for same and different flavor events. In the same flavor case, the Z-peak is visible which is removed via the Z-window cut which helps to reject about 80 % of the Z/DY background. With an increasing mass, the signal is distributed more uniformly in $m_{\ell\ell}$.

[3] $m_H < 200\,\text{GeV}$

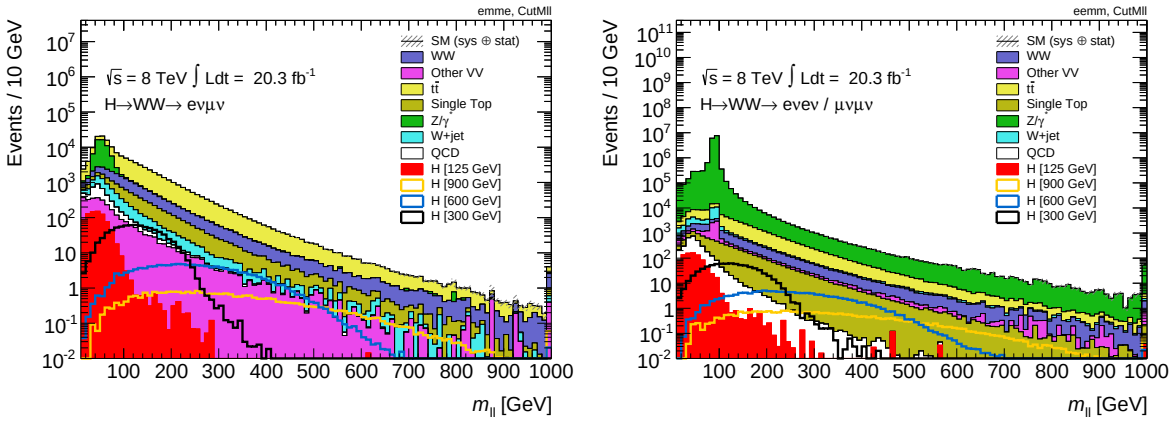

(a) $m_{\ell\ell}$ in $e\mu + \mu e$ events

(b) $m_{\ell\ell}$ in $ee + \mu\mu$ events

Figure 6.6.: The distributions show the dilepton invariant mass $m_{\ell\ell}$ for the different flavor (left) and same flavor category (right). The cuts applied are the pre-selection cuts up to the cut on $m_{\ell\ell} > 10, 12\,\text{GeV}$ (see section 6.3).

- **Missing transverse energy $\not{E}_{\text{T}}^{\text{miss}}$:**

  Since two undetectable neutrinos are expected in the signal events, a minimal amount of $\not{E}_{\text{T}}^{\text{miss}}$ in the event is required. Especially in the SF case the Z/DY background can be rejected very efficiently via a cut on $\not{E}_{\text{T}}^{\text{miss}}$. The transverse missing energy can be measured via either the information obtained from the calorimeters or from the information of the tracker. Both approaches are used in the $H \to WW^{(*)} \to \ell\nu\ell\nu$ analysis. Both the track and the calorimeter based $\not{E}_{\text{T}}^{\text{miss}}$ is shown in Figure 6.7 for $e\mu + \mu e$ and $ee + \mu\mu$ events. The cuts applied are the pre-selection cuts (see section 6.3) up to the cut on $m_{\ell\ell} > 10, 12\,\text{GeV}$. The signal of a heavy Higgs like particle is broadly distributed in $\not{E}_{\text{T}}^{\text{miss}}$ while some of the background processes tend towards small values in $\not{E}_{\text{T}}^{\text{miss}}$.

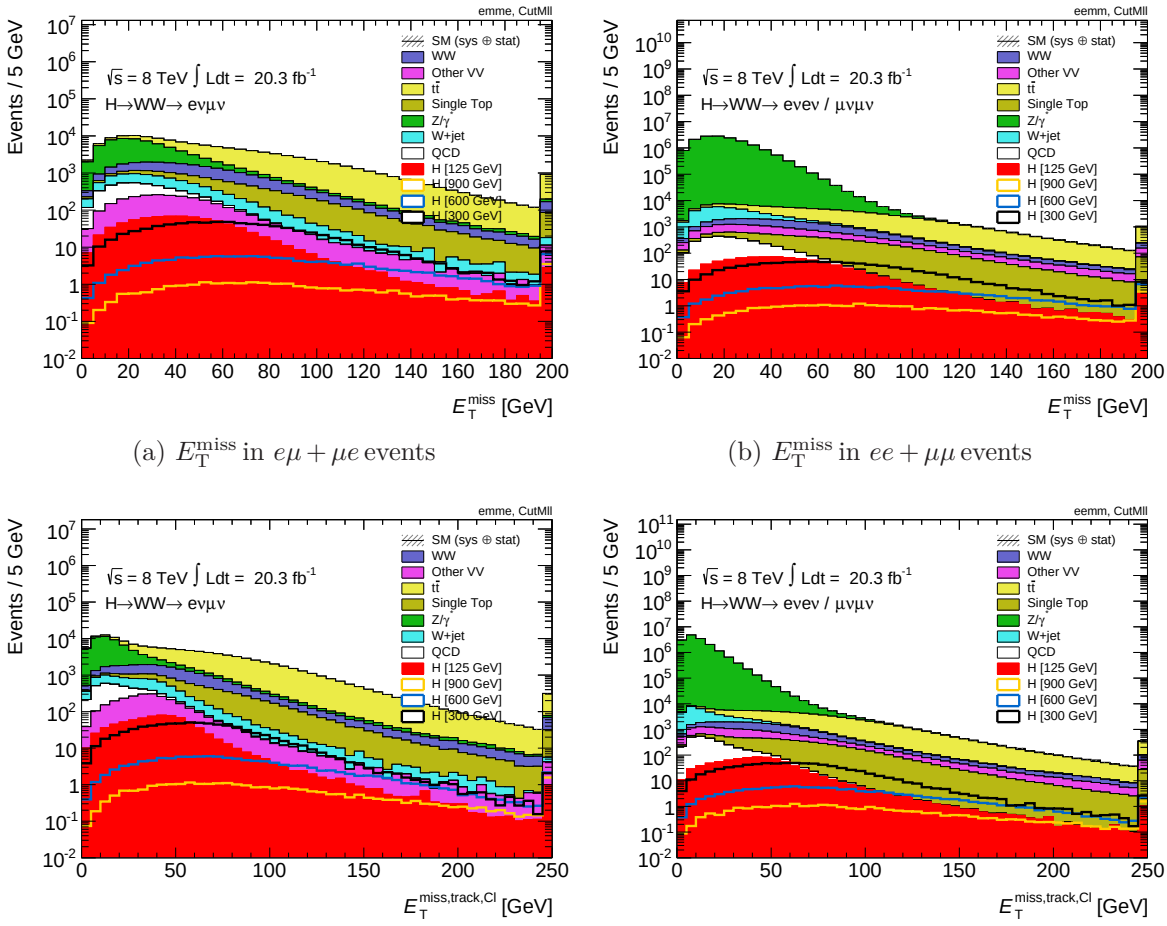

(a) $E_{\mathrm{T}}^{\mathrm{miss}}$ in $e\mu + \mu e$ events

(b) $E_{\mathrm{T}}^{\mathrm{miss}}$ in $ee + \mu\mu$ events

(c) $p_{\mathrm{T}}^{\mathrm{miss}}$ in $e\mu + \mu e$ events

(d) $p_{\mathrm{T}}^{\mathrm{miss}}$ in $ee + \mu\mu$ events

Figure 6.7.: The distributions show the calorimeter based $\not{E}_{\mathrm{T}}^{\mathrm{miss}}$ (upper row) and the track based $\not{E}_{\mathrm{T}}^{\mathrm{miss}}$ (lower row) for same (left) and different flavor (right) events. The cuts applied are the pre-selection cuts up to the cut on $m_{\ell\ell} > 10,12\,\mathrm{GeV}$ (see section 6.3).

- **Difference in pseudorapidity of leptons $\Delta\eta_{\ell\ell}$:**

  Since a data driven estimate of the dominant, irreducible WW background is performed (see section 7), $\Delta\eta_{\ell\ell}$ can be used to orthogonalize the WW control regions from signal regions. The difference of pseudorapidity is used for the analysis of heavier Higgs bosons. Here the signal shows up in the same $m_{\ell\ell}$ regions as the WW background and therefore a separation of signal and control regions is no longer possible via $m_{\ell\ell}$. The $H \to WW$ signal tends to have small values of $\Delta\eta_{\ell\ell}$. In Figure 6.8 $\Delta\eta_{\ell\ell}$ is shown for $e\mu + \mu e$ and $ee + \mu\mu$ events after the cut on $m_{\ell\ell} > 10,12\,\mathrm{GeV}$ (see section 6.3).

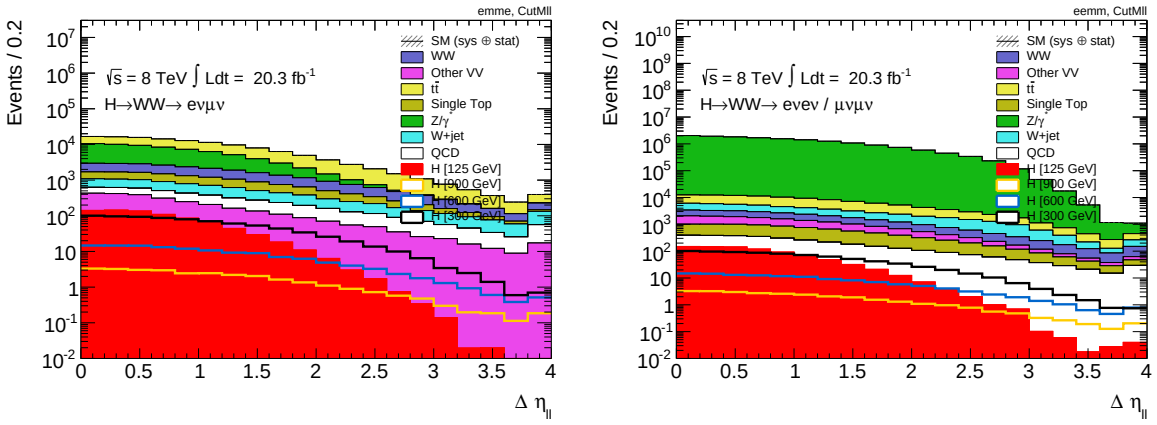

(a) $\Delta\eta_{\ell\ell}$ in $e\mu + \mu e$ events

(b) $\Delta\eta_{\ell\ell}$ in $ee + \mu\mu$ events

Figure 6.8.: The distributions show the difference in lepton pseudorapidity $\Delta\eta_{\ell\ell}$ for the different flavor (left) and same flavor category (right). The cuts applied are the pre-selection cuts up to the cut on $m_{\ell\ell} > 10,12\,\text{GeV}$ (see section 6.3).

- **Invariant di-tau mass $m_{\tau\tau}$:**

  The invariant di-tau mass can be constructed if it is assumed that the observed charged lepton originating from the decay of a τ lepton is collinear with the emitted neutrinos. The neutrinos from such $\tau \to \ell\nu_\ell\nu_\tau$ decays are then the only source of real $\not{E}_{\text{T}}^{\text{miss}}$ in such events. The energy fractions x_1 and x_2 of the neutrinos in $\tau\tau \to \ell\nu_\ell\nu_\tau\ell\nu_\ell\nu_\tau$ events (where ℓ can be either a electron or a muon) can be computed using the measured transverse momenta of the reconstructed leptons and the reconstructed $\not{E}_{\text{T}}^{\text{miss}}$. If both x_1 and x_2 are greater than zero (e.g. real neutrinos), the invariant di-tau mass is defined as

$$m_{\tau\tau} = \frac{\sqrt{(E_1 + E_2)^2 - (p_1 + p_2)^2}}{\sqrt{x_1 \cdot x_2}}, \tag{6.1}$$

  where E_1 and E_2 are the measured energies of the leading and sub-leading lepton and p_1 and p_2 are the momenta of the leading and sub-leading lepton (electrons or muons) [69].

- **Transverse mass m_{T}:**

  Owing to the fact that one is not able to reconstruct the two neutrinos in the final state of the $H \to WW^{(*)} \to \ell\nu\ell\nu$ analyses, it is not possible to reconstruct the invariant mass of the full final state. Therefore the $H \to WW^{(*)} \to \ell\nu\ell\nu$ analysis

makes use of the so called transverse mass:

$$m_T = \sqrt{(E_T^{\ell\ell} + P_T^{\nu\nu})^2 - |\vec{P}_T^{\ell\ell} + \vec{P}_T^{\nu\nu}|^2}, \tag{6.2}$$

where $E_T^{\ell\ell} = \sqrt{(P_T^{\ell\ell})^2 + (m_{\ell\ell})^2}$. The neutrino kinematic entering the transverse mass definition is equivalent to the $\not{E}_{\mathrm{T}}^{\mathrm{miss}}$ information in the event. The $\not{E}_{\mathrm{T}}^{\mathrm{miss}}$ information used is obtained from the track-based missing transverse energy. No cut is applied to this variable but a fit of this distribution is performed to extract exclusion limits and measure the couplings of the 125 GeV Standard Model Higgs boson (see chapter 9) and obtain upper limits on the production cross section times branching ratio for heaver Higgs like states. The m_{T} distribution is shown in Figure 6.11 after the pre-selection cuts for $e\mu + \mu e + ee + \mu\mu$ events. In the Figures 6.12, 6.13 and 6.14 - 6.16 the transverse mass in the various signal regions is presented[4].

- **Opening angle of leptons $\Delta\phi_{\ell\ell}$:**

  Due to the spin-0 nature of the Higgs boson, the opening angle of the leptons tends to small values for masses $m_H < 200\,\mathrm{GeV}$. The Higgs decaying into two spin-1 W bosons with opposite spins which sequentially decay into leptons with aligned spins. Since the decay of the W boson has a V-A structure, the opening angle of the charged leptons have a small opening angle in the laboratory frame (see Fig. 6.10) [70]. For the high mass analysis the background rejection efficiency of $\Delta\phi_{\ell\ell}$ is relatively small due to the boost of the two W-bosons. Figure 6.9 shows the opening angle of the two leptons for different and same flavor events. The applied cuts are the pre-selection cuts up to $m_{\ell\ell} > 10, 12\,\mathrm{GeV}$ (see section 6.3).

[4] In all m_{T} distributions presented in this work, the x-axis is labeled with $m_{\mathrm{T}}^{\mathrm{track-clj}}$. The superscript track-clj refers to the definition of $\not{E}_{\mathrm{T}}^{\mathrm{miss}}$ used in the m_{T} calculation. The so called jet corrected track $\not{E}_{\mathrm{T}}^{\mathrm{miss}}$ $p_{\mathrm{T}}^{\mathrm{miss,J-TRK}}$ is used in all distributions (see section 5.4)

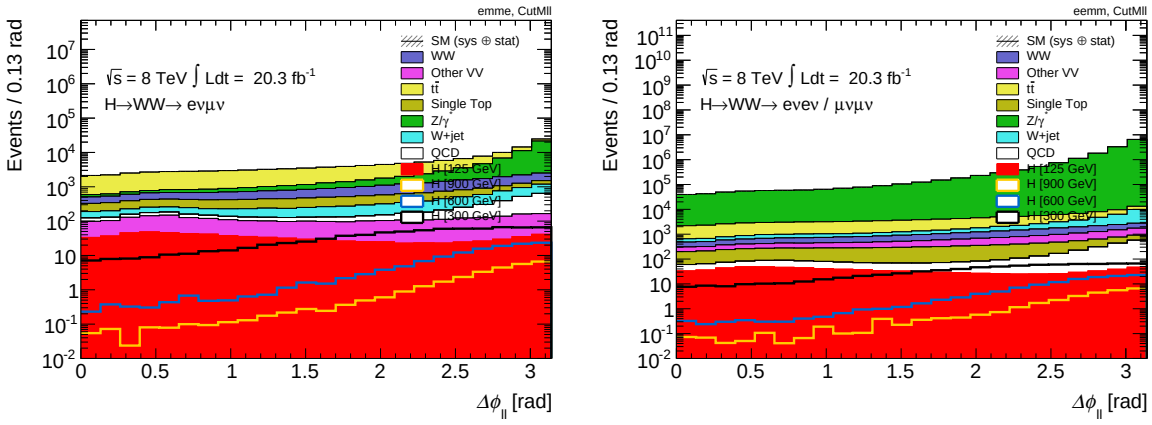

(a) $\Delta\phi_{\ell\ell}$ in $e\mu + \mu e$ events

(b) $\Delta\phi_{\ell\ell}$ in $ee + \mu\mu$ events

Figure 6.9.: The distributions show the opening angle of the two leptons for the different flavor (left) and same flavor category (right). The cuts applied are the pre-selection cuts up to the cut on $m_{\ell\ell} > 10,12\,\text{GeV}$ (see section 6.3).

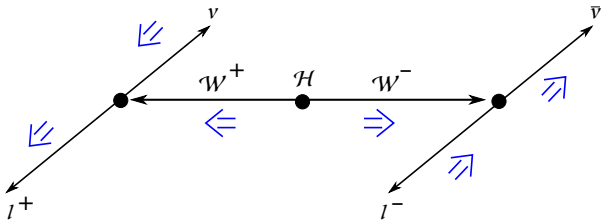

Figure 6.10.: Illustration of the spin alignment of the leptons originating from the $H \to WW$ decay. The small arrows indicate the momenta and the large double arrays indicate the spins of the particles in the decay [70].

- **Fractional jet recoil - f_{recoil} :**

  Events from $Z/\gamma^* \to ee/\mu\mu$ events which pass $\not{E}_{\text{T}}^{\text{miss}}$ and $p_T^{\ell\ell}$ requirements as in the low mass 0 and 1 jet analysis, have two boosted, close-by leptons with low invariant mass. The measured missing transverse energy in those events is fake since there are no true neutrinos in those events to balance the dilepton system. The two lepton system must be balanced by a hadronic recoil. The soft recoil system is reconstructed as the vector sum p_{T} of soft jets below the analysis jet threshold but with $E_{\text{T}} > 10\,\text{GeV}$ and $|\eta| < 4.5$. The jets are required to be in the transverse quadrant opposite the dilepton system ($\frac{3\pi}{4} < \Delta\phi(\ell\ell, \text{soft-jets}) < \frac{5\pi}{4}$). The f_{recoil} variable measures the strength of the recoil system relative to the dileptonic system. The vectorial sum of the soft jet p_{T} is weighted by the jet-vertex

fraction in order to reduce the influence of soft jets from pile-up.

$$f_{\text{recoil}} = \frac{|\sum_{\text{soft-jets}} |\text{JVF}| \cdot \vec{p_{\text{T}}}|}{p_{\text{T}}^{\ell\ell(+\text{hardjet})}} \tag{6.3}$$

The quantity $p_{\text{T}}^{\ell\ell(+\text{hardjet})}$ represents the total transverse momentum of the dilepton system in the $N_{\text{jets}} = 0$ bin and the total transverse momentum of the two leptons plus the jet in the $N_{\text{jets}} = 1$ bin [69].

- **Jet multiplicity N_{jets}:**

  As previously discussed to distinguish between the two dominant Higgs Boson production mechanisms, the analyses are separated in jet bins. This also varies the background composition.

- **Rapidity difference for jets ΔY_{jj} and invariant Jet mass m_{jj}:**

  For the VBF category ($\geq$ 2 jets in the event) one can also make use of di-jet variables like ΔY_{jj} and m_{jj}. The two jets originating from the VBF production process tend to be hard forward jets.

6.3. Pre-selection of Events

In order to select events suitable for the $H \to WW^{(*)} \to \ell\nu\ell\nu$ analyses, a set of pre-selection cuts are applied. Those selection criteria will be described briefly in the following:

- Data quality: Events which are not from good luminosity blocks or good runs are removed (see section 4.3)

- Good vertex: It is required that the primary vertex in the event is associated with at least three tracks.

- Event cleaning: Events with a so called "bad jet" are rejected if the bad jet has a transverse momentum of $p_{\text{T}} > 20\,\text{GeV}$. Bad jets are objects which fulfill the jet criteria but their source can be either hardware problems, beam halo, beam conditions or cosmic ray showers [71]. Those events are rejected since the measurement of $\not{E}_{\text{T}}^{\text{miss}}$ might not be trustworthy. Only about 0.01% of the events in the 8 TeV dataset are removed by these criteria.

- LAr noise bursts: In the liquid Argon calorimeters of ATLAS noise bursts can occur which are automatically flagged by the ATLAS software [71]. Events which such LAr noise bursts are removed from the analysis.

- Tile Cleaning: In a few runs during the 8 TeV proton-proton data taking the tile calorimeter had some defective detector cells. If a reconstructed jet in an event pointed towards such a defective calorimeter region, the event is removed.

- Trigger requirements: It is required that at least one of the for $H \to WW^{(*)} \to \ell\nu\ell\nu$ analyses typical triggers (see section 4.3.1) has fired.

- Trigger matching: It is required that one or both of the reconstructed leptons have fired the single- or di-lepton trigger. This is realized via matching the reconstructed leptons to the trigger objects inside a cone $\Delta R = \sqrt{\Delta\eta^2 + \Delta\phi^2} < 0.15$.

- Stream overlap: It is possible that an event is stored in both the "muon stream" and the "electron stream". Those data streams are fed by the electron or muon triggers. If an event is found in both streams, the event is only used from the "muon stream".

- Two OS good leptons: Since the $H \to WW^{(*)} \to \ell\nu\ell\nu$ signal requires two oppositely charged leptons, only events with exactly two leptons fulfilling the object requirements described in section 5.1 and 5.2 are analyzed. Furthermore, the two leptons are required to have different electric charge. The lepton p_{T} of the leading lepton is required to be greater than 22 GeV and the p_{T} of the sub-leading lepton should be greater than 10 GeV.

- $m_{\ell\ell} > 10, 12\,\mathrm{GeV}$: To remove meson resonances at low $m_{\ell\ell}$, only events with an invariant dilepton mass greater than 10 GeV for $e\mu + \mu e$ events and greater than 12 GeV for $ee + \mu\mu$ events are analyzed.

- Z-Veto: In the same flavor case ($ee + \mu\mu$) all events with a dilepton invariant mass $m_{\ell\ell}$ within 15 GeV of the mass of the Z-Boson[5] are rejected. This requirement removes a big fraction (about 88 %) of Z+jets events.

This set of pre-selection criteria are satisfied by 2,150,203 events from the 2012 ATLAS data taking. Figure 6.11 shows the transverse mass m_{T} (see section 6.2) for data, Monte Carlo events and the data-driven W+jets and QCD background estimations after the pre-selection cuts. The background is dominated at this stage by Z+jets events followed by the $t\bar{t}$ background.

[5] $m_{\mathrm{Z}} = 91.187 \pm 0.0021\,\mathrm{GeV}$ [17]

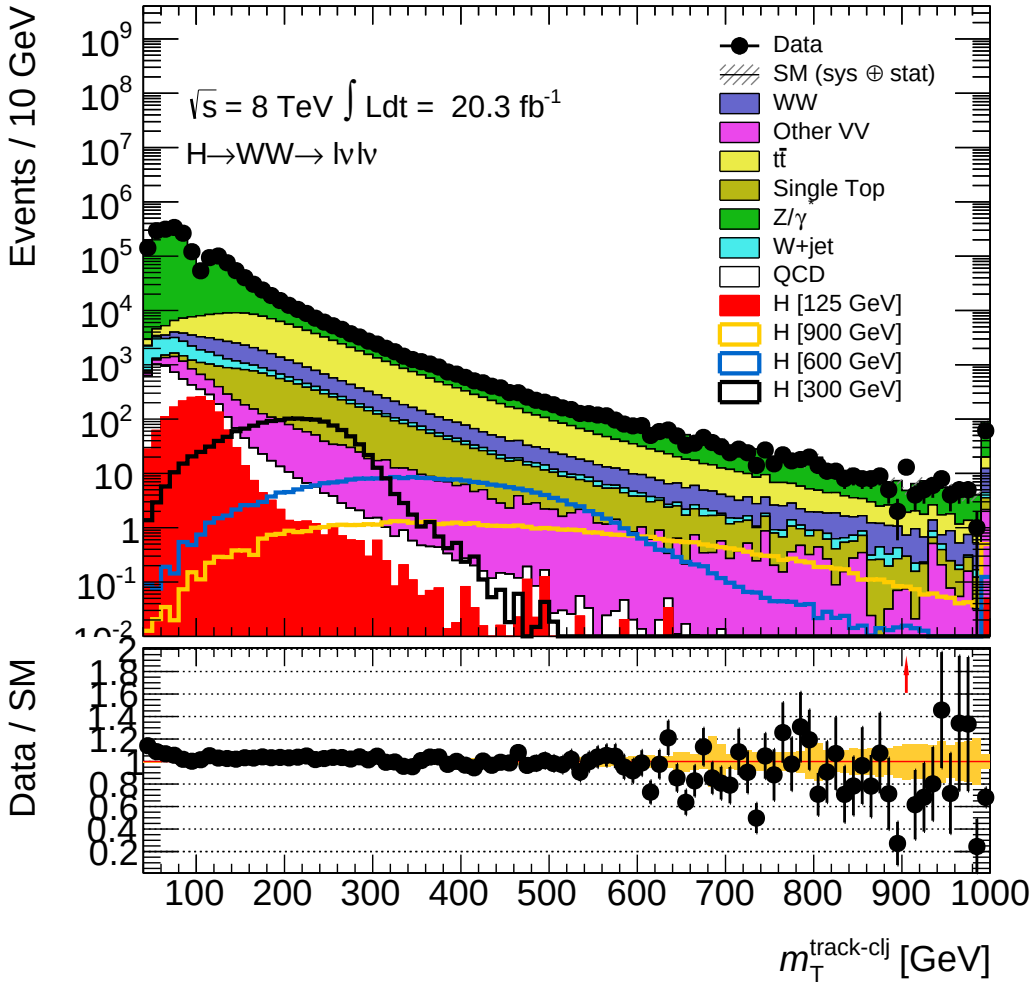

Figure 6.11.: m_{T} for $\ell\ell$ after the pre-selection cuts are applied to the 8 TeV dataset and the Monte Carlo events. The W+jets and QCD background are taken from the data-driven estimates.

6.4. Signal region selection

As indicated in section 6.1, the phase space in which signal arising from a Standard Model Higgs Boson[6] is expected, depends on the mass of the particle (which can also be seen in Fig. 6.11). Therefore, the signal region selection in the $H \to WW^{(*)} \to \ell\nu\ell\nu$ analysis is divided into two categories:

[6] A massive, neutral, spin-0 particle with branching ratios as presented in Figure 2.2 and production cross-sections as shown if Figure 2.4

- The so called low mass (or couplings) analysis which is optimized for Higgs bosons with a mass between $114\,\text{GeV} < m_H \leq 200\,\text{GeV}$. Given the fact that both the ATLAS and the CMS collaboration have discovered a resonance at around 125 GeV, all optimization efforts in the low mass analysis were performed in order to increase the signal acceptance for a Standard Model Higgs Boson with a mass of ≈ 125 GeV.

- The high mass analysis which is optimized to search for Standard Model (-like) Higgs Bosons with masses between $200\,\text{GeV} \leq m_H \leq 1\,\text{TeV}$ (2 TeV NWA). As discussed in section 2.4, some extensions of the Standard Model require further, heavier bosons which resemble the Standard Model Higgs boson. Furthermore, exploring the full mass range can help establishing the resonance at roughly 125 GeV as the Standard Model Higgs boson. The high mass analysis is also used to explore two non Standard Model scenarios: EWS and NWA (see chapter 2.4).

The two following sections will summarize the signal region selections for the low and the high mass analysis.

6.4.1. Event selection for $m_H \leq 200\,\text{GeV}$

The background composition as well as the dominant Higgs Bosons production mechanism depend on the number of jets in the event. For events with 0 and 1 jet the $H \to WW^{(*)} \to \ell\nu\ell\nu$ signal is mainly produced via the gluon fusion process. In the category with 1 jet, the jet in the signal process is mainly due to initial state radiation, but also misidentified vector boson fusion signal can appear in this bin. In events with $N_{\text{jets}} \geq 2$ jets signal produced via VBF becomes accessible. Since signal and background composition highly depend on the number of jets, the signal region selection of both analyses (low and high mass) depends on the number of jets in the event.

Selection for N_{jets}= 0
In events with 0 jets after the pre-selection cuts, the dominant background is Z+jets for same flavor. In the different flavor case the dominant background is WW but also $Z \to \tau\tau + \gamma/\text{jets}$ is not negligible. To further separate the (ggF dominated) signal from the background processes, the following selection cuts are applied:

- $p_{\text{T}}^{\text{miss}} > 20\,\text{GeV}$ for $e\mu + \mu e$ events and $E_{\text{T,rel}}^{\text{miss}} > 40\,\text{GeV}$ for $ee + \mu\mu$ events. A minimum of missing transverse energy is required since two neutrinos are expected in $H \to WW^{(*)} \to \ell\nu\ell\nu$ events.

- The invariant mass of the two leptons $m_{\ell\ell}$ is required to be smaller than 55 GeV.

- The opening angle in the transverse plane of the two leptons $\Delta\phi_{\ell\ell}$ is required to

be less than 1.8 radians.

- The total transverse momentum of the two leptons $p_T^{\ell\ell}$ has to be greater than 30 GeV.

- The opening angle between the transverse missing energy and the dilepton system $\Delta\phi_{\ell\ell,\not{E}_{\mathrm{T}}^{\mathrm{miss}}}$ is required to be greater than $\pi/2$. This cut helps to remove pathological events where the missing transverse energy points in the same direction as one of the leptons. For signal, only about 1% of the events are rejected which means only background is reduced efficiently by this requirement.

- For $ee+\mu\mu$ events cuts on $f_{\mathrm{recoil}} < 0.1$ and $p_{\mathrm{T}}^{\mathrm{miss}} > 40$ GeV are applied to further reduce Z+jets background.

In Figure 6.12 the transverse mass distributions for same flavor and different flavor in low mass 0 jet signal region are shown. The WW background is irreducible and is the dominant background in both cases (same flavor and different flavor). It contributes roughly 72 % to the total background in $ee+\mu\mu$ events and about 64 % for $e\mu+\mu e$ events. For the total background in the 0 jet signal region 1096 ± 8 (stat.) events are expected for same flavor and 2351 ± 10 for different flavor (see Table 6.1 & 6.2).

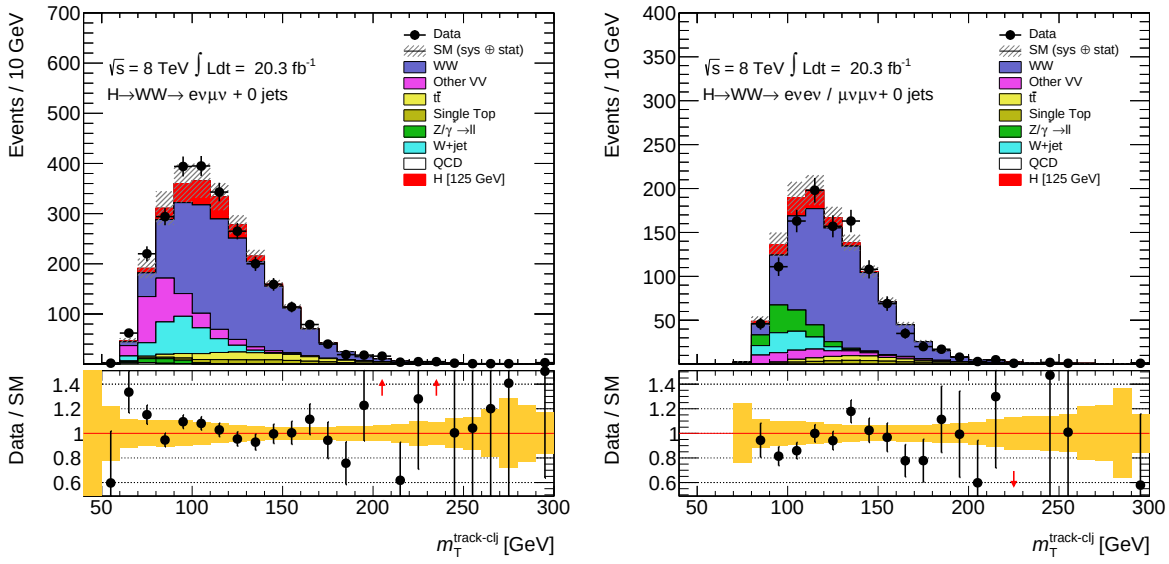

(a) different flavor 0 jet signal region

(b) same flavor 0 jet signal region

Figure 6.12.: The distributions show the transverse mass m_{T} in the 0 jet signal region for same flavor (left) and different flavor (right). All normalization factors which are obtained from the control regions are applied (see chapter 7).

Selection for N_{jets}= 1
In the $N_{\text{jets}} = 1$ category the same flavor case is also dominated by Z+jets but also $t\bar{t}$+ single-top contributes strongly to the background composition. In different flavor events the top background is dominant followed by $Z \to \tau\tau + \gamma$/jets. The additional signal region selection cuts are:

- $p_{\text{T}}^{\text{miss}} > 20\,\text{GeV}$ for $e\mu + \mu e$ events and $E_{\text{T,rel}}^{\text{miss}} > 40\,\text{GeV}$ for $ee + \mu\mu$ events.
- It is required to have no jet which was tagged as a b-jet (see section 5.3) with a transverse momentum of $p_{\text{T}} > 20\,\text{GeV}$ in the event. This reduces the top background very efficiently. Only $\approx 20\%$ of the top background survive this cut.
- To reject $Z \to \tau\tau$ events a cut on $m_{\tau\tau} > (m_Z - 25\,\text{GeV})$ is implemented.
- $\max\{m_T(\ell, \not{E}_{\text{T}}^{\text{miss}})\} > 50\,\text{GeV}$ in $e\mu + \mu e$ events which efficiently rejects QCD background.
- The same cuts on $m_{\ell\ell}$ and $\Delta\phi_{\ell\ell}$ as in the N_{jets}= 0 are applied: $m_{\ell\ell} < 55\,\text{GeV}$, $\Delta\phi_{\ell\ell} < 1.8$.
- To further reject Z+jets cuts on $f_{\text{recoil}} < 0.1$ and $p_{\text{T}}^{\text{miss}} > 35$ GeV are required.

In Figure 6.13 the transverse mass distributions in the low mass 1 jet signal region are shown separately for different flavor and same flavor. Moreover, in 1 jet the WW background is irreducible and is about 47 % of the total background for same flavor and 40 % for different flavor. The second dominant background in the 1 jet case is top and contributes about 35 % in same flavor and 36 % in different flavor to the total background. The total background is 404 ± 4 (stat.) for same flavor and 1030 ± 6 for different flavor in the 1 jet signal region (see Table 6.1 & 6.2).

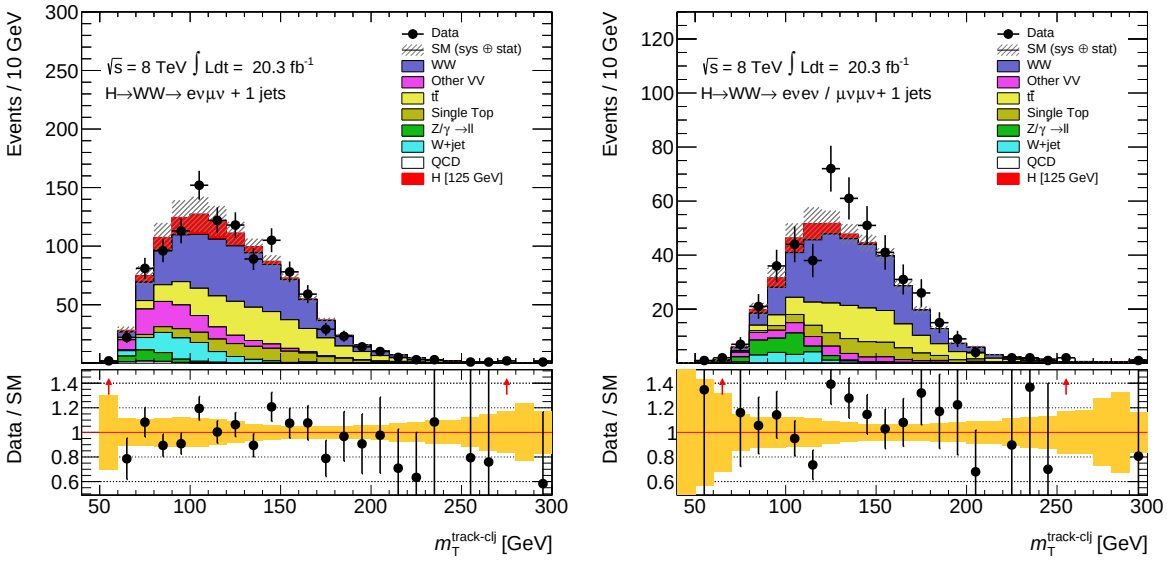

(a) different flavor 1 jet signal region

(b) same flavor 1 jet signal region

Figure 6.13.: The distributions show the transverse mass m_{T} in the 1 jet signal region for same flavor (left) and different flavor (right). All normalization factors which are obtained from the control regions are applied (see chapter 7).

In the Tables 6.1 and 6.2 the cutflows for the 0 and 1 jet signal regions are shown separately for $e\mu + \mu e$ and for $ee + \mu\mu$ events.

Selection for $N_{\mathrm{jets}} \geq 2$

The low mass $N_{\mathrm{jets}} \geq 2$ or VBF analysis follows a different approach than the low mass 0 and 1 jet analysis. Whereas in the low mass 0 and 1 jet a shape fit of the m_{T} distribution is performed[7], the low mass VBF analysis uses a boosted decision tree (BDT) score to extract limits and measure the strength of couplings to the Standard Model Higgs Bosons. Since the low mass VBF analysis is not part of this thesis, it will be described only very briefly, more information can be found in Ref. [70] and Ref. [66].

A boosted decision tree is a multivariate analysis technique. Decisions trees are a collection of cuts which are used to classify events as signal-like or background-like. Once a decision tree is defined, another tree "is grown" to better separate signal-like from background-like events which were misidentified by the first one. This iterative step is repeated until a specified number of trees is present. The iterative growing of decision trees is known- as *boosting* hence boosted decision trees.

In the low mass VBF analyses eight variables are used to train the BDT which are: $\Delta\phi_{\ell\ell}, m_{\ell\ell}, \Delta Y_{jj}, m_{jj}, p_{\mathrm{T}}^{\mathrm{tot}}, m_{\mathrm{T}}$, lepton η centrality and the sum of invariant masses of lepton and jet $\sum_{\ell,j} M_{\ell,j}$.

Generally speaking, the BDT score together with specific cuts are used to define a signal

[7] Also in the high mass 0, 1 and ≥ 2 jet a m_{T} shape fit is performed.

	Signal [125 GeV]	WW	Other VV	top	Z+jets	W+jets	QCD	Total Bkg.	Observed	Data/MC
Z veto (SF)	777.91 ± 1.92	11322.56 ± 14.50	2017.02 ± 13.91	67922.27 ± 30.89	45178.32 ± 95.25	3726.23 ± 30.39	2176.42 ± 6.10	132342.82 ± 106.72	135734	1.03 ± 0.00
$E_{\mathrm{T,[rel],(clj)}}^{\mathrm{miss,(track)}} > [40], (20)$	590.56 ± 1.59	9122.19 ± 13.02	1471.45 ± 12.05	42153.84 ± 24.24	12273.39 ± 49.72	2331.67 ± 19.04	599.99 ± 3.54	67952.53 ± 61.23	69280	1.02 ± 0.00
0j: jet veto	322.62 ± 0.95	7113.27 ± 12.72	738.98 ± 8.47	1227.02 ± 4.05	5682.23 ± 35.33	1334.84 ± 12.62	236.82 ± 2.67	16333.16 ± 40.80	16423	1.01 ± 0.01
0j: $\Delta\phi_{\ell\ell,MET} > 1.57$	322.24 ± 0.95	7108.02 ± 12.71	736.49 ± 8.46	1217.09 ± 4.03	5646.03 ± 35.25	1333.30 ± 12.57	230.25 ± 2.66	16271.18 ± 40.71	16339	1.00 ± 0.01
0j: $p_{\mathrm{T},\ell\ell} > 30$ GeV	272.83 ± 0.84	5690.02 ± 11.38	571.02 ± 7.47	1093.52 ± 3.80	843.05 ± 15.39	1054.32 ± 8.76	27.86 ± 1.83	9279.80 ± 22.73	9339	1.01 ± 0.01
0j: $m_{\ell\ell} < 55$ GeV	232.50 ± 0.65	1670.48 ± 6.14	352.69 ± 6.12	219.78 ± 1.68	377.39 ± 8.83	426.58 ± 6.16	12.39 ± 1.71	3059.31 ± 14.03	3411	1.11 ± 0.02
0j: $E_{\mathrm{T,rel}}^{\mathrm{miss,track}} > 40$ GeV (SF)	232.50 ± 0.65	1670.48 ± 6.14	352.69 ± 6.12	219.78 ± 1.68	377.39 ± 8.83	426.58 ± 6.16	12.39 ± 1.71	3059.31 ± 14.03	3411	1.11 ± 0.02
0j: $\Delta\phi_{\ell\ell} < 1.8$	208.88 ± 0.62	1502.86 ± 5.82	323.74 ± 5.90	207.24 ± 1.62	31.04 ± 2.47	277.63 ± 5.02	9.17 ± 1.63	2351.68 ± 10.26	2642	1.12 ± 0.02
0j: $f_{\mathrm{recoil}} < 0.1$ (SF)	208.88 ± 0.62	1502.86 ± 5.82	323.74 ± 5.90	207.24 ± 1.62	31.04 ± 2.47	277.63 ± 5.02	9.17 ± 1.63	2351.68 ± 10.26	2642	1.12 ± 0.02
1j: one jet	191.83 ± 1.03	2753.00 ± 7.31	495.85 ± 6.51	10725.19 ± 11.99	5729.53 ± 31.66	662.51 ± 12.00	334.25 ± 2.22	20700.33 ± 37.29	20607	1.00 ± 0.01
1j: b-jet veto	164.92 ± 0.89	2406.34 ± 6.79	422.52 ± 6.03	2167.50 ± 5.39	4993.57 ± 29.33	535.26 ± 10.58	268.17 ± 2.00	10793.35 ± 32.98	10859	1.01 ± 0.01
1j: Max lepton-MT (DF)	140.31 ± 0.84	2262.57 ± 6.59	365.58 ± 5.61	2071.60 ± 5.26	2036.76 ± 20.53	476.77 ± 7.17	62.35 ± 0.98	7275.64 ± 24.01	7368	1.01 ± 0.01
1j: $Z \to \tau\tau$ veto (DF)	119.40 ± 0.74	1666.77 ± 5.65	275.27 ± 4.95	1495.74 ± 4.47	713.40 ± 11.90	311.25 ± 5.50	31.70 ± 0.77	4494.13 ± 15.78	4574	1.02 ± 0.02
1j: $m_{\ell\ell} < 55$ GeV	99.98 ± 0.57	486.23 ± 3.04	139.21 ± 3.76	408.30 ± 2.35	389.90 ± 7.93	128.72 ± 4.00	18.61 ± 0.59	1570.99 ± 10.40	1656	1.05 ± 0.03
1j: $E_{\mathrm{T,rel}}^{\mathrm{miss,track}} > 35$ GeV (SF)	99.98 ± 0.57	486.23 ± 3.04	139.21 ± 3.76	408.30 ± 2.35	389.90 ± 7.93	128.72 ± 4.00	18.61 ± 0.59	1570.99 ± 10.40	1656	1.05 ± 0.03
1j: $\Delta\phi_{\ell\ell} < 1.8$	87.18 ± 0.48	417.83 ± 2.82	119.17 ± 3.47	371.75 ± 2.22	27.38 ± 2.16	88.11 ± 2.89	6.06 ± 0.39	1030.30 ± 6.17	1129	1.10 ± 0.03
1j: $f_{recoil} < 0.10$ (SF)	87.18 ± 0.48	417.83 ± 2.82	119.17 ± 3.47	371.75 ± 2.22	27.38 ± 2.16	88.11 ± 2.89	6.06 ± 0.39	1030.30 ± 6.17	1129	1.10 ± 0.03

Table 6.1.: Cutflow for the low mass 8 TeV analysis for the $e\mu + \mu e$ final state. The background and signal estimates are taken from MC, except for the W+jets and QCD backgrounds which are data-driven. Only statistical uncertainties are shown.

	Signal [125 GeV]	WW	Other VV	top	Z+jets	W+jets	QCD	Total Bkg.	Observed	Data/MC
Z veto (SF)	768.22 ± 1.89	9217.31 ± 13.18	2647.03 ± 12.40	54484.93 ± 27.60	1830942.23 ± 1977.40	7870.08 ± 73.28	2193.88 ± 4.70	1907355.46 ± 1979.04	2014469	1.06 ± 0.00
$E_{\mathrm{T,[rel],(clj)}}^{\mathrm{miss,(track)}} > [40], (20)$	288.28 ± 1.10	4075.53 ± 8.78	631.00 ± 6.58	20630.52 ± 16.94	41257.74 ± 258.37	836.07 ± 14.18	45.04 ± 0.72	67475.89 ± 259.55	70655	1.05 ± 0.01
0j: jet veto	171.28 ± 0.65	3256.13 ± 8.68	357.87 ± 5.00	629.43 ± 2.86	31743.64 ± 230.40	503.90 ± 11.14	29.22 ± 0.60	36520.20 ± 230.90	38040	1.04 ± 0.01
0j: $\Delta\phi_{\ell\ell,MET} > 1.57$	171.06 ± 0.65	3252.71 ± 8.68	354.93 ± 4.99	626.46 ± 2.85	29139.54 ± 217.91	492.54 ± 10.79	25.84 ± 0.57	33892.02 ± 218.42	35445	1.05 ± 0.01
0j: $p_{\mathrm{T},\ell\ell} > 30$ GeV	160.72 ± 0.63	3008.84 ± 8.37	308.92 ± 4.70	595.67 ± 2.77	6724.71 ± 98.24	395.98 ± 6.67	2.60 ± 0.29	11036.73 ± 98.97	11660	1.06 ± 0.01
0j: $m_{\ell\ell} < 55$ GeV	146.91 ± 0.56	1256.01 ± 5.40	178.83 ± 3.83	173.20 ± 1.49	4852.12 ± 31.03	250.53 ± 5.27	1.98 ± 0.27	6712.66 ± 32.20	6786	1.01 ± 0.01
0j: $E_{\mathrm{T,rel}}^{\mathrm{miss,track}} > 40$ GeV (SF)	120.98 ± 0.52	1096.73 ± 5.06	106.48 ± 2.75	157.80 ± 1.41	660.73 ± 14.75	133.44 ± 3.34	0.53 ± 0.24	2155.71 ± 16.25	2197	1.02 ± 0.02
0j: $\Delta\phi_{\ell\ell} < 1.8$	117.06 ± 0.51	1067.75 ± 4.99	104.26 ± 2.73	153.41 ± 1.38	649.19 ± 14.67	122.24 ± 3.17	0.46 ± 0.24	2097.31 ± 16.11	2127	1.01 ± 0.02
0j: $f_{\mathrm{recoil}} < 0.1$ (SF)	74.78 ± 0.41	785.89 ± 4.30	69.37 ± 2.20	71.61 ± 0.93	90.71 ± 5.24	78.52 ± 2.46	0.04 ± 0.23	1096.15 ± 7.60	1108	1.01 ± 0.03
1j: one jet	77.22 ± 0.73	1110.81 ± 4.69	191.52 ± 3.54	4770.04 ± 8.00	8379.87 ± 109.38	177.56 ± 6.71	12.77 ± 0.37	14642.59 ± 110.03	15344	1.05 ± 0.01
1j: b-jet veto	66.60 ± 0.64	971.76 ± 4.36	163.24 ± 3.26	970.06 ± 3.64	6885.99 ± 96.99	137.31 ± 5.80	10.23 ± 0.32	9138.59 ± 97.38	9897	1.08 ± 0.02
1j: Max lepton-MT (DF)	66.60 ± 0.64	971.76 ± 4.36	163.24 ± 3.26	970.06 ± 3.64	7463.42 ± 105.41	137.31 ± 5.80	10.23 ± 0.32	9716.02 ± 105.77	9897	1.02 ± 0.02
1j: $Z \to \tau\tau$ veto (DF)	66.60 ± 0.64	971.76 ± 4.36	163.24 ± 3.26	970.06 ± 3.64	7463.42 ± 105.41	137.31 ± 5.80	10.23 ± 0.32	9716.02 ± 105.77	9897	1.02 ± 0.02
1j: $m_{\ell\ell} < 55$ GeV	57.95 ± 0.50	351.07 ± 2.62	78.77 ± 2.40	310.99 ± 2.09	3587.77 ± 21.92	73.22 ± 4.32	7.79 ± 0.28	4409.61 ± 22.72	5127	1.16 ± 0.02
1j: $E_{\mathrm{T,rel}}^{\mathrm{miss,track}} > 35$ GeV (SF)	42.64 ± 0.43	292.32 ± 2.39	49.20 ± 1.82	266.12 ± 1.89	196.08 ± 7.97	37.58 ± 1.98	0.20 ± 0.05	841.51 ± 8.95	960	1.14 ± 0.04
1j: $\Delta\phi_{\ell\ell} < 1.8$	38.59 ± 0.41	265.11 ± 2.28	44.41 ± 1.74	247.40 ± 1.81	195.57 ± 8.34	30.34 ± 1.77	0.17 ± 0.05	783.00 ± 9.18	889	1.14 ± 0.04
1j: $f_{recoil} < 0.10$ (SF)	23.17 ± 0.28	187.95 ± 1.93	29.47 ± 1.42	141.98 ± 1.36	27.30 ± 2.98	17.43 ± 1.31	0.02 ± 0.03	404.16 ± 4.27	467	1.16 ± 0.05

Table 6.2.: Cutflow for the low mass 8 TeV analysis for the $ee + \mu\mu$ final state. The background and signal estimates are taken from MC, except for the W+jets and QCD backgrounds which are data-driven. Only statistical uncertainties are shown.

region and control regions for the dominant background in the $N_{\text{jets}} \geq 2$ category. To obtain limits and measure couplings a binned likelihood fit is performed on the BDT score which is binned in 3 bins in the signal region.

6.4.2. Event selection for $m_H > 200\,\text{GeV}$

The high mass analysis is designed to search for spin-0, neutral Higgs-like bosons in the mass range $200\,\text{GeV} \leq m_\text{H} \leq 1\,\text{TeV}$ (2 TeV for the NWA scenario). It uses a cut-based approach to define signal and control regions and a binned likelihood fit of the transverse mass m_T to obtain limits. Defining a (cut-based) analysis for a search over a broad phase space is more involved than defining a signal region for a more or less known signal. The high mass analysis was optimized via maximizing the significance $S/\sqrt{B + \Delta B^2}$ where S are the signal events for various mass hypothesis, B is the number of events from the Standard Model backgrounds including the processes (ggF,VBF) $\rightarrow H \rightarrow WW^{(*)} \rightarrow \ell\nu\ell\nu$ for a 125 GeV Higgs boson and ΔB^2 is the systematic uncertainty on the yield of background events. The uncertainty was fixed to 10 % during the optimization process. The 10 % are based on the experience from earlier publications of the low and high mass analysis [72], [73]. Furthermore, a 20 % uncertainty on the background was implemented in the optimization process and it could be shown that the results of the cut optimization were approximately stable under the change of the background uncertainty. The analysis has been optimized for each jet category (0,1,$\geq$ 2) and for both same flavor and different flavor events.
In order to utilize possible correlations between kinematic variables a multi-dimensional optimization tool *BumpHunter* was used. *BumpHunter* is a software package from the *StatPatterRecognition* package [74] and makes use of the PRIM [75] algorithm. The *BumpHunter* tool searches for multi-dimensional rectangular regions with optimal separation between two categories of events. A list of 16 variables was used to optimize the signal region selection. Table 6.3 summarizes the variables used in the three different jet categories. The choices of variables used in the optimization were based on the experiences of the low and high mass analysis and from shape comparison studies [76].
The optimization was performed with respect to the SM-like Higgs signal only, since it could be shown that the significance based optimization does not significantly depend on the various signal models (SM-like, NWA or EWS).

The *BumpHunter* tool returns a selection of each variable with an upper and lower boundary. Very often one of the two cut limits yielded very high or very low values so that only one dimensional cuts are used. The cuts resulting from the *BumpHunter* optimization were further fine-tuned while mainly two considerations were playing an important role:

- MC Statistics - especially for very heavy Higgs Bosons ($m_\text{H} > 700\,\text{GeV}$) a pure significance optimization can result in signal regions with very poor statistics.

- Signal vs. background shape - for some variables the shape of background and signal is rather similar. A significance optimization on such variables can yield very hard cuts leading again to very poor statistics in signal regions.

Table 6.3.: This Table shows a complete list of variables which have been used with *BumpHunter* to search for signal regions as well as control regions. The 'x' indicates if a variable was used for a given jet multiplicity [63].

Variable	0-jet	1-jet	≥ 2 jets
Lepton $p_{\mathrm{T}}^{\mathrm{lead}}$	x	x	x
Lepton $p_{\mathrm{T}}^{\mathrm{sublead}}$	x	x	x
Calorimeter $\not{E}_{\mathrm{T}}^{\mathrm{miss}}$			x
Calorimeter relative $\not{E}_{\mathrm{T}}^{\mathrm{miss}}$	x	x	
Track $\not{E}_{\mathrm{T}}^{\mathrm{miss}}$	x	x	x
Track relative $\not{E}_{\mathrm{T}}^{\mathrm{miss}}$	x	x	x
Jet corrected track $\not{E}_{\mathrm{T}}^{\mathrm{miss}}$	x	x	x
$p_T^{\ell\ell}$	x		
$p_{\mathrm{T}}^{\mathrm{tot}}$			x
$m_{\ell\ell}$	x	x	x
m_{jj}			x
ΔY_{jj}			x
Jet $p_{\mathrm{T}}^{\mathrm{lead}}$			x
$\Delta\eta_{jj}$			x
$\Delta\Phi_{\ell\ell}$	x	x	x
$\Delta\eta_{\ell\ell}$	x	x	x

The outcome of the optimization will be presented and discussed in the following. The same cuts are used for all three analyzed scenarios (SM-like, NWA & EWS). In order to keep the presented information readable only the SM-like signal is shown in the following plots. The background composition is independent of the analyzed scenario, only signal event yields and the shape of the signal differs.

Selection for N_{jets}= 0
Similar to the low-mass analysis the main backgrounds in the 0 jet case are WW and Z+jets. The following cuts were found to be optimal to separate signal (ggF + VBF) from background in the 0 jet category:

- $p_{\mathrm{T}}^{\mathrm{lead}} > 60\,\mathrm{GeV}$ and $p_{\mathrm{T}}^{\mathrm{sublead}} > 30\,\mathrm{GeV}$.
- $p_{\mathrm{T}}^{\mathrm{miss}} > 45\,\mathrm{GeV}$ for different flavor events and $E_{\mathrm{T,rel}}^{\mathrm{miss}} > 45\,\mathrm{GeV}$ with an additional cut on $p_{\mathrm{T,rel}}^{\mathrm{miss}} > 65\,\mathrm{GeV}$ for same flavor events.
- $p_{\mathrm{T}}^{\ell\ell} > 60\,\mathrm{GeV}$ which rejects Z+jets very efficiently.
- The di-lepton mass should be $m_{\ell\ell} > 60\,\mathrm{GeV}$.

- The difference in pseudo-rapidity of the two leptons in the final state should be $\Delta\eta_{\ell\ell} < 1.35$. This cut is necessary to orthogonalize the WW control region to the signal region.

In Figure 6.14 the m_{T} distribution in the high mass 0 jet signal region is shown. The dominant background is WW with 56 % contribution for $e\mu + \mu e$ and 53 % for $ee + \mu\mu$. The second most dominant background is top with 37 % in $e\mu + \mu e$ and 38 % in $ee + \mu\mu$. The total background expectation is 512.5 ± 3.5 (stat.) events for different flavor and 186.8 ± 2.3 (stat.) for same flavor.

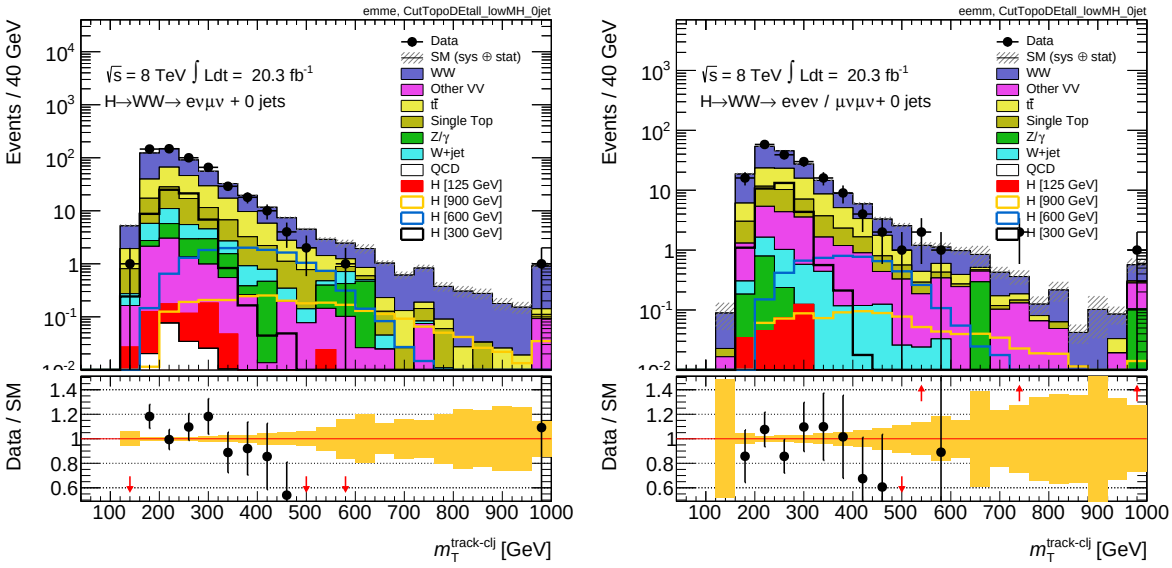

(a) different flavor 0 jet signal region

(b) same flavor 0 jet signal region

Figure 6.14.: The distributions show the transverse mass m_{T} in the 0 jet signal region for same flavor (left) and different flavor (right). All normalization factors which are obtained from the control regions are applied (see chapter 7)

Selection for $N_{\mathrm{jets}} = 1$

In the 1 jet case the following cuts are used to define the high mass signal region:

- $p_{\mathrm{T}}^{\mathrm{lead}} > 50\,\mathrm{GeV}$ and $p_{\mathrm{T}}^{\mathrm{sublead}} > 35\,\mathrm{GeV}$.

- To reduce top background no jet which was tagged as a b-jet (see section 5.3) with a transverse momentum of $p_{\mathrm{T}} > 20\,\mathrm{GeV}$ should be in the event.

- $p_{\mathrm{T}}^{\mathrm{miss}} > 35\,\mathrm{GeV}$ for different flavor events and $E_{\mathrm{T,rel}}^{\mathrm{miss}} > 45\,\mathrm{GeV}$ with an additional cut on $p_{\mathrm{T,rel}}^{\mathrm{miss}} > 70\,\mathrm{GeV}$ for same flavor events.

- The di-lepton mass should be $m_{\ell\ell} > 65\,\text{GeV}$.

- The difference in pseudo-rapidity of the two leptons in the final state should be like in the 0 jet bin $\Delta\eta_{\ell\ell} < 1.35$. Also in the 1 jet case this cut is a necessity to orthogonalize signal and WW control region.

Figure 6.15 shows the m_{T} distributions for the 1 jet high mass signal region. The dominant backgrounds in the 1 jet signal region are like in the 0 jet case WW and top but in the 1 jet case top contributes more to the total background as WW. 49 % of events originate from top in the different flavor case and about 55 % arising from top in the same flavor case. About 42 % are WW background in the different flavor case and 35 % in the same flavor case. The total background expectation is 940 ± 6 (stat.) for $e\mu + \mu e$ and 86.9 ± 1.4 (stat.) for $ee + \mu\mu$.

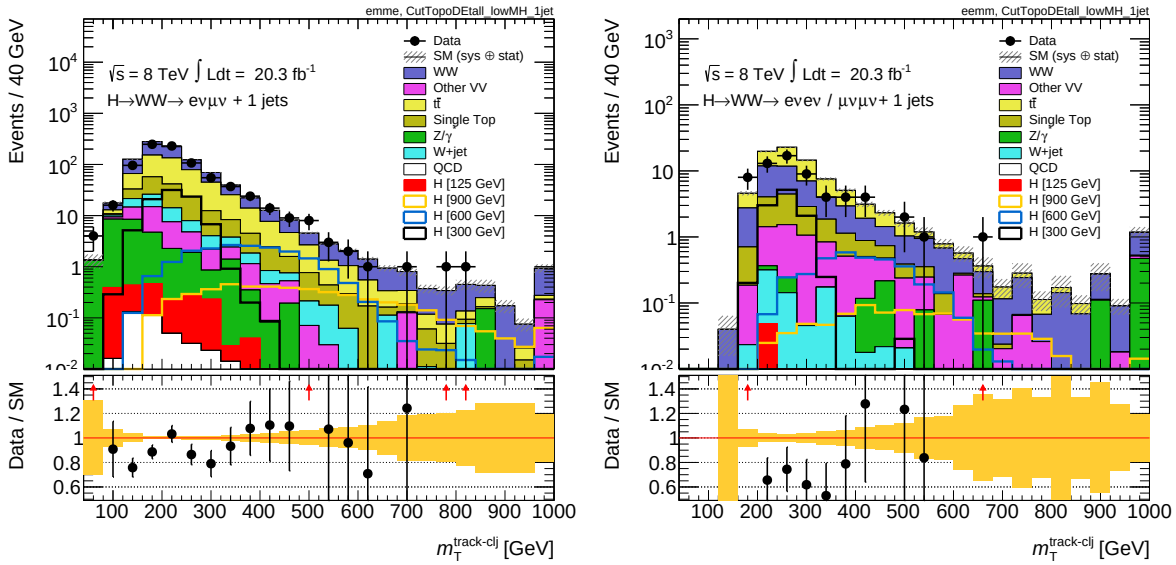

(a) different flavor 1 jet signal region

(b) same flavor 1 jet signal region

Figure 6.15.: The distributions show the transverse mass m_{T} in the 1 jet signal region for same flavor (left) and different flavor (right). All normalization factors which are obtained from the control regions are applied (see chapter 7).

Selection for $N_{\text{jets}} \geq 2$

For the high mass VBF category a cut-based approach is applied. This category is very interesting in the search for high mass Higgs bosons due to the very clear signature of two oppositely charged leptons, large $\not{E}_{\text{T}}^{\text{miss}}$ and two hard forward jets. The cuts used for $N_{\text{jets}} \geq 2$ are:

- $p_{\text{T}}^{\text{lead}} > 45\,\text{GeV}$ and $p_{\text{T}}^{\text{sublead}} > 20\,\text{GeV}$.

- To reduce top background, no jet which was tagged as a b-jet (see section 5.3) with a transverse momentum of $p_{\mathrm{T}} > 20\,\mathrm{GeV}$ should be in the event.

- $\not{E}_{\mathrm{T}}^{\mathrm{miss}} > 25\,\mathrm{GeV}$ for different flavor events and $\not{E}_{\mathrm{T}}^{\mathrm{miss}} > 45\,\mathrm{GeV}$ for same flavor events.

- The total transverse momentum of leptons, jets and missing transverse energy $p_{\mathrm{T}}^{\mathrm{tot}}$ should be smaller than 40 GeV. This is required in order to reject all sorts of background events with roughly 68 % efficiency while only about 20 % of signal independent of mass is getting rejected.

- The rapidity gap of the two jets in the event Y_{jj} should be greater than 4. This cut is based on the event topology origination from the VBF production mode.

- The di-jet mass m_{jj} is required to be greater than 500 GeV.

- Owing to the fact that it is expected to have two hard forward jets from the vector boson fusion, it is required to not have any jet with a $p_{\mathrm{T}} > 20\,\mathrm{GeV}$ within the rapidity gap of the two leading jets, the so called central jet veto CJV.

- The two leptons of the final state are required to be within the rapidity gap of the two hard forward jets. This requirement will be referred to as the outside lepton veto OLV.

- The di-lepton mass should be $m_{\ell\ell} > 45\,\mathrm{GeV}$ for $ee + \mu\mu$ events and $m_{\ell\ell} > 60\,\mathrm{GeV}$ for $e\mu + \mu e$ events is required.

- The difference in pseudo-rapidity of the two leptons in the final state should be $\Delta\eta_{\ell\ell} < 1.85$ which helps rejecting WW and top background in the signal region.

The transverse mass distributions in the 2 jet high mass signal region are shown in Figure 6.16. In the 2 jet different flavor case top is with 44 % the dominant background followed by WW with 34 %. For the same flavor 2 jet signal region the dominant background is Z+jets with 51 % followed by top with 24 %. The total background expectation is 23.8 ± 0.7 (stat.) for $e\mu + \mu e$ and 29.7 ± 2.3 (stat.) for $ee + \mu\mu$.

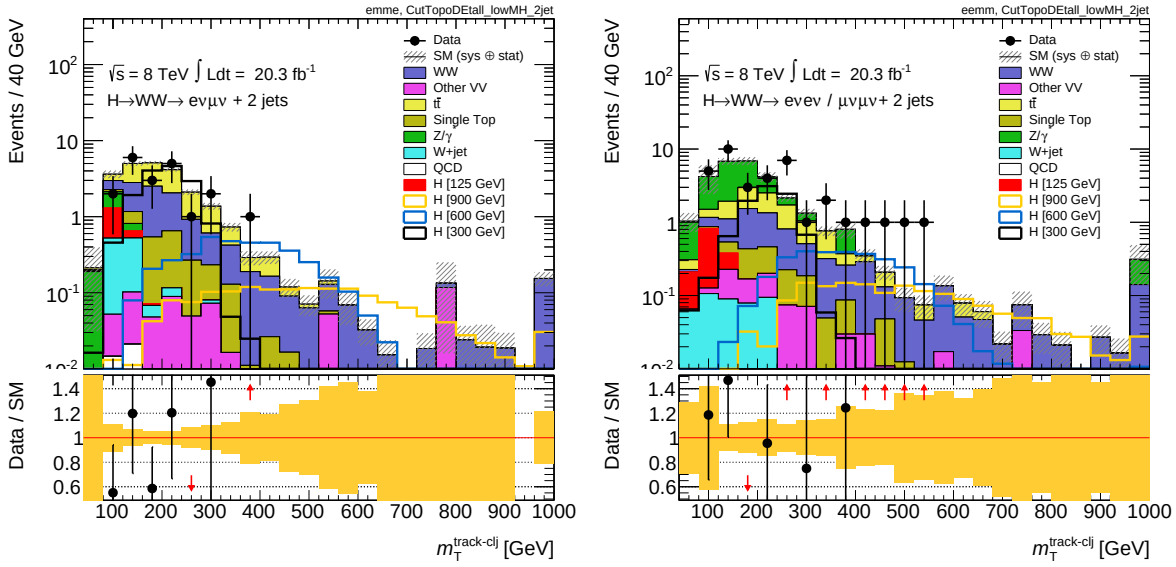

(a) different flavor 2 jet signal region

(b) same flavor 2 jet signal region

Figure 6.16.: The distributions show the transverse mass m_{T} in the 2 jet signal region for same flavor (left) and different flavor (right). All normalization factors which are obtained from the control regions are applied (see chapter 7).

In Table 6.4 and 6.5 the detailed cutflow tables for the high mass analysis are shown separately for $e\mu + \mu e$ and $ee + \mu\mu$. The numbers for the signal of a 300 GeV, 600 GeV and 900 GeV Higgs-Boson are for the SM-like case. For other models (NWA & EWS) the yields differ. The same signal region definitions are used for all three analyzed scenarios.

	Signal [300 GeV]	Signal [600 GeV]	Signal [900 GeV]	125 GeV BG	WW	Other VV	top	Z+jets	W+jets	QCD	Total Bkg.	Observed	Data/MC
Z veto (for $ee, \mu\mu$)	803.97 ± 4.06	131.15 ± 0.84	29.45 ± 0.29	794.24 ± 1.93	11227.36 ± 14.38	2017.02 ± 13.91	64315.32 ± 29.25	45276.83 ± 95.89	4099.47 ± 30.19	2176.42 ± 6.10	129906.66 ± 106.78	135734	1.04 ± 0.00
0j:$p_{TLead} > 60$ GeV	603.03 ± 3.52	122.03 ± 0.74	27.83 ± 0.26	106.43 ± 1.07	4493.75 ± 9.61	480.91 ± 6.53	35215.19 ± 21.57	1234.45 ± 17.49	891.84 ± 9.11	27.14 ± 0.28	42449.71 ± 31.46	43003	1.01 ± 0.00
0j: $p_{TSubLead} > 30$ GeV	483.45 ± 3.16	110.30 ± 0.69	25.60 ± 0.25	45.88 ± 0.82	3423.23 ± 8.40	307.73 ± 5.18	24784.53 ± 18.13	422.88 ± 10.73	408.16 ± 4.63	13.98 ± 0.13	29406.38 ± 23.74	29534	1.00 ± 0.01
0j: $E^{\mathrm{miss}}_{\mathrm{T,rel}} > 45$ GeV	330.51 ± 2.60	87.35 ± 0.60	21.36 ± 0.22	22.48 ± 0.58	1737.91 ± 5.95	132.09 ± 3.35	17048.49 ± 15.04	161.43 ± 5.25	164.75 ± 3.35	2.71 ± 0.07	19269.85 ± 17.67	19237	1.00 ± 0.01
0j: jet veto	112.15 ± 1.58	23.60 ± 0.32	4.31 ± 0.10	1.28 ± 0.21	788.88 ± 4.04	28.81 ± 1.56	372.37 ± 2.17	20.17 ± 2.35	43.28 ± 1.18	0.75 ± 0.04	1255.55 ± 5.51	1230	0.98 ± 0.03
0j: $p_{T,\ell\ell} > 60$ GeV	78.08 ± 1.32	18.51 ± 0.27	3.57 ± 0.09	0.95 ± 0.17	448.96 ± 3.04	16.86 ± 1.13	273.13 ± 1.86	11.06 ± 1.73	20.22 ± 0.88	0.33 ± 0.02	771.52 ± 4.22	785	1.02 ± 0.04
0j: $m_{\ell\ell} > 60$ GeV	77.64 ± 1.32	18.51 ± 0.27	3.56 ± 0.09	0.56 ± 0.15	440.81 ± 3.01	16.08 ± 1.10	265.85 ± 1.84	10.73 ± 1.71	20.14 ± 0.88	0.33 ± 0.02	754.49 ± 4.17	769	1.02 ± 0.04
0j: $E^{\mathrm{miss,track}}_{\mathrm{T,rel}} > 65$ GeV	77.64 ± 1.32	18.51 ± 0.27	3.56 ± 0.09	0.56 ± 0.15	440.81 ± 3.01	16.08 ± 1.10	265.85 ± 1.84	10.73 ± 1.71	20.14 ± 0.88	0.33 ± 0.02	754.49 ± 4.17	769	1.02 ± 0.04
0j: $\Delta\eta_{\ell\ell} < 1.35$	63.15 ± 1.19	13.76 ± 0.24	2.56 ± 0.08	0.53 ± 0.15	286.84 ± 2.43	8.51 ± 0.80	191.69 ± 1.56	9.48 ± 1.62	15.21 ± 0.75	0.19 ± 0.02	512.45 ± 3.49	526	1.03 ± 0.05
1j:$p_{TLead} > 55$ GeV	647.26 ± 3.64	123.91 ± 0.75	28.24 ± 0.27	142.07 ± 1.18	5481.82 ± 10.71	573.40 ± 7.10	41986.88 ± 24.21	1724.91 ± 20.71	1102.60 ± 10.21	42.34 ± 0.80	51054.01 ± 35.86	49563	0.97 ± 0.00
1j: $p_{TSubLead} > 35$ GeV	463.16 ± 3.09	106.91 ± 0.68	24.96 ± 0.24	42.81 ± 0.82	3596.56 ± 8.68	298.47 ± 5.07	24840.45 ± 18.66	401.06 ± 9.64	377.19 ± 4.31	12.94 ± 0.11	29569.47 ± 23.69	28333	0.96 ± 0.01
1j: $E^{\mathrm{miss}}_{\mathrm{T,rel}} > 45, 35$ GeV	363.65 ± 2.73	92.37 ± 0.63	22.29 ± 0.23	27.00 ± 0.66	2209.22 ± 6.78	164.97 ± 3.72	19659.76 ± 16.60	192.60 ± 6.88	214.96 ± 3.46	3.21 ± 0.06	22471.72 ± 19.88	21338	0.95 ± 0.01
1j: 1 jet	126.27 ± 1.61	31.51 ± 0.36	7.86 ± 0.13	8.08 ± 0.40	715.99 ± 3.87	62.45 ± 2.24	3313.36 ± 6.63	63.98 ± 4.69	61.19 ± 1.62	1.08 ± 0.04	4226.14 ± 9.41	4029	0.95 ± 0.02
1j: b veto	110.55 ± 1.49	27.28 ± 0.33	6.92 ± 0.12	6.60 ± 0.35	622.35 ± 3.58	51.44 ± 2.04	677.60 ± 2.95	54.01 ± 4.54	49.64 ± 1.27	0.78 ± 0.04	1462.41 ± 6.93	1364	0.93 ± 0.03
1j: $m_{\ell\ell} > 65$ GeV	109.72 ± 1.49	27.19 ± 0.32	6.92 ± 0.12	1.91 ± 0.29	585.63 ± 3.47	48.42 ± 1.98	645.61 ± 2.88	31.84 ± 4.22	48.26 ± 1.23	0.75 ± 0.04	1362.43 ± 6.61	1269	0.93 ± 0.03
1j: $E^{\mathrm{miss,track}}_{\mathrm{T,rel}} > 70$ GeV	109.72 ± 1.49	27.19 ± 0.32	6.92 ± 0.12	1.91 ± 0.29	585.63 ± 3.47	48.42 ± 1.98	645.61 ± 2.88	31.84 ± 4.22	48.26 ± 1.23	0.75 ± 0.04	1362.43 ± 6.61	1269	0.93 ± 0.03
1j: $\Delta\eta_{\ell\ell} < 1.35$	89.62 ± 1.35	19.20 ± 0.27	4.73 ± 0.10	1.74 ± 0.27	390.17 ± 2.84	29.71 ± 1.60	456.08 ± 2.42	28.12 ± 4.16	33.65 ± 1.04	0.39 ± 0.03	939.86 ± 5.91	857	0.91 ± 0.03
2j:$p_{TLead} > 45$ GeV	723.73 ± 3.85	127.58 ± 0.80	28.81 ± 0.28	270.83 ± 1.41	6860.10 ± 11.23	834.63 ± 8.57	49685.17 ± 25.76	4133.38 ± 31.46	1715.04 ± 12.91	99.97 ± 1.15	63599.11 ± 44.98	65724	1.03 ± 0.00
2j: $p_{TSubLead} > 20$ GeV	666.76 ± 3.70	122.34 ± 0.77	27.85 ± 0.27	172.99 ± 1.20	6128.32 ± 10.63	647.95 ± 7.49	43462.80 ± 24.13	2319.54 ± 24.47	982.25 ± 8.50	57.32 ± 0.54	53771.17 ± 37.73	55589	1.03 ± 0.00
2j: $E^{\mathrm{miss}}_{\mathrm{T,rel}} > 45, 25$ GeV	600.69 ± 3.51	114.00 ± 0.75	26.19 ± 0.26	135.33 ± 1.11	4996.06 ± 9.57	490.33 ± 6.48	38900.73 ± 22.82	1349.37 ± 17.47	718.86 ± 7.35	29.85 ± 0.38	46620.54 ± 31.86	48036	1.03 ± 0.00
2j: >= 2 jets	177.97 ± 1.81	42.97 ± 0.45	11.39 ± 0.17	58.87 ± 0.71	694.08 ± 3.49	161.77 ± 3.85	31602.54 ± 20.72	440.29 ± 8.74	262.82 ± 5.35	7.67 ± 0.18	33228.03 ± 23.71	34207	1.03 ± 0.01
2j: b veto	131.11 ± 1.52	31.71 ± 0.39	8.51 ± 0.14	41.81 ± 0.56	511.39 ± 2.97	112.18 ± 3.16	1976.61 ± 5.05	311.05 ± 7.20	96.29 ± 2.60	3.89 ± 0.14	3053.23 ± 10.16	3255	1.07 ± 0.02
2j: $p_{T,\mathrm{tot}} < 40$ GeV	104.16 ± 1.35	25.13 ± 0.35	6.93 ± 0.14	33.27 ± 0.49	424.07 ± 2.72	83.11 ± 2.74	1512.16 ± 4.42	257.63 ± 6.61	53.39 ± 2.05	2.09 ± 0.11	2365.72 ± 9.09	2589	1.09 ± 0.02
2j: $\Delta Y_{\mathrm{jj}} > 4.0$	27.32 ± 0.55	7.01 ± 0.17	2.84 ± 0.09	6.26 ± 0.12	29.28 ± 0.66	3.70 ± 0.49	84.48 ± 1.05	8.89 ± 1.08	3.22 ± 0.50	0.20 ± 0.03	136.02 ± 1.80	133	0.98 ± 0.09
2j: $m_{\mathrm{jj}} > 500$ GeV	22.59 ± 0.47	6.07 ± 0.16	2.61 ± 0.09	5.23 ± 0.09	19.47 ± 0.52	2.08 ± 0.36	53.64 ± 0.84	6.43 ± 0.89	1.94 ± 0.41	0.12 ± 0.03	88.92 ± 1.44	89	1.00 ± 0.11
2j: CJV (20 GeV)	17.61 ± 0.40	4.69 ± 0.14	2.00 ± 0.07	3.98 ± 0.08	14.04 ± 0.43	1.09 ± 0.22	21.33 ± 0.53	3.36 ± 0.60	1.34 ± 0.33	0.06 ± 0.02	45.22 ± 1.00	39	0.86 ± 0.14
2j: OLV	16.82 ± 0.38	4.53 ± 0.14	1.94 ± 0.07	3.84 ± 0.08	11.36 ± 0.38	0.82 ± 0.20	18.06 ± 0.48	2.50 ± 0.52	1.25 ± 0.33	0.05 ± 0.01	37.88 ± 0.90	35	0.92 ± 0.16
2j: $m_{\ell\ell} > 45, 60$ GeV	16.22 ± 0.38	4.53 ± 0.14	1.94 ± 0.07	0.95 ± 0.04	9.85 ± 0.35	0.74 ± 0.19	16.10 ± 0.46	1.17 ± 0.38	1.02 ± 0.30	0.05 ± 0.01	29.89 ± 0.78	27	0.90 ± 0.18
2j: $\Delta\eta_{\ell\ell} < 1.85$	14.91 ± 0.36	3.79 ± 0.14	1.53 ± 0.06	0.95 ± 0.04	7.96 ± 0.32	0.56 ± 0.17	12.18 ± 0.40	1.17 ± 0.38	0.89 ± 0.30	0.04 ± 0.01	23.75 ± 0.73	20	0.84 ± 0.19

Table 6.4.: Cutflow for the high mass 8 TeV analysis for the $e\mu + \mu e$ final state. The background and signal estimates are taken from MC, except for the W+jets and QCD backgrounds which are data-driven. Only statistical uncertainties are shown.

	Signal [300 GeV]	Signal [600 GeV]	Signal [900 GeV]	125 GeV BG	WW	Other VV	top	Z+jets	W+jets	QCD	Total Bkg.	Observed	Data/MC
Z veto (for $ee, \mu\mu$)	641.58 ± 3.63	122.53 ± 0.76	27.96 ± 0.32	792.08 ± 1.90	9120.80 ± 17.04	2647.03 ± 12.40	51591.56 ± 26.14	1833332.07 ± 1550.27	9560.04 ± 72.81	2193.88 ± 4.70	1909237.47 ± 1552.35	2014469	1.06 ± 0.00
0j:$p_{TLead} > 60$ GeV	500.27 ± 3.21	115.57 ± 0.69	26.91 ± 0.30	97.35 ± 1.01	3757.30 ± 11.83	618.79 ± 6.27	28250.74 ± 19.28	249521.90 ± 397.28	1008.72 ± 19.75	19.48 ± 0.45	283274.29 ± 398.46	292132	1.03 ± 0.00
0j: $p_{TSubLead} > 30$ GeV	423.45 ± 2.96	106.39 ± 0.66	24.99 ± 0.24	41.61 ± 0.84	2993.46 ± 10.69	417.48 ± 5.14	20681.28 ± 16.53	197231.15 ± 274.83	573.77 ± 11.37	6.49 ± 0.28	221945.25 ± 275.82	228523	1.03 ± 0.00
0j: $E^{\mathrm{miss}}_{\mathrm{T,rel}} > 45$ GeV	179.48 ± 1.93	46.75 ± 0.45	11.09 ± 0.16	8.43 ± 0.47	958.54 ± 6.01	109.63 ± 2.45	6293.65 ± 9.10	2462.08 ± 29.99	62.01 ± 2.46	0.07 ± 0.04	9894.41 ± 32.10	9674	0.98 ± 0.01
0j: jet veto	75.21 ± 1.30	14.11 ± 0.24	2.58 ± 0.09	0.96 ± 0.20	524.52 ± 4.48	46.37 ± 1.50	227.24 ± 1.70	1650.96 ± 21.91	27.91 ± 1.65	0.06 ± 0.02	2478.02 ± 22.54	2391	0.96 ± 0.02
0j: $p_{T,\ell\ell} > 60$ GeV	51.91 ± 1.08	11.46 ± 0.21	2.18 ± 0.08	0.63 ± 0.12	275.56 ± 3.21	32.75 ± 1.22	161.75 ± 1.43	35.46 ± 3.68	8.38 ± 0.48	0.02 ± 0.01	514.55 ± 5.25	517	1.00 ± 0.05
0j: $m_{\ell\ell} > 60$ GeV	51.46 ± 1.08	11.46 ± 0.21	2.18 ± 0.08	0.32 ± 0.10	267.64 ± 3.17	29.21 ± 1.15	155.29 ± 1.40	34.59 ± 3.66	8.35 ± 0.47	0.01 ± 0.01	495.41 ± 5.19	498	1.01 ± 0.05
0j: $E^{\mathrm{miss,track}}_{\mathrm{T,rel}} > 65$ GeV	37.29 ± 0.92	7.47 ± 0.17	1.37 ± 0.07	0.28 ± 0.10	167.74 ± 2.51	21.75 ± 0.97	102.67 ± 1.14	2.44 ± 0.74	4.33 ± 0.31	0.00 ± 0.00	299.21 ± 3.03	278	0.93 ± 0.06
0j: $\Delta\eta_{\ell\ell} < 1.35$	30.11 ± 0.83	5.13 ± 0.14	0.95 ± 0.06	0.28 ± 0.10	95.70 ± 1.89	16.13 ± 0.81	70.16 ± 0.94	1.46 ± 0.50	3.11 ± 0.26	0.00 ± 0.00	186.83 ± 2.33	181	0.97 ± 0.07
1j:$p_{TLead} > 55$ GeV	529.50 ± 3.30	117.13 ± 0.70	27.08 ± 0.31	130.84 ± 1.13	4450.54 ± 12.95	719.72 ± 6.70	33185.36 ± 21.48	327301.55 ± 467.08	1272.02 ± 22.73	31.28 ± 0.55	367091.30 ± 468.36	377606	1.03 ± 0.00
1j: $p_{TSubLead} > 35$ GeV	410.89 ± 2.92	103.48 ± 0.65	24.35 ± 0.24	38.52 ± 0.83	3124.79 ± 11.03	409.32 ± 5.09	20847.23 ± 17.05	241505.23 ± 296.14	591.52 ± 11.70	7.49 ± 0.28	266524.10 ± 297.11	273310	1.03 ± 0.00
1j: $E^{\mathrm{miss}}_{\mathrm{T,rel}} > 45, 35$ GeV	172.00 ± 1.89	45.04 ± 0.44	10.73 ± 0.16	7.73 ± 0.45	959.42 ± 6.07	105.34 ± 2.42	6262.85 ± 9.33	3062.06 ± 33.63	63.20 ± 2.09	0.11 ± 0.04	10460.71 ± 35.57	9856	0.94 ± 0.01
1j: 1 jet	58.27 ± 1.10	15.71 ± 0.27	3.80 ± 0.09	3.00 ± 0.36	287.08 ± 3.33	35.09 ± 1.37	1417.45 ± 4.34	618.69 ± 14.92	16.90 ± 1.19	0.03 ± 0.03	2378.25 ± 15.99	2153	0.91 ± 0.02
1j: b veto	50.72 ± 1.02	13.67 ± 0.25	3.35 ± 0.09	2.33 ± 0.29	248.08 ± 3.07	28.66 ± 1.21	291.89 ± 1.93	523.38 ± 11.52	14.80 ± 0.87	0.01 ± 0.02	1109.15 ± 12.17	989	0.89 ± 0.03
1j: $m_{\ell\ell} > 65$ GeV	50.29 ± 1.01	13.66 ± 0.25	3.35 ± 0.09	0.76 ± 0.26	229.19 ± 2.95	25.57 ± 1.14	274.76 ± 1.88	478.31 ± 10.62	14.40 ± 0.86	0.02 ± 0.02	1022.99 ± 11.27	912	0.89 ± 0.03
1j: $E^{\mathrm{miss,track}}_{\mathrm{T,rel}} > 70$ GeV	13.04 ± 0.52	4.58 ± 0.13	1.15 ± 0.05	0.05 ± 0.03	46.53 ± 1.26	8.94 ± 0.65	70.93 ± 0.95	1.20 ± 0.33	1.34 ± 0.19	-0.00 ± 0.00	128.99 ± 1.75	99	0.77 ± 0.08
1j: $\Delta\eta_{\ell\ell} < 1.35$	10.77 ± 0.47	3.39 ± 0.11	0.84 ± 0.05	0.05 ± 0.03	30.54 ± 1.03	6.18 ± 0.50	48.10 ± 0.78	1.20 ± 0.33	0.80 ± 0.15	-0.00 ± 0.00	86.87 ± 1.44	63	0.73 ± 0.09
2j:$p_{TLead} > 45$ GeV	576.32 ± 3.44	119.72 ± 0.73	27.56 ± 0.32	251.77 ± 1.34	5251.22 ± 13.09	1023.42 ± 7.90	38618.59 ± 22.65	500088.55 ± 665.83	2054.69 ± 32.53	78.21 ± 0.85	547366.47 ± 667.19	568693	1.04 ± 0.00
2j: $p_{TSubLead} > 20$ GeV	533.83 ± 3.32	116.20 ± 0.71	26.76 ± 0.30	155.44 ± 1.15	4640.75 ± 12.40	795.39 ± 6.91	33624.65 ± 21.17	428685.92 ± 588.67	1162.07 ± 23.05	34.23 ± 0.56	469098.45 ± 589.68	484917	1.03 ± 0.00
2j: $E^{\mathrm{miss}}_{\mathrm{T,rel}} > 45, 25$ GeV	371.12 ± 2.75	92.71 ± 0.63	22.40 ± 0.27	75.14 ± 0.87	2540.51 ± 9.06	357.59 ± 4.62	23526.18 ± 17.71	24393.14 ± 138.11	323.84 ± 7.35	4.48 ± 0.19	51220.89 ± 139.81	50828	0.99 ± 0.01
2j: >= 2 jets	116.23 ± 1.47	35.52 ± 0.37	10.07 ± 0.16	36.82 ± 0.58	416.86 ± 3.58	117.04 ± 2.87	19151.63 ± 16.10	5147.06 ± 68.41	136.24 ± 4.96	1.79 ± 0.14	25007.43 ± 70.60	25240	1.01 ± 0.01
2j: b veto	86.86 ± 1.24	25.94 ± 0.31	7.78 ± 0.14	25.73 ± 0.45	303.32 ± 3.03	79.40 ± 2.36	1209.56 ± 3.93	3553.25 ± 55.05	41.64 ± 3.19	0.93 ± 0.11	5213.83 ± 55.42	5175	0.99 ± 0.02
2j: $p_{T,\mathrm{tot}} < 40$ GeV	68.40 ± 1.10	20.48 ± 0.27	6.30 ± 0.13	20.29 ± 0.40	249.43 ± 2.76	59.20 ± 2.09	921.37 ± 3.43	2021.44 ± 43.88	21.52 ± 2.61	0.32 ± 0.08	3293.57 ± 44.23	3314	1.01 ± 0.02
2j: $\Delta Y_{\mathrm{jj}} > 4.0$	17.60 ± 0.44	5.77 ± 0.14	2.69 ± 0.08	3.68 ± 0.08	17.85 ± 0.65	2.89 ± 0.45	52.14 ± 0.82	105.29 ± 10.38	1.20 ± 0.60	0.05 ± 0.02	183.10 ± 10.46	195	1.07 ± 0.10
2j: $m_{\mathrm{jj}} > 500$ GeV	14.70 ± 0.38	4.99 ± 0.13	2.49 ± 0.08	3.28 ± 0.07	12.78 ± 0.52	2.17 ± 0.41	34.29 ± 0.66	66.59 ± 8.94	0.63 ± 0.29	0.04 ± 0.02	119.77 ± 8.99	124	1.04 ± 0.12
2j: CJV (20 GeV)	11.01 ± 0.31	3.79 ± 0.11	2.07 ± 0.08	2.50 ± 0.06	8.93 ± 0.41	1.21 ± 0.26	13.19 ± 0.41	34.52 ± 5.83	0.36 ± 0.22	0.02 ± 0.01	60.75 ± 5.87	59	0.97 ± 0.16
2j: OLV	10.44 ± 0.30	3.66 ± 0.10	1.99 ± 0.07	2.39 ± 0.06	7.44 ± 0.36	0.94 ± 0.22	11.12 ± 0.38	20.09 ± 2.34	0.40 ± 0.21	0.01 ± 0.01	42.40 ± 2.42	49	1.16 ± 0.18
2j: $m_{\ell\ell} > 45, 60$ GeV	10.29 ± 0.30	3.66 ± 0.10	1.99 ± 0.07	1.00 ± 0.04	6.65 ± 0.33	0.88 ± 0.22	10.12 ± 0.36	15.51 ± 2.21	0.42 ± 0.21	0.02 ± 0.01	34.60 ± 2.29	44	1.27 ± 0.21
2j: $\Delta\eta_{\ell\ell} < 1.85$	9.19 ± 0.28	3.04 ± 0.10	1.61 ± 0.07	1.00 ± 0.04	5.17 ± 0.30	0.68 ± 0.16	7.21 ± 0.30	15.23 ± 2.21	0.40 ± 0.21	0.01 ± 0.01	29.69 ± 2.27	37	1.25 ± 0.23

Table 6.5.: Cutflow for the high mass 8 TeV analysis for the $ee + \mu\mu$ final state. The background and signal estimates are taken from MC, except for the W+jets and QCD backgrounds which are data-driven. Only statistical uncertainties are shown.

7. Background estimation

In this chapter the event topologies of the Standard Model backgrounds as well as their estimation are presented. To minimize the dependence on generator modeling most of the backgrounds are estimated via a semi or fully data-driven method. The W+jets & QCD estimation is realized via the fake factor method (see section 7.5), a full data-driven estimation. The Drell-Yan process for the low mass analysis ($m_H \leq 200\,\text{GeV}$) is estimated via the so called pacman method (see section 7.4). Other backgrounds like WW, top and other dibosons are normalized to the measured data in specifically designed control regions. The derived normalization factor is calculated using the following formula:

$$\text{NF} = \frac{\text{(data - (total background - process))}}{\text{process}} \tag{7.1}$$

Where "process" is the number of Monte Carlo events for the background in question, "total background" is the total number of expected background events (the sum of monte-carlo events and results from fully data-driven methods) and "data" is the measured number of data events. The normalization factors (NF) get applied as a global, multiplicative factor to the individual backgrounds.

7.1. WW

The WW continuum in the $H \to WW^{(*)} \to \ell\nu\ell\nu$ channel is an irreducible background and one of the leading background contribution in the $N_{\text{jets}} = 0$ and $N_{\text{jets}} = 1$ category. The final state of this background consists of two high p_T leptons and large $\not{E}_{\text{T}}^{\text{miss}}$. For the relatively small Higgs masses $m_H \leq 200\,\text{GeV}$ control regions can be orthogonalized from signal regions via the dilepton invariant mass $m_{\ell\ell}$. For large Higgs masses $m_H > 200\,\text{GeV}$ the separation of control region and signal region is realized via the difference in pseudorapidity of the two leptons in the final state $\Delta\eta_{\ell\ell}$. The WW control regions are separately defined in the exclusive $N_{\text{jets}} = 0$ and $N_{\text{jets}} = 1$ bins for the analyzed mass regions $m_H \leq 200\,\text{GeV}$ & $m_H > 200\,\text{GeV}$. The control regions are not defined for the $ee + \mu\mu$ final state because of lower statistics and lower purity. Furthermore, in the $N_{\text{jets}} \geq 2$ category the large contribution from the top background makes it impossible to define a relatively pure WW control region. Table 7.1 summarizes the selection criteria

for the low mass analysis and Table 7.2 for the high mass analysis. The theoretical uncertainties related to the various backgrounds as well as the uncertainties on the extrapolation or normalization factor are summarized in chapter 8.

Table 7.1.: Event selection criteria for the $m_H \leq 200\,\text{GeV}$ 0 and 1 jet WW control regions in the 7+8 TeV analysis. Masses and momenta are in units of GeV. Only the different-flavor final state is used [66].

Category	H+0	H+1
Pre-selection	Two isolated leptons ($\ell = e, \mu$) with opposite charge DF: $m_{\ell\ell} > 10$ $p_T^{\text{lead}} > 22$, $p_T^{\text{sublead}} > 15$	
Missing transverse momentum	$p_{\text{T}}^{\text{miss}} > 20$	$p_{\text{T}}^{\text{miss}} > 20$
General selection	- $p_T^{\ell\ell} > 30$ $\Delta\phi_{\ell\ell,p_{\text{T}}^{\text{miss}}} > \frac{\pi}{2}$ $55 < m_{\ell\ell} < 110$ $\Delta\phi_{\ell\ell} < 2.6$	$N_{b\text{-jet}} = 0$ $\max\{m_T(\ell, \not{E}_{\text{T}}^{\text{miss}})\} > 50$ - $m_{\ell\ell} > 80$ $\lvert m_{\tau\tau} - m_Z \rvert > 15$

Table 7.2.: Event selection criteria for the $m_H > 200\,\text{GeV}$ 0 and 1 jet WW control regions in the 8 TeV analysis. Masses and momenta are in units of GeV. Only the different-flavor final state is used [63].

Category	H+0	H+1
Pre-selection	Two isolated leptons ($\ell = e, \mu$) with opposite charge DF: $m_{\ell\ell} > 10$ $p_T^{\text{lead}} > 22$, $p_T^{\text{sublead}} > 15$	
Missing transverse momentum	$p_{\text{T}}^{\text{miss}} > 20$	$p_{\text{T}}^{\text{miss}} > 35\,(20)$
General selection	- $p_T^{\ell\ell} > 35$ $m_{\ell\ell} > 75$ $\Delta\eta_{\ell\ell} > 1.35$	$N_{b\text{-jet}} = 0$ -

The purity in the low mass 0 jet WW control region is about 60 % and about 40 % for the 1 jet case. In the high mass WW control region the purity for the 0 jet case is about 70 % and about 44 % for the 1 jet case. The resulting normalization factors are summarized in Table 7.3 and in Figure 7.1 the m_{T} distributions in the 8 TeV WW control regions are shown after applying the resulting normalization factors and moreover, the normalization factors for other backgrounds are also applied.

Table 7.3.: Normalization factors for the WW background obtained in the low and high mass analysis using the 7 and 8 TeV dataset. The uncertainties are only statistical.

dataset	0 jet	1 jet
low mass	1.219 ± 0.033	1.05 ± 0.05
high mass	1.13 ± 0.04	1.15 ± 0.07

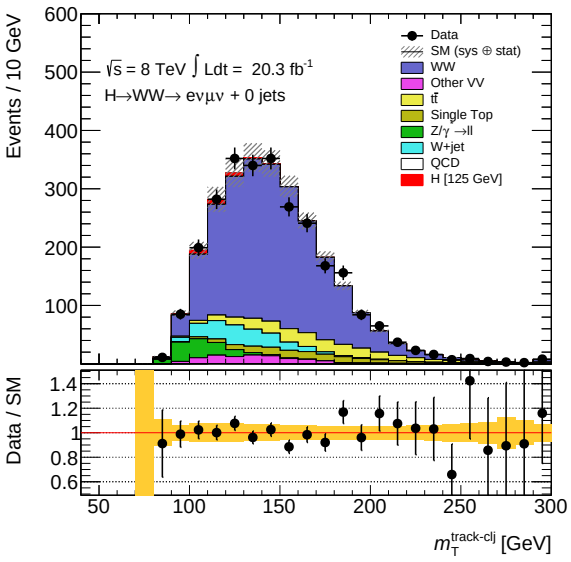

(a) low mass 8 TeV 0 jet WW CR

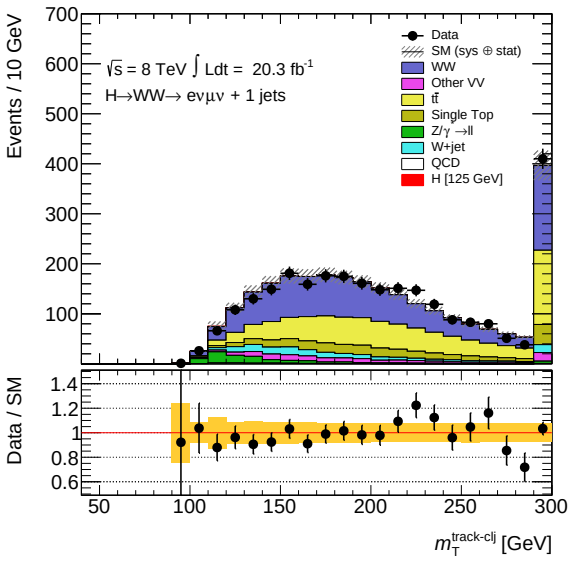

(b) low mass 8 TeV 1 jet WW CR

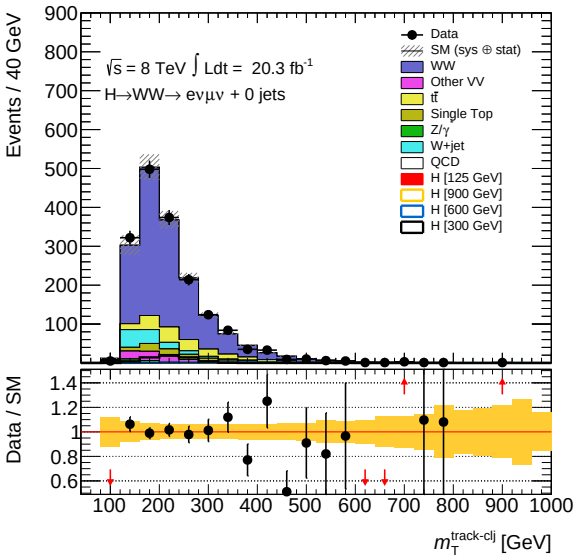

(c) high mass 8 TeV 0 jet WW CR

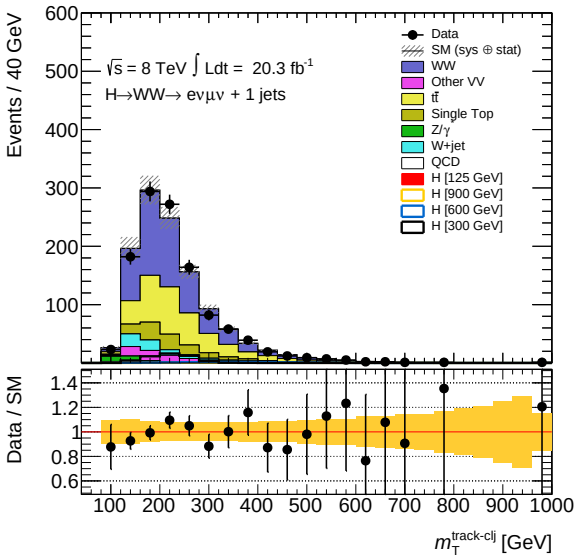

(d) high mass 8 TeV 1 jet WW CR

Figure 7.1.: The distributions show the transverse mass m_{T} for the 8 TeV low and high mass WW control regions. All normalization factors are applied

7.2. Top

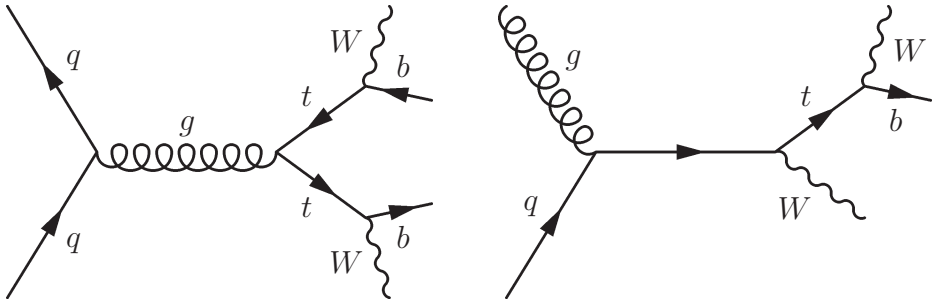

(a) top-anti-top pair production and decay (b) single top production and decay

Figure 7.2.: Feynman diagrams for the production and decay of a top-anti-top pair and for a single top.

At hadron colliders such as the LHC, top quarks are produced in pairs ($t\bar{t}$), in association with a W boson (Wt) or with an associated quark (single-t). Figure 7.2 shows the Feynman diagrams of the leading order top anti top pair production and the Wt production. Top quarks almost exclusively decay into a W-boson together with a b-quark [17] where the W boson then can further decay into a lepton-neutrino pair. This means that top events in general can also create 2 leptons with large $\not{E}_{\mathrm{T}}^{\mathrm{miss}}$ (plus one or two b-jets) in the final state, similar to the event signature of $H \to WW^{(*)} \to \ell\nu\ell\nu$ events. The top background is for events with $N_{\mathrm{jets}} \geq 1$ a dominant background and also in the 0 jet case a proper treatment is appreciated. The following section will describe the semi data-driven methods used in the 0, 1 and ≥ 2 jet categories.

7.2.1. Jet-veto survival probability method - $N_{\mathrm{jets}} = 0$

For the $N_{\mathrm{jet}} = 0$ category the amount of top background in the signal region is determined applying the so called jet-veto survival probability (JVSP) [77] method. The estimation of top events in the signal region can be summarized with the following formula:

$$N_{\mathrm{Top,0j}}^{\mathrm{Exp}} = (N_{\mathrm{data}} - N_{\text{non-top}}) \times P_2^{\mathrm{Exp}}, \tag{7.2}$$

where N_{data} represents in the low mass analysis the total number of data events after the pre-selection including a cut on $p_{\mathrm{T}}^{\mathrm{miss}} > 20\,\mathrm{GeV}$ and $\Delta\phi_{\ell\ell} < 2.8$ for $e\mu + \mu e$ events only. In the high mass analysis N_{data} is obtained after the pre-selection cuts, cuts on $p_{\mathrm{T}}^{\mathrm{lead}} > 60\,\mathrm{GeV}$, $p_{\mathrm{T}}^{\mathrm{sub}} > 30\,\mathrm{GeV}$ and a cut on $E_{\mathrm{T,rel}}^{\mathrm{miss}} > 45\,\mathrm{GeV}$. Moreover, in the high mass analysis only the DF events are used. The choice for using the different flavor events exclusively is based on the fact that in $e\mu + \mu e$ the Z+jets contamination is relatively small compared

to $ee + \mu\mu$ events at that early stage in the cutflow. The quantity "$N_{\text{non-top}}$" refers to the contribution from the non-top backgrounds at the same cut stages. This is determined either by the data-driven estimation (e.g. W+jets and QCD) or the MC predictions. The observable P_2^{Exp} corresponds to a data-driven estimate of top events passing the jet-veto cut. It bears an analogy in the MC expectation $N_{\text{top,0j}}^{\text{MC}} = N_{\text{all top}}^{\text{MC}} \times P_2^{\text{MC}}$. The data-driven P_2^{Exp} is derived using:

$$P_2^{\text{Exp}} = P_2^{\text{MC}} \times \left(\frac{P_1^{\text{data}}}{P_2^{\text{MC}}} \right)^2 \tag{7.3}$$

$$\approx P_2^{\text{MC}} \times \left(\frac{P_1^{\text{Btag,data}}}{P_2^{\text{Btag,MC}}} \right)^2 \tag{7.4}$$

where $P_1^{\text{data (MC)}}$ is a single jet veto survival probability in data (MC) and $P_1^{\text{Btag, data (MC)}}$ is the corresponding jet veto survival probability determined from a control sample in which it is required to have at least one b-tagged jet. Equation (7.3) is formed under the assumption that $P_2 = P_1^2$. More details on the JVSP method can be found in Ref. [77] and Ref. [69]. The normalization factor which is applied to the top background is determined from the ratio of $N_{\text{Top,0j}}^{\text{Exp}}$ and $N_{\text{Top, 0j}}^{\text{MC}}$ from $e\mu + \mu e$ events only. Table 7.4 summarizes the obtained normalization factors using the JVSP method.

Table 7.4.: Normalization factors for the top background via the JVSP method for the low and high mass analysis. The uncertainties are statistical only.

dataset	0 Jet (JVSP)
low mass	1.082 ± 0.024
high mass	0.993 ± 0.008

7.2.2. Top estimation for $N_{\text{jets}} = 1$

For the estimation of the top background in the $N_{\text{jets}} = 1$ bin the low mass analysis makes use of a data-driven method which extracts a top estimation via the measurement of the b-tagging efficiency. In this method, events in data with two jets are selected where one jet is required to be a b-tagged jet (tag jet). This selection criterion ensures that the sample is highly enriched with $t\bar{t}$. The non-top events are subtracted as in the JVSP method (see section 7.2.1) by the MC predictions and the fully data-driven W+jets and QCD estimation. The b-tagging efficiency $\epsilon_{\text{tag}}^{\text{data,2jetCR}}$ is defined as the ratio of events with 2 jets and the number of events where also the second jet (besides the tag-jet) is b-tagged. The same observable is determined for MC $\epsilon_{\text{tag}}^{\text{MC,2jetCR}}$. To account for an eventual bias from the 2 jet control region on the b-tagging efficiency a correction $f_{\text{correction}}$ is introduced.

The latter is purely based on MC, obtained from the ratio $\epsilon_{\text{tag}}^{\text{MC,1jetCR}}$ over $\epsilon_{\text{tag}}^{\text{MC,2jetCR}}$. The measured event in the 1 jet signal region for the low mass analysis can then be expressed as

$$N_{\text{Top}}^{\text{data,1jetSR}} = \frac{N_{\text{Top}}^{\text{data,1jetCR}}}{\epsilon_{\text{tag}}^{\text{data,2jetCR}} \cdot f_{\text{correction}}} \cdot (1 - \epsilon_{\text{tag}}^{\text{data,2jetCR}} \cdot f_{\text{correction}}). \tag{7.5}$$

The resulting NF is then defined as the ratio of MC top events $N_{\text{Top}}^{\text{MC,1jetSR}}$ and $N_{\text{Top}}^{\text{data,1jetSR}}$ with a resulting value of 1.026 ± 0.024 for the 8 TeV dataset (statistical uncertainties only). The 2 jet control region is defined after the pre-selection cuts and a cut on $\max\{m_T(\ell, \not{E}_{\text{T}}^{\text{miss}})\} > 50\,\text{GeV}$ for the DF events only [69].

In the high mass analysis a normalization factor as defined in equation (7.1) is obtained from a control region which is defined as summarized in Table 7.5. The control region is supposed to be close to the signal region definition hence the hard lepton p_{T} cuts. The resulting normalization factors for high mass is 1.055 ± 0.029 (statistical uncertainties only).

Table 7.5.: Event selection criteria for the 1 jet top control regions in the high mass analysis. Masses and momenta are in units of GeV. Only the different flavor final state is used [63].

Category	H+1
Pre-selection	Two isolated leptons ($\ell = e, \mu$) with opposite charge DF: $m_{\ell\ell} > 10$ $p_{\text{T}}^{\text{lead}} > 55$, $p_{\text{T}}^{\text{sub}} > 35$
Missing transverse momentum	DF: $p_{\text{T}}^{\text{miss}} > 20$ DF: $p_{\text{T,rel}}^{\text{miss}} > 20$
Top-enrichment	$N_{b\text{-jet}} \geq 1$

In Figure 7.3 the m_{T} distribution for the 8 TeV high mass $N_{\text{jets}} = 1$ top control region is shown.

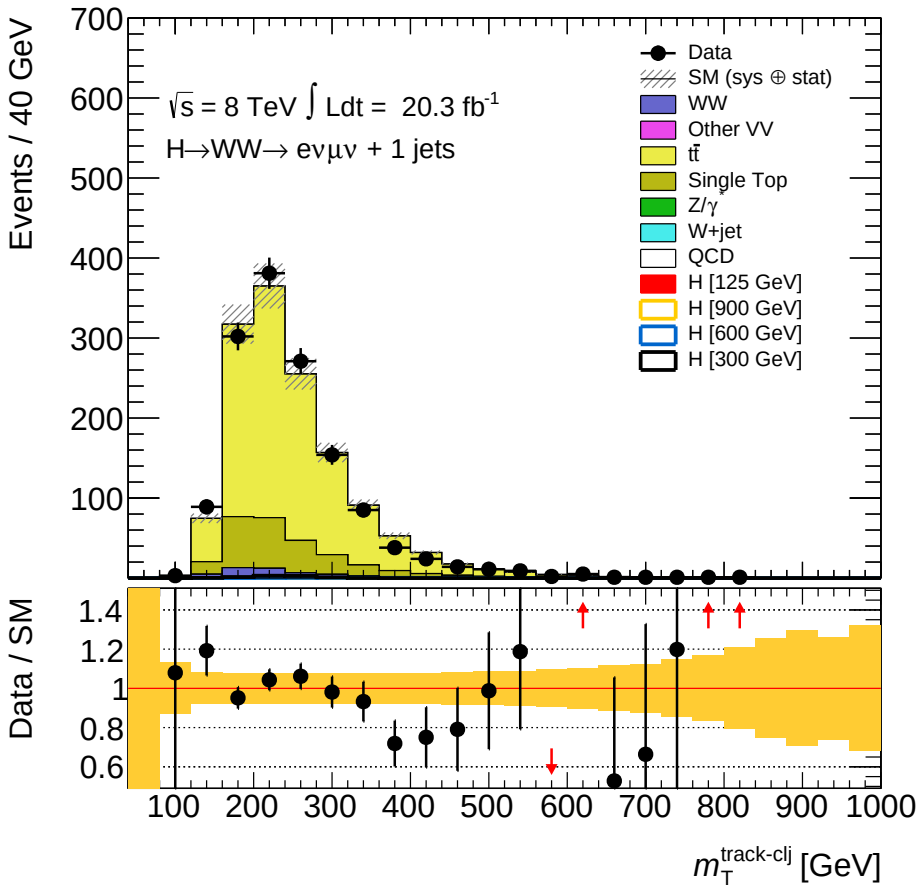

Figure 7.3.: The distribution shows the transverse mass m_{T} for the high mass top control region in the $N_{\mathrm{jets}} = 1$ bin. All normalization factors are applied.

7.2.3. Top estimation for $N_{\mathrm{jets}} \geq 2$

For the high mass ≥ 2 jet category the top control region is defined with a requirement to have exactly one b-jet in the event. To use as much data statistics as possible in the 2 jet top control region both the different flavor and the same flavor final state is used. It is assumed that any mismodeling of the VBF criteria is independent of lepton flavor. Table 7.6 the selection criteria for the 2 jet category top control region are summarized.

Table 7.6.: Event selection criteria for the 2 jet top control regions in the high mass analysis. Masses and momenta are in units of GeV. Only the different flavor final state is used [63].

Category	H+2
Pre-selection	Two isolated leptons ($\ell = e, \mu$) with opposite charge DF: $m_{\ell\ell} > 10$ SF: $m_{\ell\ell} > 12$, $\lvert m_{\ell\ell} - m_Z \rvert > 15$
	$p_{\mathrm{T}}^{\mathrm{lead}} > 45$, $p_{\mathrm{T}}^{\mathrm{sub}} > 20$
Missing transverse momentum	DF: $E_{\mathrm{T}}^{\mathrm{miss}} > 20$ SF: $E_{\mathrm{T}}^{\mathrm{miss}} > 20$
Top-enrichment	$N_{b\text{-jet}} = 1$
VBF topology	$\Delta Y_{jj} > 4.0$; $m_{jj} > 500$

For the high mass analysis the resulting normalization factor is 1.01 $\pm$ 0.06 (statistical uncertainties only). Figure 7.4 shows the m_{T} distribution in the high mass $\geq$ 2 jet control region for different flavor and same flavor combined.

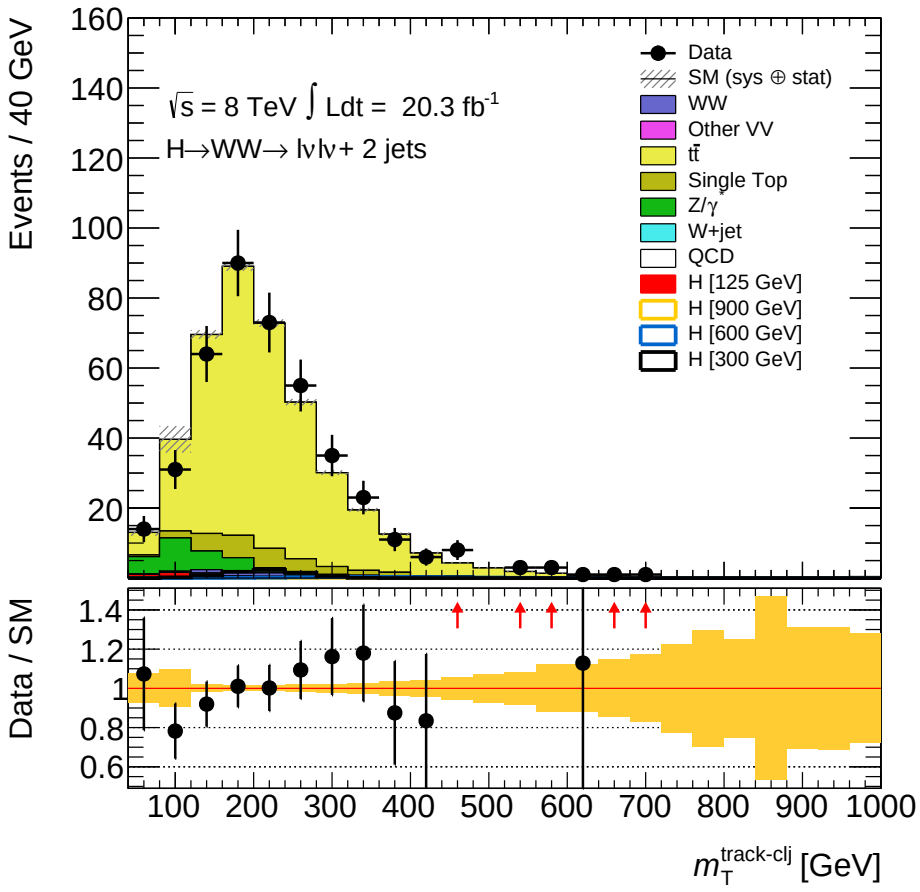

Figure 7.4.: The distribution shows the transverse mass m_{T} for the high mass ≥ 2 jet top control region. All normalization factors are applied

7.3. Other dibosons

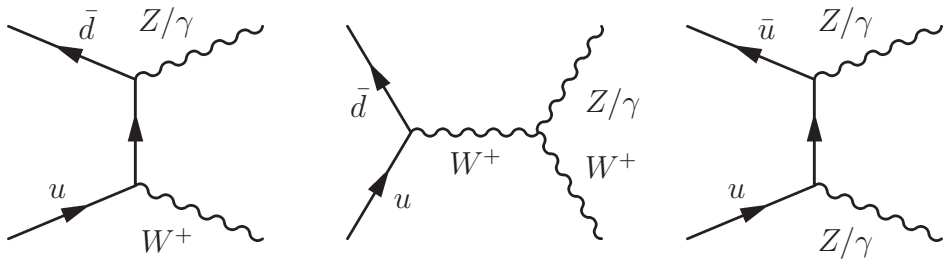

Figure 7.5.: Leading order diagrams of non-WW diboson production.

There is one set of background processes which originates from the decay of two gauge bosons like WZ,ZZ,$W\gamma$ or $W\gamma^*$. This type of decays is summarized under the notation "other dibosons", "VV" or "non-WW". Figure 7.5 shows the dominant production diagrams of non-WW background processes. The ZZ or WZ decays can mimic $H\to WW^{(*)}\to \ell\nu\ell\nu$ events if one or more leptons are missed. $ZZ \to \ell^+\ell^-\nu\nu$ events are suppressed in the same flavor channel by the Z-window cut. $W\gamma$ or $W\gamma^*$ decays can also fake an event signature with 2 leptons and large $\not{E}_{\mathrm{T}}^{\mathrm{miss}}$ if the $\gamma^{(*)}$ is mis-identified as an electron. In the high mass analysis the other diboson background is estimated from MC alone. This is due to the fact that the contribution from those events is on the order of 3 % for the $m_H > 200\,\mathrm{GeV}$ analysis. In the low mass analysis ($m_H \leq 200\,\mathrm{GeV}$) the other diboson events contribute up to 10 % to the total background composition in the $N_{\mathrm{jets}} \leq 1$ categories which is roughly on the same order of magnitude as the signal expectation. Owing to the fact that $W\gamma^{(*)}$ and WZ events are equally likely to produce two oppositely charged leptons as two leptons with the same charge, so called same-sign events are used in order to design a "Non-WW" control region. By requiring to have two equally charged leptons (or same-sign leptons) the $H\to WW^{(*)}\to \ell\nu\ell\nu$ signal, top, WW and $Z/\gamma^* \to \ell\ell$ processes are rejected. Only events from W+jets, QCD and other dibosonic backgrounds survive a selection which requires two same-sign (SS) leptons. The assumption that the contribution from the "Non-WW" events is symmetric for same-sign and opposite-sign events is only a valid approximation for $e\mu + \mu e$ events. Therefore, only the DF final state is used for the SS control region. The SS control region is defined using events passing the DF signal region definition for the $m_H \leq 200\,\mathrm{GeV}$ 0 and 1 jet analysis up to the cut on $\Delta\phi_{\ell\ell}$. The resulting normalization factors are 0.92 $\pm$ 0.07 (stat.) for 0 jet and 0.96 $\pm$ 0.12 for 1 jet. In Figure 7.6 the transverse mass distributions for the 0 jet (left) and 1 jet (right) SS control regions are shown.

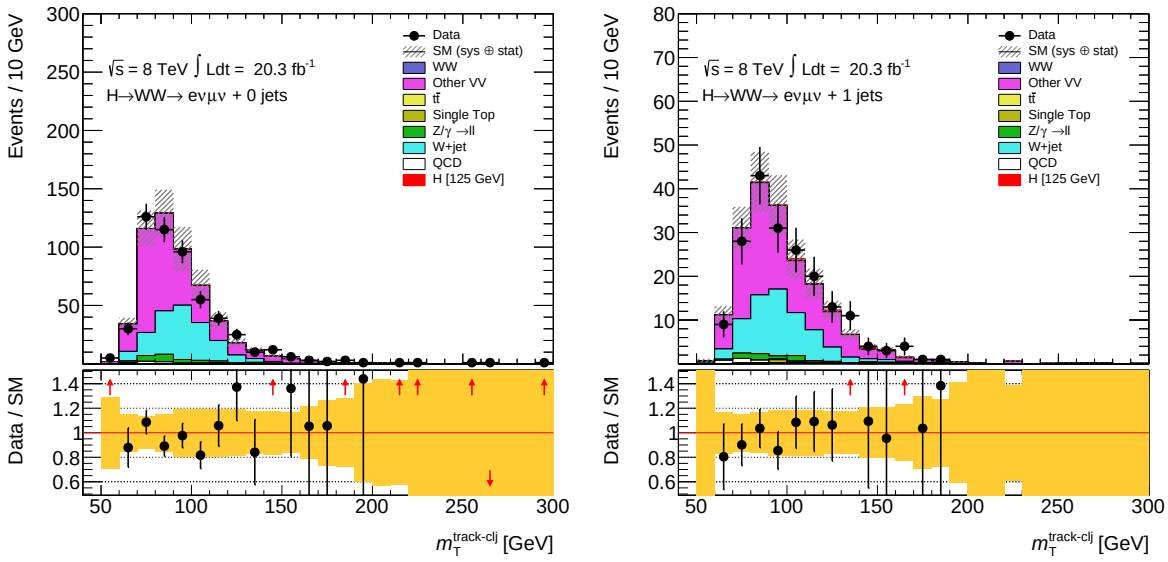

(a) m_{T} in the same sign 0 jet control region (b) m_{T} in the same sign 1 jet control region

Figure 7.6.: The distributions show the transverse mass m_{T} for the 8 TeV low mass same sign control region. All normalization factors are applied

7.4. Drell-Yan

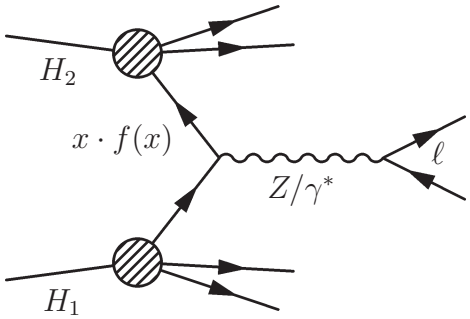

Figure 7.7.: The Drell-Yan process. The two incoming lines H_1 and H_2 together with the two blobs, represent two initial state hadrons. The lines which are extracted from the shaded blobs, mean that the relevant PDF (see section 2.3) is used to find the probability of finding that parton in the hadron represented by the blobs.

The Drell-Yan process as shown in Figure 7.7, produces two oppositely charged leptons and can be reconstructed with $\not{E}_{\mathrm{T}}^{\mathrm{miss}} > 0\,\mathrm{GeV}$ due to neutrinos originating from $Z/\gamma^* \to \tau\tau$, heavy quark decays or detector resolution effects. Due to the hard lepton p_{T} cuts in the high mass analysis the Drell-Yan process is a negligible background contribution with one exception, the $ee + \mu\mu\,2$ jet signal region. In the $m_H > 200\,\mathrm{GeV}\,0$ jet case the Z+jets background contributes roughly 1 % of the total background and about 3 % in the 1 jet case. For the 2 jet signal region the Z+jets contributes 5 % in the different flavor channel and about 52 % in the same flavor channel case. Even though the contribution of Drell-Yan in the 2 jet $ee + \mu\mu$ high mass signal region is not negligible, the prediction is taken purely from MC. To reduce statistical uncertainties in the analyzed high $m_{\ell\ell}$ region, the high mass analysis uses Z+jets MC samples with more than 5 millions events per lepton flavor ($Z \to (ee, \mu\mu, \tau\tau)$) for $m_Z^{\mathrm{truth}} > 100\,\mathrm{GeV}$. In the low mass analysis the Z/γ^* background is estimated via two methods. The $Z/\gamma^* \to \tau\tau$ contribution is estimated from a control region where a normalization factor is obtained. The $Z/\gamma^* \to ee/\mu\mu$ background for $N_{\mathrm{jets}} \leq 1$ is obtained via a data-driven estimation called "pacman method". In the following sections those two background estimations will be described briefly.

7.4.1. $Z/\gamma^* \to \tau\tau$

To remove the contribution from $Z/\gamma^* \to ee/\mu\mu$ in the $\tau\tau$ control region, it is defined using $e\mu + \mu e$ events only. For the $N_{\mathrm{jets}} = 0$ case the control region is defined after the pre-selection cuts with further requiring $m_{\ell\ell} < 80\,\mathrm{GeV}$ and $\Delta\phi_{\ell\ell} > 2.8$. The normalization factor obtained is 1.00 ± 0.02 (stat.). In the $N_{\mathrm{jets}} = 1$ category also the pre-selection cuts are applied and furthermore, the invariant $\tau\tau$ mass is required to be greater than $(m_{\mathrm{Z}} - 25\,\mathrm{GeV})$ and a cut $m_{\ell\ell} < 80\,\mathrm{GeV}$ is applied. The resulting normalization factor for the 1 jet bin is 1.06 ± 0.04.

7.4.2. $Z/\gamma^* \to ee/\mu\mu$

The fractional jet recoil f_{recoil} shows a clear difference in the shape between Drell-Yan and all other background processes with real $\not{E}_{\mathrm{T}}^{\mathrm{miss}}$ (e.g. neutrinos) in the final state. In the same flavor low mass 0 and 1 jet analysis a method is used which measures the cut efficiency on f_{recoil} in data and uses the estimation of DY after a cut on f_{recoil} . Figure 7.8 shows f_{recoil} for $ee + \mu\mu$ events in the low mass 0 and 1 jet category where the dominant contribution of the Z/DY process is distributed in the region $f_{\mathrm{recoil}} > 0.1$

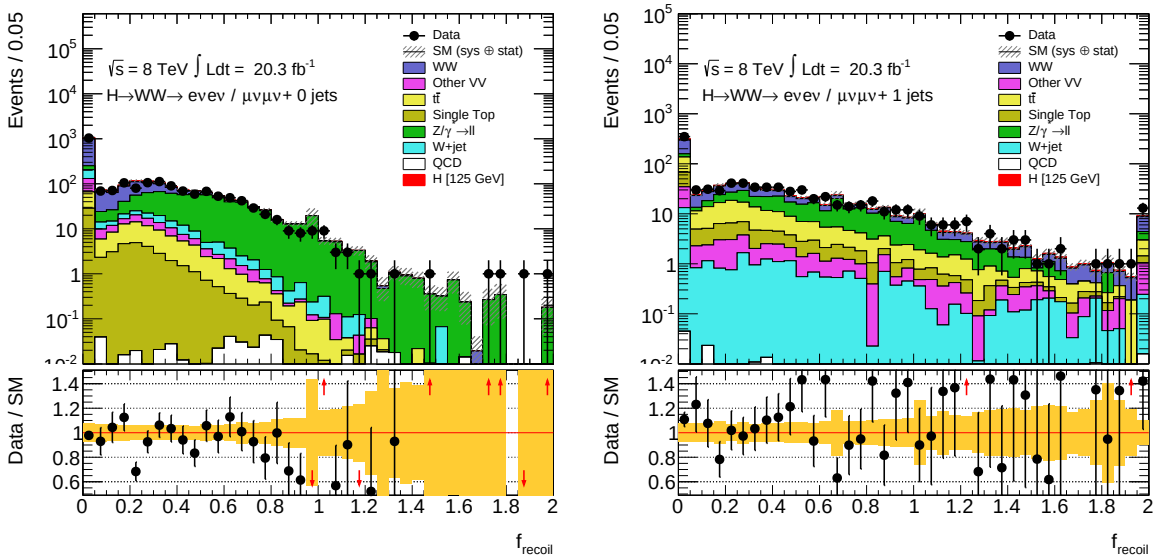

(a) f_{recoil} in the 0 jet category

(b) f_{recoil} in the 1 jet category

Figure 7.8.: The distributions show the relative jet recoil f_{recoil} for the 8 TeV low mass 0 and 1 jet category for $ee + \mu\mu$ events. All normalization factors are applied

A control sample of events is divided into two bins: passing N_{pass} and failing N_{fail} the f_{recoil} cut. The former actually defines the signal region for the SF low mass 0 and 1 jet analysis. The efficiency of the f_{recoil} cut is then obtained via $\alpha = N_{\text{pass}}/(N_{\text{pass}} + N_{\text{fail}})$. The efficiency α is measured separately for data, Drell-Yan background and non-DY background. Together with the observed events passing the f_{recoil} cut a normalization factor can then be obtained via inverting the matrix

$$\begin{pmatrix} N_{\text{pass}} \\ N_{\text{pass}} + N_{\text{fail}} \end{pmatrix} = \begin{pmatrix} 1 & 1 \\ 1/\alpha_{\text{DY}} & 1/\alpha_{\text{non-DY}} \end{pmatrix} \cdot \begin{pmatrix} B_{\text{DY}} \\ B_{\text{non-DY}} \end{pmatrix} \tag{7.6}$$

and solving for B_{DY}, the estimation of Drell-Yan events in the $ee + \mu\mu$ signal regions. The efficiency for the non-DY backgrounds $\alpha_{\text{non-DY}}$ is measured in a sample using $e\mu + \mu e$ events only in order to increase the purity. The resulting normalization factors are 1.24 ± 0.10 (stat.) in the 0 jet category and 1.50 ± 0.20 (stat.) in the 1 jet category [70].

7.5. W+jets & QCD

Events where a W boson is produced in association with jets and the W boson decays into a lepton neutrino pair, can contribute to the total background if one of the jets is misidentified as a lepton. The misidentification rate may not be modeled correctly in MC samples. Therefore, a data-driven estimate of this background is implemented in the $H \to WW^{(*)} \to \ell\nu\ell\nu$ analyses. The method itself is called the "Fake Factor Method". Also QCD multi-jet events can give a rise to the total background contribution. The probability of misidentifying jets from the QCD background as two leptons together with $\not{E}_{\mathrm{T}}^{\mathrm{miss}} > 0$ GeV is relatively small but the cross section of QCD events is presumably very large. The multi-jet background is obtained via the same "Fake Factor Method" as the W+jets background. The estimation of those two backgrounds is the same for the low- and high mass analysis.

For the "Fake Factor Method" three samples are defined: a signal sample, a W+jets control sample and a QCD control sample. The signal sample is exactly what is used in the signal region definitions of the $H \to WW$ analyses which means those are the events which contain two fully identified leptons in data. It can be expressed in a way to explicitly include the contribution from W+jets and QCD:

$$N_{\mathrm{id+id}} = N_{\mathrm{id+id}}^{\mathrm{QCD}} + N_{\mathrm{id+id}}^{W+\mathrm{jets}} + N_{\mathrm{id+id}}^{\mathrm{EW}} \tag{7.7}$$

where $N_{\mathrm{id+id}}$ is the signal sample, $N_{\mathrm{id+id}}^{\mathrm{QCD}}$ is the QCD background, $N_{\mathrm{id+id}}^{W+\mathrm{jets}}$ is W+jets contribution to the background and $N_{\mathrm{id+id}}^{\mathrm{EW}}$ are all other backgrounds. The subscript "id+id" refers to the requirement that in this sample both leptons have to fulfill the object quality criteria as described in chapter 5. The W+jets control sample is defined using an alternative lepton definition to enhance the probability of a jet faking an electron. Objects which pass this alternative object definition are referred to as "anti-id"[1]. The "anti-id" objects are explicitly asked to fail the object identification criteria. Isolation and track impact parameter requirements are either relaxed or removed. The W+jets control sample is then defined to contain one fully identified lepton and one anti-id object. The control sample can be expressed similarly as in equation (7.7):

$$N_{\mathrm{id+anti-id}} = N_{\mathrm{id+anti-id}}^{\mathrm{QCD}} + N_{\mathrm{id+anti-id}}^{W+\mathrm{jets}} + N_{\mathrm{id+anti-id}}^{\mathrm{EW}} \tag{7.8}$$

And hence the QCD control sample is constructed with two anti-id objects and can be expressed in a similar way:

$$N_{\mathrm{anti-id+anti-id}} = N_{\mathrm{anti-id+anti-id}}^{\mathrm{QCD}} + N_{\mathrm{anti-id+anti-id}}^{W+\mathrm{jets}} + N_{\mathrm{id+anti-id}}^{\mathrm{EW}} \tag{7.9}$$

[1] abbreviation for anti identified object

In order to obtain the number of W+jets and QCD events in the signal region, an extrapolation factor is introduced. This extrapolation factor relates the number of W+jets and QCD events in the control samples with the number of W+jets and QCD events in the signal regions. The factor itself is defined as the ratio of the number of jets satisfying the full lepton identification over the number of jets satisfying the anti-id selection:

$$f_\ell = \frac{N_{\text{id}}}{N_{\text{anti-id}}} \quad (\ell = e \text{ or } \mu) \tag{7.10}$$

The extrapolation factor or fake-factor f_ℓ (hence the name "Fake Factor Method") is defined for both electrons and muons. This fake factor is measured in data using di-jets and Z+jets events with either the e^+e^- or the $\mu^+\mu^-$ final state. The fake factor is binned in lepton p_{T} bins for 10 GeV - 15 GeV, 15 GeV - 20 GeV, 20 GeV- 25 GeV and >25 GeV. Figure 7.9 shows the fake factor measured in data from Z+jets events for electrons and muons compared with the predicted fake factors from Monte Carlo simulations.

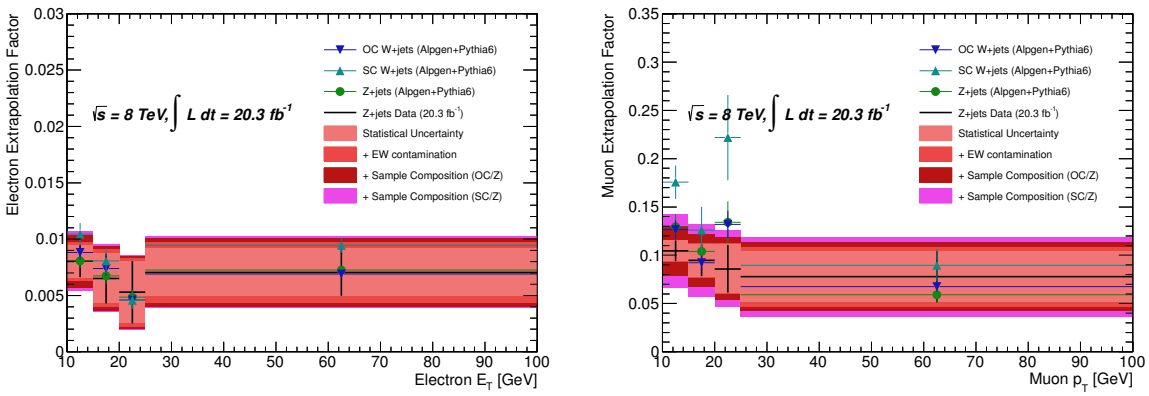

fake factor for electrons fake factor for muons

Figure 7.9.: Fake factors for electrons (left) and muons (right) as a function of anti-id lepton p_{T}. The fake factors were obtained in Z+jets events for data and are compared with predictions by various MC simulations. The EW contamination uncertainty is based on the uncertainty from the subtraction of other electroweak processes in the Z+jets control sample. The sample composition uncertainties reflect the dependence of the fake factor on the Monte Carlo generator used and the dependence of the fake factor on same charge (SC) and opposite charge (OC) events [69].

The W+jets background can then be calculated by scaling the number of event in the

W+jets control sample by the fake factor:

$$N^{W+\text{jet}}_{\text{id+id}} = f_\ell \cdot N^{W+\text{jet}}_{\text{it+anti-id}} \tag{7.11}$$

$$= f_\ell \cdot (N_{\text{it+anti-id}} - N^{\text{EW}}_{\text{it+anti-id}} - N^{\text{QCD}}_{\text{it+anti-id}}) \tag{7.12}$$

where $N^{\text{EW}}_{\text{it+anti-id}}$ is subtracted using pure MC and $N^{\text{QCD}}_{\text{it+anti-id}}$ is subtracted using the $N_{\text{anti-id+anti-id}}$ events. In the low mass analysis W+jets & QCD contributes about 15 % for 0 jet and roughly 7 % in the 1 jet category. In high mass the contribution from W+jets & QCD is 2 % for 0 jet, 3 % for 1 jet and about 2.5 % for ≥ 2 jets.

8. Systematic uncertainties

Systematic uncertainties are a very important part of the analysis. They enter the fit (see chapter 9) as nuisance parameters in the likelihood function. The proper treatment of any source of uncertainties has a direct influence on the quality of the obtained results. Uncertainties can be separated into two categories: Detector uncertainties and theoretical uncertainties. For experimental uncertainties the parameter in question is varied by $\pm 1\sigma$ while re-running all of the object and signal region selection to determine the impact on the acceptance. The number of individual uncertainties is rather large. The number of detector systematics for a SM-like Higgs boson with a mass of $m_H = 800\,\text{GeV}$ is about 58[1]. In the following, a summarized overview of the detector and theory uncertainties will be given. More details on all used systematics can be found in [69], [43] and [70]. Some systematics are specific for individual processes and will be presented at the end of this chapter.

8.1. Uncertainties associated with leptons

For the leptons (electron or muons) the reconstruction and identification, the energy scale as well as the energy resolution are sources of uncertainties. The uncertainties (including uncertainties on trigger efficiencies) are estimated using $Z \to ee/\mu\mu, J/\psi \to ee/\mu\mu$ and $W \to e\nu, \mu\nu$ decays. Table 8.1 summarizes the estate of the uncertainties for electrons and muons. The size of the uncertainties is obtained depending on E_T and η for electrons and muons [66].

[1] This number depends slightly on production mechanism, model interpretation, mass of signal and so on.

Uncertainty source	Size of the uncertainty
Electron Efficiency	0.1 % - 1.0 % reconstruction
	0.2 % - 2.6 % identification
Electron energy scale	about 0.4 %
Electron Energy Resolution	about 1 %
Muon Efficiency	$<$ 0.46 % - 1.0 %
Muon Energy scale	$<$ 0.50%
Muon Energy Resolution	less than 1 %

Table 8.1.: The size and source of the lepton uncertainties. All uncertainties depend on the lepton E_T and η. Only the range of the uncertainty is shown here [66].

The uncertainty on the trigger efficiencies is found to be smaller than 1 % [66] (see also section 3.4.1).

8.2. Uncertainties associated with jets

In general jets are very complex objects. In the treatment of the systematic uncertainties many sources of uncertainties have to be considered. The uncertainties on jets are categorized into two sources of uncertainties: the jet energy scale (JES) and the jet energy resolution (JER) uncertainties. The JES itself is determined from a combination of simulation, *in situ*[2] measurements [43] and with test beams in the LHC. The JES systematic is derived as a function of jet p_T and jet η. The uncertainty on the JES is in practice separated in the following categories: modeling and statistics on the method for the η intercalibration of jets from the central region to the forward region, high-p_T jet behavior, MC non-closure, different quark/gluon composition and response, the b-jet energy scale, impact from in-time and out-of-time pile-up and *in situ* jet energy corrections [43]. In Figure 8.1 the JES uncertainty for central ($|\eta| = 0.0$, left) and forward ($|\eta| = 3.5$, right) jets is shown.

[2]For example a tag and probe method.

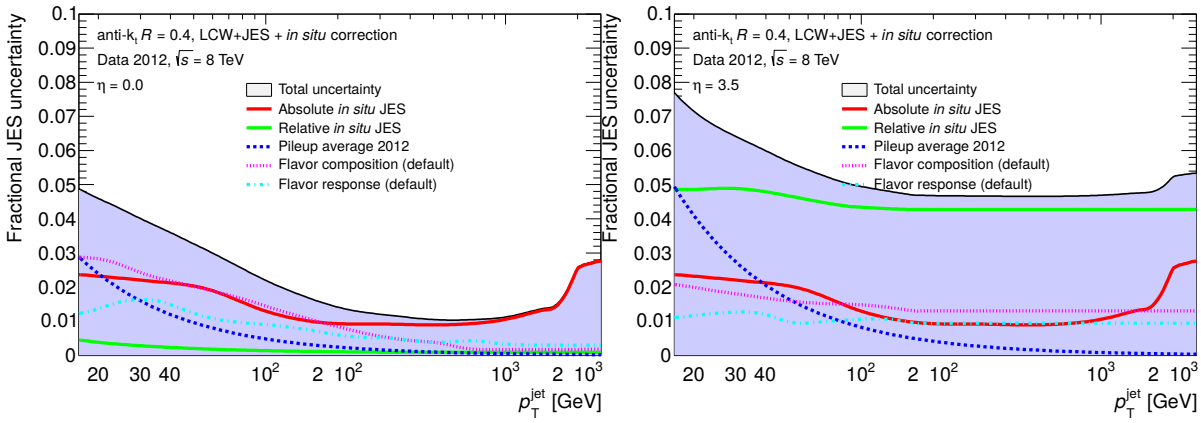

JES uncertainty for central jets JES uncertainty for forward jets

Figure 8.1.: The distributions show total JES uncertainties for central (left) and forward (right) jets as a function of jet p_T [43].

The JES uncertainty is 1 % - 7 % for jets with $p_T > 25\,\text{GeV}$ and $|\eta| < 4.5$ depending on jet-p_T and η. The JER uncertainty varies from 5 % to 20 % depending on jet p_T and jet η [43].

b-tagging plays an important role in the rejection of top background. The uncertainty on the b-jet tagging is estimated with a likelihood fit to the data in a sample with dileptonic top pair events. The b-jet tagging uncertainty is decomposed into into six uncorrelated components. The number of components is based on the number p_T bins used in the calibration. The uncertainty itself ranges from $< 1\%$ to 7.8% [69]. The uncertainty for a c-jet to be reconstructed as a b-jet ranges between 6 % - 14 % depending on jet p_T and the uncertainty for light jets to be misidentified as a b-jet ranges from 9 % to 19 % depending on η and p_T.

8.3. Uncertainties associated with missing transverse energy

As mentioned earlier two $\not{E}_T^{miss}$ definitions are used in the $H \to WW$ analyses. The calorimeter based missing transverse energy E_T^{miss} and the track based missing transverse energy or momentum p_T^{miss}. The transverse missing energy is a composition of all hard objects in the event as well as all remaining measurements, the so called soft terms in the $\not{E}_T^{miss}$. All uncertainties related to the hard objects (leptons & jets) are propagated to the $\not{E}_T^{miss}$ calculation. The only part specific for the $\not{E}_T^{miss}$ calculation is the systematic on the soft terms in any $\not{E}_T^{miss}$ definition (E_T^{miss} and p_T^{miss}). The overall

total uncertainty has been obtained by the ATLAS Jet+$\not{E}_{\mathrm{T}}^{\mathrm{miss}}$ combined performance group and was determined to be 17 % for calorimeter based $\not{E}_{\mathrm{T}}^{\mathrm{miss}}$ in the low- and high mass signal regions [66]. For the track based missing transverse energy the uncertainties have been estimated in Z events where data and simulations have been compared. It was found that the scale variations range from $0.3\,\mathrm{GeV} - 1.4\,\mathrm{GeV}$ and the resolution for $p_{\mathrm{T}}^{\mathrm{miss}}$ ranges from $1.5\,\mathrm{GeV} - 3.3\,\mathrm{GeV}$ [66], [43]. In general the uncertainty originating from $p_{\mathrm{T}}^{\mathrm{miss}}$ is relatively small $< 0.5\%$.

8.4. Luminosity and Pile Up

For pile up related systematics a dedicated pile up control region was defined. The control region is defined for $ee + \mu\mu$ events within the Z-peak $|m_{\ell\ell} - m_{\mathrm{Z}}| < 15\,\mathrm{GeV}$ and further requiring to have exactly one jet with a relaxed cut on the jet vertex fraction JVF: $0 < |\mathrm{JVF}| < 0.1$. A total systematic input of 0.5% for the $N_{\mathrm{jets}} = 0$ and $N_{\mathrm{jets}} = 1$ category was found. For the VBF category $N_{\mathrm{jets}} \geq 2$ a total systematic of 1.0% has been determined [66]. The uncertainty for the 8 TeV data on the integrated luminosity was found to be 2.8 % where the derivation methodology is based on beam-separation scans also known as *van der Meer* scans. More details can be found in Ref. [64].

8.5. Theoretical uncertainties

In the following, the theoretical uncertainties on background processes as well as on signal processes are summarized. Since many backgrounds are normalized to data in control regions (see chapter 7) theoretical uncertainties on the cross sections are not essential. Therefore an uncertainty on the control region to signal region extrapolation is necessary for most background processes. For the background processes the theoretical uncertainties considered are the QCD scale variation, parton showering and underlying event modeling (UEPS) and parton density function (PDF) modeling.

WW background

For WW background the QCD scale uncertainties are evaluated by varying factorization and renormalization scales in aMC@NLO. The PDF uncertainties are obtained from CT10 PDF eigenvectors [78] and a comparison between CT10, MWST2008 [79] and NNPDF2.3 PDFs [80]. The UEPS uncertainty is evaluated by comparing the normalization factors from Powheg+Pythia8 with the NF obtained with samples generated using Powheg+Pythia8 and Powheg+Herwig. The total uncertainty on the extrapolation or normalization factor ranges from 2.0 % to 7.1 % for the low mass analysis,

depending on subleading lepton p_{T} and jet multiplicity [66]. In Table 8.2 the uncertainties for the WW control region to signal region extrapolation for the high mass analysis are summarized.

Table 8.2.: Theoretical systematic uncertainties on the WW control region to signal region extrapolation. In the case of numbers derived from statistically limited samples, the statistical uncertainty on the uncertainty is quoted [63].

Jet bin	UEPS unc (%)	Modelling unc (%)	PDF unc (%)	QCD scale unc (%)
0	2.8 ± 0.2	7.7 ± 0.3	1.0	0.9 ± 0.5
1	3.1 ± 0.2	7.7 ± 0.3	1.4	1.9 ± 0.4

top background

In the low mass analysis the total theoretical uncertainty on the top quark background is estimated to be 7.5 % for the $N_{\mathrm{jets}} = 0$ category. This includes a theoretical uncertainty on $t\bar{t}$ and Wt interference [66]. For the low mass $N_{\mathrm{jets}} = 1$ the total uncertainty is found to be 3.1%. In Table 8.3 the theoretical uncertainties on the top control region to signal region extrapolation for the high mass analysis are summarized.

Table 8.3.: Theoretical systematic uncertainties on the top control region to signal region extrapolation. In the case of numbers derived from statistically limited samples, the statistical uncertainty on the uncertainty is quoted [63].

Jet bin	UEPS unc (%)	Modelling unc (%)	PDF unc (%)	QCD scale unc (%)
1	2.6	1.9	0.7	3.7
≥ 2	1.7 ± 6.9	3.5 ± 7.0	0.6	4.8

Z/DY background

For the high mass analysis the Z/DY background is estimated purely by MC predictions since the contribution is negligible. In the 2 jet $ee + \mu\mu$ high mass signal region a 15 % uncertainty is applied to the normalization. The uncertainty is based on the total relative theoretical uncertainty from the measurement of Z+2 jets cross section in high m_{jj} [81]. For the low mass analysis a total theoretical uncertainty of 21 % for $Z/\gamma^* \to \tau\tau$ in $N_{\mathrm{jets}} = 0$ has been estimated and 12 % for $Z/\gamma^* \to \tau\tau$ in $N_{\mathrm{jets}} = 1$ [66]. For $Z/\gamma^* \to ee/\mu\mu$ a total uncertainty (including theory) on the estimated background yield B_{DY} is found to be 49 % for the 0 jet category and 45 % in the $N_{\mathrm{jets}} = 1$ bin.

other di-boson production

Theoretical uncertainties for non-WW processes are dominated by the scale uncertainty in each jet bin. The uncertainties for the $W\gamma$ background have been obtained using MCFM [60] following the procedure described in Ref. [82]. For the 0 jet bin the uncertainty is 11 %, 53 % for 1 jet category and 100 % for the $\geq$ 2 jet case [66]. For the $W\gamma^*$ and WZ processes correction factors on the cross section for those processes were obtained with MCFM. The correction factors are 0.85 ± 0.09 for 0 jet,1.03 ± 0.32 for 1 jet and 1.9 ± 0.5 for $\geq$ 2 jet. The uncertainties on the correction factors correspond to QCD scale uncertainties. The contribution from ZZ and $Z\gamma$ events is relatively small hence no theoretical uncertainty is assigned to those processes [66].

W+jets & QCD estimation

The extrapolation factor or fake factor for the W+jet and QCD data-driven background estimation is determined in data and in MC. For the fake factor determined from MC, Z+jets samples as well as W+jets samples are used. The comparison of the MC samples is used to determine an uncertainty on the fake factor. For the Z+jets and W+jets control sample Powheg+Pythia8, Alpgen+Pythia6 and Alpgen+Herwig are used. The total systematic uncertainty on the fake factor varies from 29 % to 61 % for anti-identified electrons (depending on the anti-identified object p_{T}) and from 25 % to 46 % for anti-identified muons (see Figure 7.9) [66].

ggF and VBF signal

The uncertainty on the perturbative calculation of the production cross section for the Higgs signal is one of the leading uncertainties on the measurement of the signal strength μ. For the gluon-gluon-fusion process the total uncertainty is about 10 % with approximately equal contributions from QCD scale variations (7.5 %) and PDF modeling (7.2 %) for a 125 GeV Higgs [66]. For the VBF signal the contribution to the theoretical uncertainty from QCD scale variations is found to be negligible. The PDF modeling uncertainty is evaluated to be 2.7 %. The total acceptance uncertainty for cut-based analyses for a 125 GeV VBF produced Higgs is about 2.4 % [66]. Detailed information on the methodology of the evaluation on the theoretical uncertainties for the perturbative cross section calculation as well as detailed listing of the uncertainties for various Higgs masses can be found in Ref. [59].

Furthermore, an uncertainty on the jet multiplicity distribution is obtained using the jet-veto efficiency (JVE) method for ggF [83]. The uncertainties on the JVE for $N_{\mathrm{jets}} = 0$ are found to be 14 %. In the $N_{\mathrm{jets}} = 1$ case the uncertainty is 24 % from the JVE. The total contribution to a measurement of the signal strength for a Higgs with a mass of $\approx 125\,\mathrm{GeV}$ is $\approx 5\,\%$ from the jet-veto efficiency [66]. For a Higgs boson with a mass of 600 GeV the JVE uncertainty is 38 % for $N_{\mathrm{jets}} = 0$ and 42 % for $N_{\mathrm{jets}} = 1$. For a 1 TeV Higgs signal these uncertainties are 55 % for $N_{\mathrm{jets}} = 0$ and 46 % for $N_{\mathrm{jets}} = 1$.

For the SM-like signal processes with masses above a mass of $m_H \geq 400\,\text{GeV}$,[3] an additional uncertainty on the interference weighting is introduced. This uncertainty is determined for the ggF processes via the rescaling of the interference weights from LO to NNLO. A more detailed description can be found in Ref. [59]. For VBF the the uncertainty was obtained from the REPOPLO tool. It allows to generate matrix elements for signal processes with and without the interference applied. More details can be found Ref. [59]. In Figure 4.1 one can see the size of uncertainty on the interference weighting for a 400 GeV, 700 GeV and 1 TeV SM-like Higgs.

8.6. Summary

This section gives a brief overview of the total uncertainty on the signal and background event yields. All systematic variations have been applied one by one and the full object and event selection has been re-analyzed to determine the uncertainty for each variation. All uncertainties have been added up in quadrature. In Table 8.4 the uncertainties on the total background event yield for the combined DF+SF event yield are shown.

analysis	0 jet	1 jet	2 jet
low mass DF+SF	$3418 \pm 12(\text{stat.})^{+117}_{-95}(\text{syst.})$	$1429 \pm 7(\text{stat.})^{+37}_{-53}(\text{syst.})$	-
high mass DF+SF	$699 \pm 4(\text{stat.})^{+26}_{-26}(\text{syst.})$	$1026 \pm 6(\text{stat.})^{+40}_{-37}(\text{syst.})$	$53.3 \pm 2.4(\text{stat.})^{+11.9}_{-10.5}(\text{syst.})$

Table 8.4.: Total uncertainties on the total background yield for the low- and high mass analysis. The event yields and uncertainties for the $e\mu + \mu e$ events and $ee + \mu\mu$ events are combined.

In the low mass 0 jet analysis $238.6 \pm 0.7(\text{stat.})^{+42.9}_{-43.3}(\text{syst.})$ are expected from a 125 GeV Standard Model Higgs bosons. For the 1 jet category in the low mass analysis the expectation is $110.4 \pm 0.6(\text{stat.})^{+41.3}_{-41.1}(\text{syst.})$.

In chapter 9 the statistical treatment of the results will be presented. In the likelihood fit the signal strength parameter μ is determined which maximizes the numerator of eq. (9.3). The uncertainty on the fitted signal strength parameter μ depends on the mass m_H of the signal. In the following Tables the top 5 uncertainties on the fitted μ will be presented[4]. Table 8.5 summarizes the impact of the uncertainties on μ for the low mass analysis for a Higgs boson with a mass of 125 GeV.

[3] The lineshape for those processes is described by a complex pole scheme.

[4] μ is obtained from the combination of all signal regions: SF+DF $\times$ 0 jet, 1 jet and ≥ 2 jets.

Source of uncertainty	$\frac{\Delta\mu}{\mu}$ +	-
WW generator modeling	5 %	5 %
QCD scale uncertainty on the total ggF Higgs signal cross section ($m_H = 125\,\text{GeV}$)	5 %	4 %
top quark generator modeling	2.8 %	2.8 %
Fake factor for muons	2.8 %	1.9 %
Fake factor for electrons	2.8 %	1.9 %

Table 8.5.: Impact on the fitted signal strength parameter μ from the top 5 systematic uncertainties in the low mass analysis for a 125 GeV Higgs Boson. The signal strength parameter μ is determined from all signal regions (SF+DF, 0 jet, 1 jet, 2 jet).

Table 8.6 shows the impact of the uncertainties on μ for a SM-like Higgs boson signal with a mass of 300 GeV, in Table 8.7 the impact on μ is shown for a SM-like Higgs boson with a mass of 600 GeV and Table 8.8 summarizes the impact of the uncertainties on μ for 900 GeV SM-like Higgs boson. For all presented mass points more than two theory uncertainties are within the top 5 uncertainties on the measured signal strength parameter μ. Hence the $H \to WW^{(*)} \to \ell\nu\ell\nu$ analyses are supposed to be precision measurements of the Standard Model of particle physics, especially the low mass analysis.

Source of uncertainty	$\frac{\Delta\mu}{\mu}$ +	-
WW generator modeling	12 %	12 %
b-tagging eigenvector 6	6 %	7 %
QCD scale uncertainty on the total ggF Higgs signal cross section ($m_H = 300\,\text{GeV}$)	8 %	5 %
Underlying event and parton showering for WW	6 %	6 %
top quark generator modeling	6 %	5 %

Table 8.6.: Impact on the fitted signal strength parameter μ from the top 5 systematic uncertainties in the high mass analysis for a 300 GeV Higgs Boson. The signal strength parameter μ is determined from all signal regions (SF+DF, 0 jet, 1 jet and $\geq$ 2 jet).

Source of uncertainty	$\frac{\Delta\mu}{\mu}$ +	-
Interference between signal and $gg \to WW$	12 %	5 %
WW generator modeling	8 %	7 %
QCD scale uncertainty on ggF Higgs + 2 jets inclusive signal cross section ($m_H = 600\,\text{GeV}$)	9 %	3 %
QCD scale uncertainty on ggF Higgs + 0 jets inclusive signal cross section ($m_H = 600\,\text{GeV}$)	9 %	3 %
b-tagging eigenvector 6	4 %	7 %

Table 8.7.: Impact on the fitted signal strength parameter μ from the top 5 systematic uncertainties in the high mass analysis for a 600 GeV Higgs Boson. The signal strength parameter μ is determined from all signal regions (SF+DF, 0 jet, 1 jet and ≥ 2 jet).

Source of uncertainty	$\frac{\Delta\mu}{\mu}$ +	-
Interference between signal and $gg \to WW$	18 %	1.8 %
JES uncertainty η intercalibration	9 %	9 %
QCD scale uncertainty on the $qq \to VV + 2\,\text{jets}$ cross section	8 %	8 %
WW generator modeling	8 %	5 %
uncertainty on the integrated luminosity	9 %	4 %

Table 8.8.: Impact on the fitted signal strength parameter μ from the top 5 systematic uncertainties in the high mass analysis for a 900 GeV Higgs Boson. The signal strength parameter μ is determined from all signal regions (SF+DF, 0 jet, 1 jet and ≥ 2 jet).

9. Statistical treatment

To extract the results of the low- and high mass analysis a maximum likelihood fit is used. For the low mass 0 and 1 jet category as well as for the high mass 0, 1 and ≥ 2 jet category the transverse mass m_{T} is used in the fit while for the low mass ≥ 2 jet category the BDT score (see section 6.4.1) is used instead. The methodology of the fit is the same for the low and high mass analysis, with some specific differences depending on the mass region. Those differences will be discussed briefly only where it is necessary.

The signal m_{T} distribution for the high mass signal becomes quite broad with the increasing width of the Higgs signal. The background peaks at rather low m_{T} (see Figure 6.14, 6.15 and 6.16). If those m_{T} distributions are used directly in the fit, the fit would suffer from low background MC statistics in the high m_{T} regions. Due to this consideration, the m_{T} distributions in the signal regions are mapped in such a way that the signal is distributed uniformly over the full m_{T} range. The number of bins of the mapped m_{T} distribution is fixed to 10 bins for the $N_{\mathrm{jets}} = 0$ category, 6 bins for the $N_{\mathrm{jets}} = 1$ case and 4 bins for the $N_{\mathrm{jets}} \geq 2$ category. The number of bins are limited by available MC statistics and are based on the experience from earlier publications (see Ref. [73] and Ref. [72]). In the Figures 9.1-9.3 the remapped m_{T} distribution for a 300 GeV, 600 GeV and 1 TeV SM-like Higgs are shown for the ee and $e\mu$ final state. The mapping is performed individually for each lepton flavor and jet multiplicity.

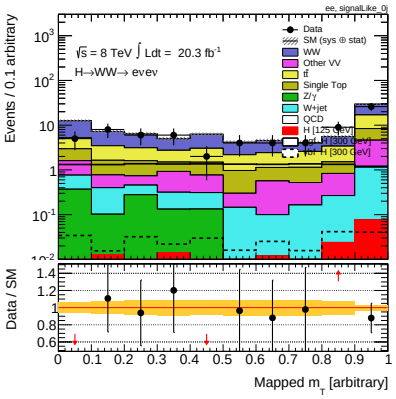

remapped m_{T} for a 300 GeV SM-like Higgs in the ee final state, 0 jet category

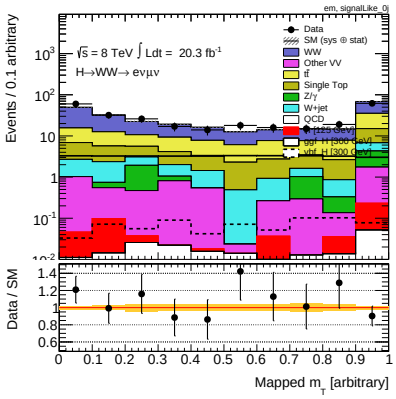

remapped m_{T} for a 300 GeV SM-like Higgs in the $e\mu$ final state, 0 jet category

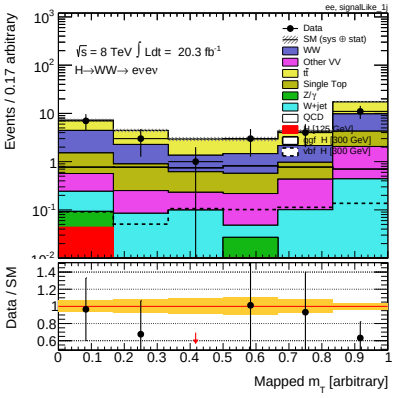

remapped m_{T} for a 300 GeV SM-like Higgs in the ee final state, 1 jet category

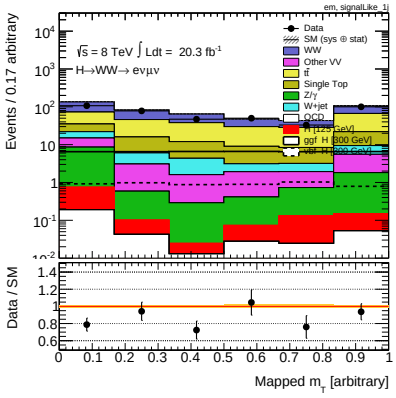

remapped m_{T} for a 300 GeV SM-like Higgs in the $e\mu$ final state, 1 jet category

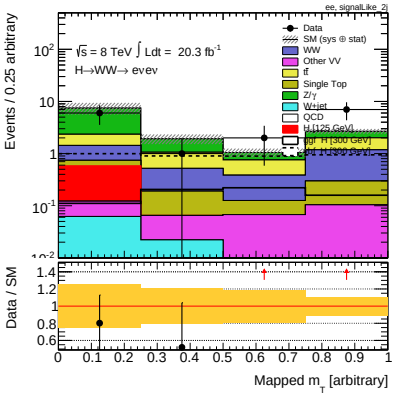

remapped m_{T} for a 300 GeV SM-like Higgs in the ee final state, 2 jet category

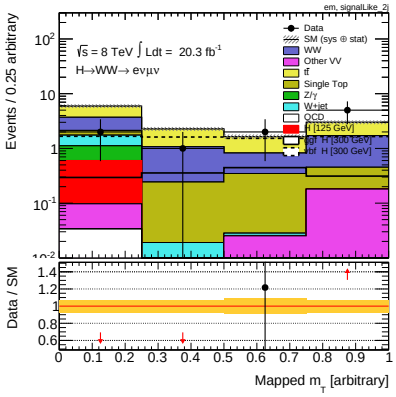

remapped m_{T} for a 300 GeV SM-like Higgs in the $e\mu$ final state, 2 jet category

Figure 9.1.: The distributions show the remapped m_{T} distribution for a 300 GeV SM-like Higgs in 0, 1 and ≥ 2 jet signal region. The left plots are the remapped m_{T} distributions in the ee final state, the right plots correspond to the $e\mu$ final state.

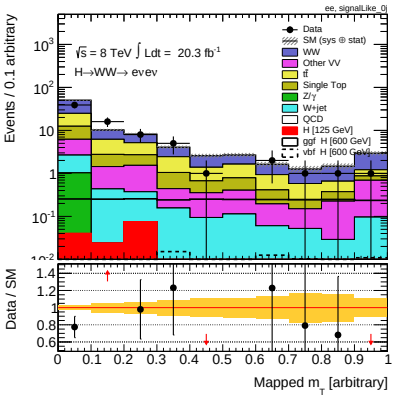

remapped m_{T} for a 600 GeV SM-like Higgs in the ee final state, 0 jet category

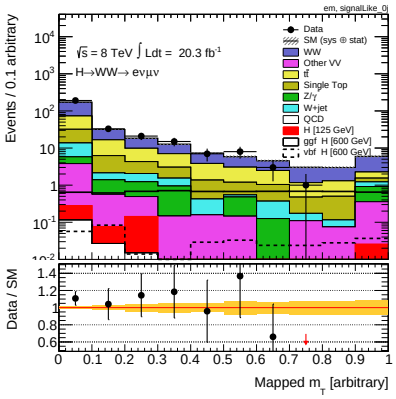

remapped m_{T} for a 600 GeV SM-like Higgs in the $e\mu$ final state, 0 jet category

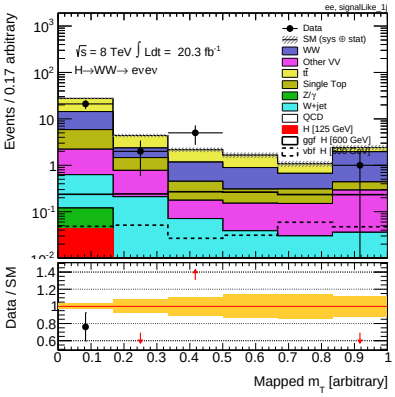

remapped m_{T} for a 600 GeV SM-like Higgs in the ee final state, 1 jet category

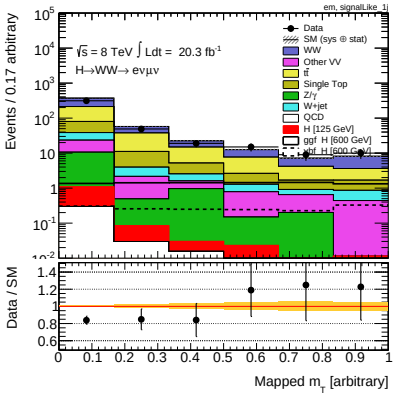

remapped m_{T} for a 600 GeV SM-like Higgs in the $e\mu$ final state, 1 jet category

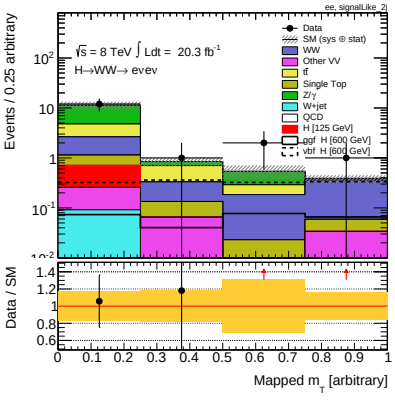

remapped m_{T} for a 600 GeV SM-like Higgs in the ee final state, 2 jet category

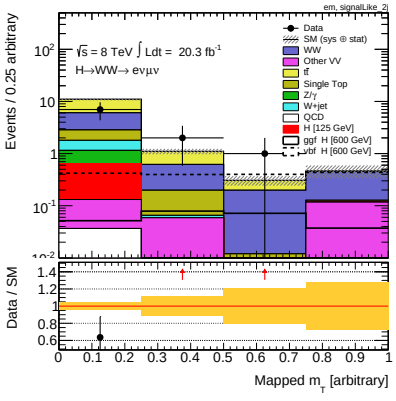

remapped m_{T} for a 600 GeV SM-like Higgs in the $e\mu$ final state, 2 jet category

Figure 9.2.: The distributions show the remapped m_{T} distribution for a 600 GeV SM-like Higgs in 0, 1 and ≥ 2 jet signal region. The left plots are the remapped m_{T} distributions in the ee final state, the right plots correspond to the $e\mu$ final state.

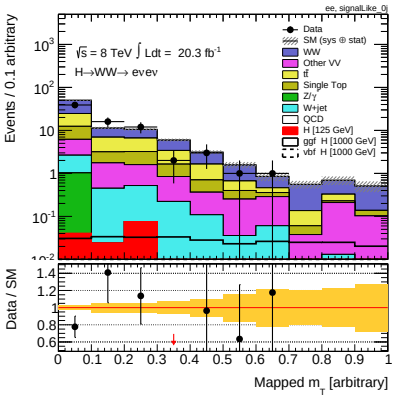

remapped m_{T} for a 1000 GeV SM-like Higgs in the ee final state, 0 jet category

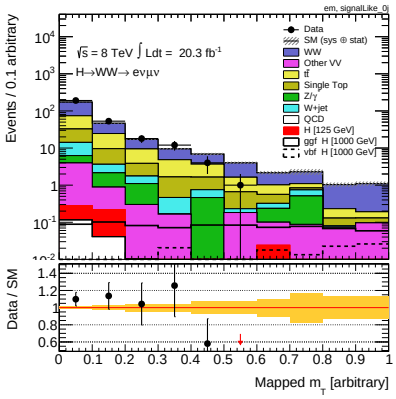

remapped m_{T} for a 1000 GeV SM-like Higgs in the $e\mu$ final state, 0 jet category

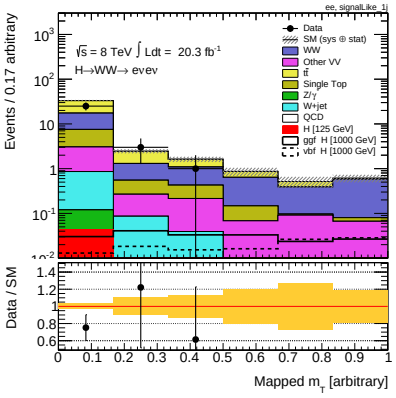

remapped m_{T} for a 1000 GeV SM-like Higgs in the ee final state, 1 jet category

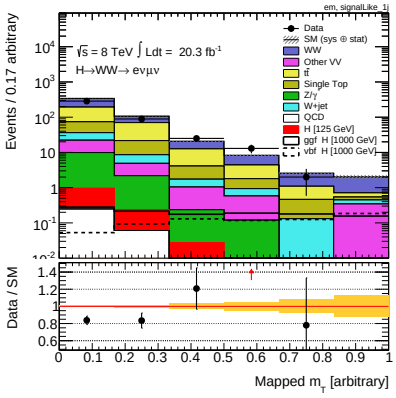

remapped m_{T} for a 1000 GeV SM-like Higgs in the $e\mu$ final state, 1 jet category

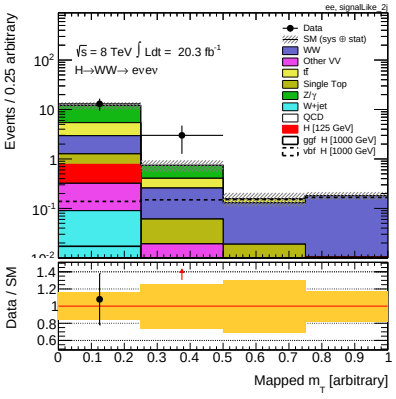

remapped m_{T} for a 1000 GeV SM-like Higgs in the ee final state, 2 jet category

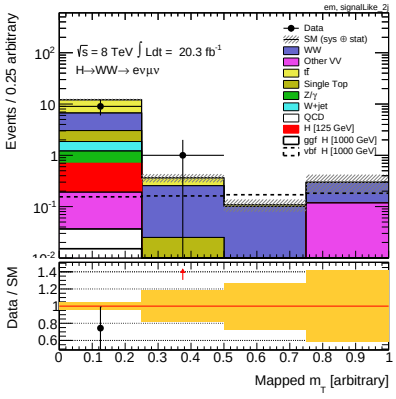

remapped m_{T} for a 1000 GeV SM-like Higgs in the $e\mu$ final state, 2 jet category

Figure 9.3.: The distributions show the remapped m_{T} distribution for a 1000 GeV SM-like Higgs in 0, 1 and ≥ 2 jet signal region. The left plots are the remapped m_{T} distributions in the ee final state, the right plots correspond to the $e\mu$ final state.

In the fit, extrapolation factors (normalization factors NF) from the control regions to the signal regions are used for the backgrounds in order to describe the fitted background rates in the signal region. Moreover, among the various control regions the background rates are extrapolated. For a single m_{T} bin in a given final state (e.g. lepton flavor and jet multiplicity) the likelihood can be written as a product of conditional Poisson probabilities $P(N|\mu)$ [1]:

$$\mathcal{L}(\mu, \mu_B) = P(N|\mu \cdot S + \mu_b \cdot b_{\mathrm{SR}}^{\mathrm{exp}}) \times P(M|\mu_b \cdot b_{\mathrm{CR}}^{\mathrm{exp}}), \tag{9.1}$$

where $b_{\mathrm{CR}}^{\mathrm{exp}}$ is the expected background yield in the control region, $b_{\mathrm{SR}}^{\mathrm{exp}}$ the expected background yield in the signal region, S the expected yield of signal events in the signal region, μ is the signal strength parameter and μ_b the signal strength parameter for the background b.

For the high mass analysis the background treated in this way is the top background for $N_{\mathrm{jets}} = 1$ and $N_{\mathrm{jets}} \geq 2$ and the WW background for $N_{\mathrm{jets}} = 0$ and $N_{\mathrm{jets}} = 1$. In the low mass analysis the Drell-Yan and the non-WW background is also treated in this way for both 0 and 1 jet. The full likelihood can be written as:

$$\mathcal{L}(\mu, \vec{\theta}) = \{ \prod_{k=e\mu,\mu e,ee,\mu\mu} \prod_{j=0}^{N_{\mathrm{jets}}} \prod_{i=1}^{N_{\mathrm{bins}}} P(N_{ijk}|\mu \cdot S_{ijk} + \sum_{m}^{N_{\mathrm{bg}}} b_{ijk})\} \times \{\prod_{i=1}^{N_\theta} N(\tilde{\theta}|\theta)\}, \tag{9.2}$$

which contains a product over the m_{T} bins, a product over lepton flavor and a product over the jets in the final state. The background yields b_{ijk} are scaled by response functions ν which depend on the nuisance parameters θ. The final term $\prod_{i=1}^{N_\theta} N(\tilde{\theta}|\theta)$ is the product over the nuisance parameters (NP). The NP correspond to the various systematic variations and the background estimations in the control regions of the analysis, the collection of the nuisance parameters is represented by $\vec{\theta}$. The nuisance parameters are divided into four categories:

1. **Flat systematics:** Systematics which do not affect the shape of the m_{T} distribution (like the 2.8 % uncertainty on the luminosity, see section 8.4) take the form $\nu_{\mathrm{flat}}(\theta) = k^\theta$. The parameter k is determined via a measurement of $\nu_{\mathrm{flat}}(\theta)$ at $\theta = \pm 1$. For such uncertainties the constraint term on θ present in the likelihood is unit Gaussian and k^θ is log-normally distributed [63].

2. **Shape systematics:** In the case of systematics affecting the shape of m_{T} (like lepton uncertainties, see section 8.1), the systematic is separated into a shape component and a flat component in such a way that the pure shape component has no influence on the event yields. The flat component is then treated as summarized above. The shape part is assumed to be distributed like a truncated Gaussian. In

[1] $P(N|\mu) = \frac{\mu^N e^{-\mu}}{N!}$

practice, the uncertainty takes the form $\nu_{\text{shape}}(\theta) = 1 + \epsilon \cdot \theta$, where ϵ is again determined like k (see type 1). The constraint on θ is a unit Gaussian again. The truncation of the shape part Gaussian is imposed in such a way that $\nu_{\text{shape}}(\theta < \frac{-1}{\epsilon}) = 0$. Some systematics can have both a shape component and a normalization component (type 1). For such systematics the same nuisance parameter θ is shared between $\nu_{\text{flat}}(\theta)$ and $\nu_{\text{shape}}(\theta)$ [63].

3. **Statistical uncertainties:** Those uncertainties arise from MC statistics or data-driven methods. The constraint on θ for such uncertainties is described by the Poisson probability $P(\tilde{\theta}|\theta\gamma)$ for an auxiliary measurement of number of events $\tilde{\theta}$. For an uncertainty σ_{b_0} on the expectation of background events b_0 the auxiliary measured events $\tilde{\theta}$ can be expressed as $\tilde{\theta} = \gamma = \frac{b_0^2}{\sigma_{b_0}^2}$ and the form of systematics can be expressed as $\nu_{\text{stat}}(\theta) = \theta$ [63].

4. **Background control regions:** From the high-statistics data control regions (see chapter 7), which are used to constrain the normalization of certain backgrounds, uncertainties can arise which are similar to the type 3 systematics. A slightly different methodology is applied to properly take the contamination from other backgrounds and from signal in the control regions into account. The constraint on such θ is again a Poisson probability $P(\tilde{\theta}|\gamma(\theta))$ where $\tilde{\theta}$ are the observed events in the CR. The expectation value of the Poisson $\gamma(\theta)$ is $\mu \cdot s + \theta \cdot b_{\text{target}} + \sum_i^{N_{\text{bg}}-1} b_i$. The number b_{target} is the background in question for a specific CR [63].

A single nuisance parameter can affect multiple background rates as well as signal rates. Some nuisance parameters are specific to certain physics processes (like the theoretical uncertainties for specific processes, see section 8.5). The normalization of individual backgrounds dominates the shape variation of m_{T} since individual backgrounds are not equally distributed over the full m_{T} spectrum.

To obtain the results like the 95 % confidence level (C.L.) exclusion limits, a modified frequentist method known as the CL_s method [84], [85] is used. In the CL_s method the ratio of the profiled likelihoods is used to test a certain hypothesis on μ:

$$q(\mu) = -2 \cdot \ln \left. \frac{\mathcal{L}(\mu, \vec{\theta})}{\mathcal{L}(\hat{\mu}, \hat{\hat{\vec{\theta}}})} \right|_{\vec{\theta}=\hat{\vec{\theta}}} \tag{9.3}$$

where $\hat{\hat{\vec{\theta}}}$ and $\hat{\mu}$ are the values of $\vec{\theta}$ and μ that maximize $\mathcal{L}$. The numerator of Eqn. 9.3 depends on μ only since $\vec{\theta}$ takes the value that maximizes $\mathcal{L}$ for a given value μ. The level of agreement of a given hypothesis on μ and the data is quantified by the p_0 value. The p_0 value integrates all values of $q(\mu)$ which are equal or less compatible with the

observed value of $q(\mu)_{\text{Obs.}}$:

$$p_0 = \int_{q(\mu)_{\text{Obs.}}}^{\infty} f(q(\mu)|\mu)\ \mathrm{d}q(\mu), \tag{9.4}$$

where $f(q(\mu)|\mu)$ represents the probability density function (pdf) under a given assumption on μ. In practice, the pdf for a given hypothesis on μ is obtained using Monte Carlo pseudo-experiments.

Part III.

Results

10. Results of the low mass analysis

The low mass analysis is designed to measure the signal strength and the couplings of the resonance around 125 GeV. Over the last years the signal region definitions, the background treatment and estimation as well as the fit procedure have been optimized in order to be able to perform a high precision measurement. In the following, the results obtained via the statistical treatment introduced in chapter 9 for the low mass analysis will be presented and discussed. In all results presented for the low mass analysis, the measurements in the 0 and the 1 jet signal region as well as the 2 jet VBF category are exploited and both the 2011 $\sqrt{s} = 7\,\text{TeV}$ and the 2012 $\sqrt{s} = 8\,\text{TeV}$ datasets are incorporated (see chapter 4). All results presented in this chapter are published in Ref. [70].

10.1. Signal strength

The test statistic $q(\mu)$ defined in equation 9.4 is used to quantify the agreement of the observed data, the background only hypothesis and the background plus signal hypothesis. As signal a Standard Model Higgs boson with a mass of $114\,\text{GeV} < m_H \leq 200\,\text{GeV}$ is assumed. The probability that the background fluctuates to reproduce the observed data is expressed via the p_0 value which is computed using $q(\mu)$ with $\mu = 0$. In Figure 10.1 the p_0 value as a function of m_H is shown. A broad minimum around 125 GeV can be seen where the broadness of the curve reflects the rather poor mass resolution of the $H \to WW^{(*)} \to \ell\nu\ell\nu$ analysis. The absolute minimum of the p_0 value is found at $m_\text{H} = 130\,\text{GeV}$, which corresponds to an observed 6.1σ significance. Owing to the fact that the ATLAS $H \to ZZ \to 4\ell$ and $H \to \gamma\gamma$ analyses have measured the mass of the resonance to be $125.36 \pm 0.41\,\text{GeV}$ all results of the low mass analysis are quoted for this mass. The observed significance for $125.36\,\text{GeV}$ is also 6.1σ and the expected significance for $m_\text{H} = 125.36\,\text{GeV}$ is 5.7σ.

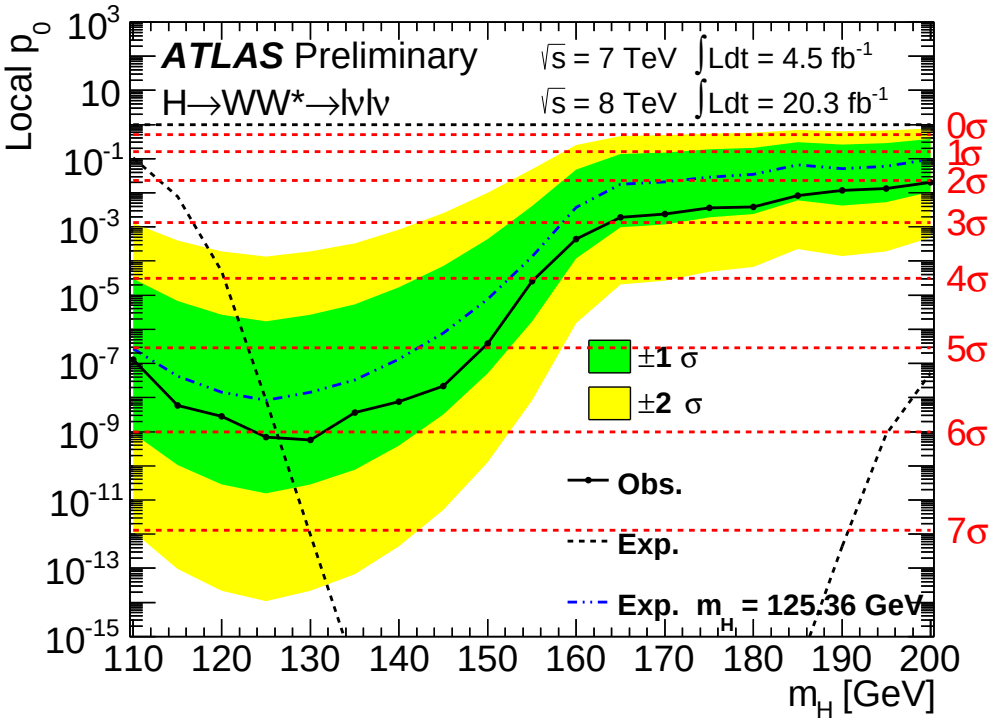

Figure 10.1.: Local p_0 as a function of m_{H}. The measurements of the 0, 1 and 2 jet category are exploited and both the 2011 and 2012 dataset is incorporated. The black dashed curve shows the expected p_0 value at each mass hypothesis m_{H}. The dashed blue curve labeled "Exp. $m_{\mathrm{H}} = 125.36\,\mathrm{GeV}$" shows the expected p_0 value given the presence of a signal arising from a Higgs boson with a mass of $m_{\mathrm{H}} = 125.36\,\mathrm{GeV}$.

The observed significance of 6.1σ establishes a discovery of the $H \to WW^{(*)} \to \ell\nu\ell\nu$ signal. In the left plot of Figure 10.2 the observed signal strength μ is shown as a function of m_{H}. The signal strength μ represents the ratio of observed production cross section times branching ratio over the theoretical prediction of the product of production cross section and branching ratio. The observed μ is compatible with zero for masses $m_{\mathrm{H}} > 160\,\mathrm{GeV}$ and shows a sharp increase to a value of one at $m_{\mathrm{H}} \approx 125\,\mathrm{GeV}$. The increase of μ for small m_{H} can be interpreted by the presence of a $H \to WW^{(*)} \to \ell\nu\ell\nu$ signal arising from a Higgs boson with a mass of $m_{\mathrm{H}} = 125.36\,\mathrm{GeV}$. Moreover, is the increase at small m_{H} caused by the relatively poor mass resolution of the $H \to WW^{(*)} \to \ell\nu\ell\nu$ analysis. The dependence of μ on the mass hypothesis m_{H} reflects the branching ratio (see Figure 2.2) of a Standard Model Higgs boson to decay into two W bosons. The right plot in Figure 10.2 shows the negative log-likelihood as a function of μ and m_{H} where the point $(\mu = 1, m_{\mathrm{H}} = 125.36\,\mathrm{GeV})$ lies well within the 68 % C.L. contour which can be interpreted as a good agreement between the prediction by the Standard Model and the observed data.

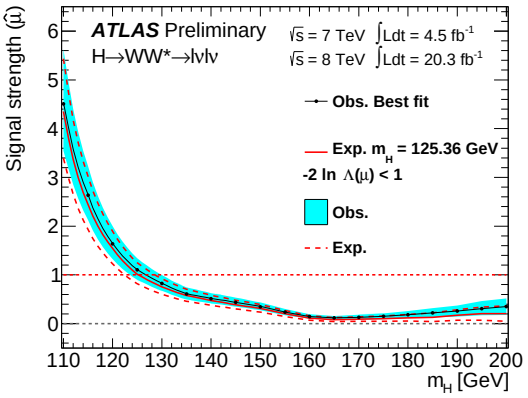

The plots shows the signal strength μ as a function of the mass hypothesis m_{H}. The solid black curve represents the observed data, the red dashed line shows the expectation on μ for a Standard Model Higgs boson for each mass hypothesis and the red solid line shows the expected signal strength for a signal arising from a Standard Model Higgs boson with a mass of $m_{\mathrm{H}} = 125.36\,\mathrm{GeV}$.

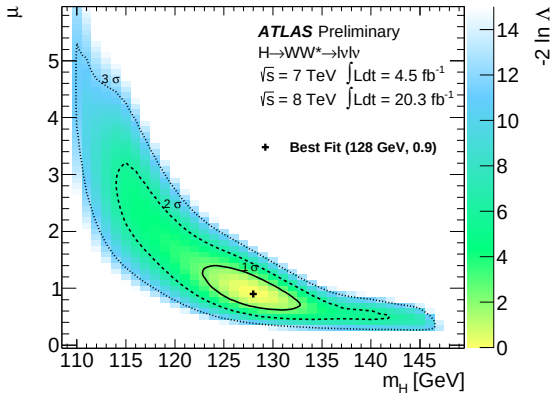

Negative log-likelihood contour as a function of the signal strength μ and the mass hypothesis m_{H}.

Figure 10.2.: Signal strength μ as a function of m_{H}.

The signal strength parameter μ can be used to exploit the signal strength of the inclusive signal strength as well as the signal strength of individual production mechanisms. To measure the signal strength of the individual production mechanisms, μ_{ggF} for the gluon fusion production and μ_{VBF} for the vector boson fusion, one of the two is profiled[1] (for example μ_{VBF} gets profiled to measure μ_{ggF} and vice versa) while the other signal strength parameter can run free in the likelihood fit. Moreover, the background contributions in the likelihood fit are profiled to the expectation in the signal regions while the extrapolation factors from the various control regions are applied. The Standard Model predictions of the ggF and VBF production cross section for Higgs bosons with a mass of $m_{\mathrm{H}} = 125.36\,\mathrm{GeV}$ are assumed. In the left plot of Figure 10.3 a likelihood scan as a function of μ_{ggF} and μ_{VBF} is shown for a mass hypothesis of $m_{\mathrm{H}} = 125.36\,\mathrm{GeV}$. The minimum of the likelihood scan yields the value of μ to be

$$\begin{aligned} \mu &= 1.08\,^{+0.16}_{+0.15}(\mathrm{stat.})\,^{+0.16}_{-0.14}(\mathrm{syst.}) \\ \mu &= 1.08\,^{+0.22}_{+0.20} \end{aligned} \tag{10.1}$$

while the signal strength of the individual production mechanisms are measured to be

[1] Profiling a parameter in the likelihood represents the procedure of reducing the number of free parameters in minimization of the likelihood.

$$\begin{aligned} \mu_{\mathrm{ggF}} &= 1.01 \pm 0.19(\mathrm{stat.})\,^{+0.19}_{-0.16}(\mathrm{syst.}) \\ \mu_{\mathrm{VBF}} &= 1.28\,^{+0.44}_{-0.40}(\mathrm{stat.})\,^{+0.29}_{-0.20}(\mathrm{syst.}). \end{aligned} \tag{10.2}$$

The measured values of μ_{ggF} and μ_{VBF} can be used to test the agreement of the couplings of the Higgs boson to fermions and (vector) bosons with the SM predictions.

10.2. Couplings scaling factors

A parametrization is used where a scaling factor κ_F is introduced for the couplings to fermions and a scaling factor κ_V for the couplings to bosons. In the Standard Model case, both scaling factors yield a value of one. The scaling of the branching fraction of the Higgs boson to decay into two W bosons is subsequently parametrized in a way that it is proportional to κ_V^2 and inversely proportional to a linear combination of κ_F^2 and κ_V^2 where the latter term represents the dependence of the total branching ratio on the scaling of the couplings. More details of the parametrization of the couplings used can be found in Ref. [59]. The right plot in Figure 10.3 shows the likelihood scan as a function of κ_V and κ_F. The obtained best fit value yields the following values of the scaling factors:

$$\begin{aligned} \kappa_F &= 0.92\,^{+0.30}_{-0.23} \\ \kappa_V &= 1.04\,^{+0.10}_{-0.11}, \end{aligned} \tag{10.3}$$

which shows a good agreement of the observed data and the predicted couplings of the Standard Model Higgs boson. Exploiting the couplings at high precision can help in the search for new physics beyond the Standard Model which might have a relatively small impact on the couplings of the Higgs boson.

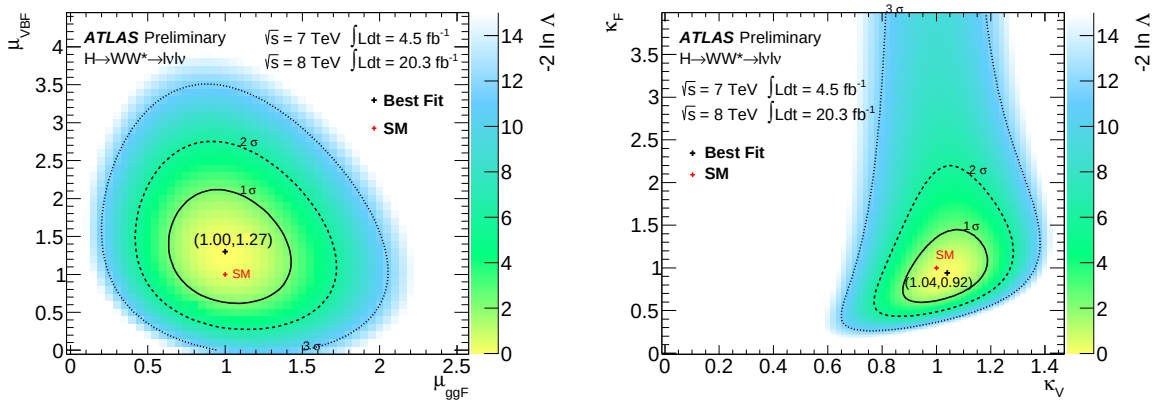

The plot shows the negative log-likelihood scan as a function of μ_{ggF} and μ_{VBF}. The 1, 2 and 3 standard deviation contours are shown.

Negative log-likelihood scan as a function of κ_V and κ_F. The 1, 2 and 3 standard deviation contours are shown.

Figure 10.3.: Likelihood scans as a function of μ_{ggF} and μ_{VBF} and as a function of κ_V and κ_F.

10.3. Exclusion limits

As mentioned earlier, the low mass analysis has been optimized for a Higgs boson with a mass of 125 GeV. Due to the comparably poor mass resolution in the $H \to WW^{(*)} \to \ell\nu\ell\nu$ channel, the analysis is sensitive up to (SM) Higgs boson masses of ≈ 200 GeV. Hence exclusion limits are obtained in the mass range $110\,\mathrm{GeV} \leq m_{\mathrm{H}} \leq 200\,\mathrm{GeV}$ for a SM Higgs. The modified frequentist method $\mathrm{CL_S}$ [84], [85] is used to determine exclusion limits where a given SM Higgs mass is excluded at 95 % C.L. if the value $\mu = 1$ is excluded at that mass hypothesis. The exclusion limits obtained in the low mass analysis are presented in Figure 10.4 where it is expected to exclude a SM Higgs down to 114 GeV. The observed limit excludes a SM Higgs in the mass range $132\,\mathrm{GeV} < m_{\mathrm{H}} < 200\,\mathrm{GeV}$. The clear access of the observed exclusion over the expected exclusion limit curve, can be interpreted via the presence of a signal arising from a Higgs with a mass of 125.36 GeV. The broadness of the access is a result of the low mass resolution in the $H \to WW^{(*)} \to \ell\nu\ell\nu$ channel.

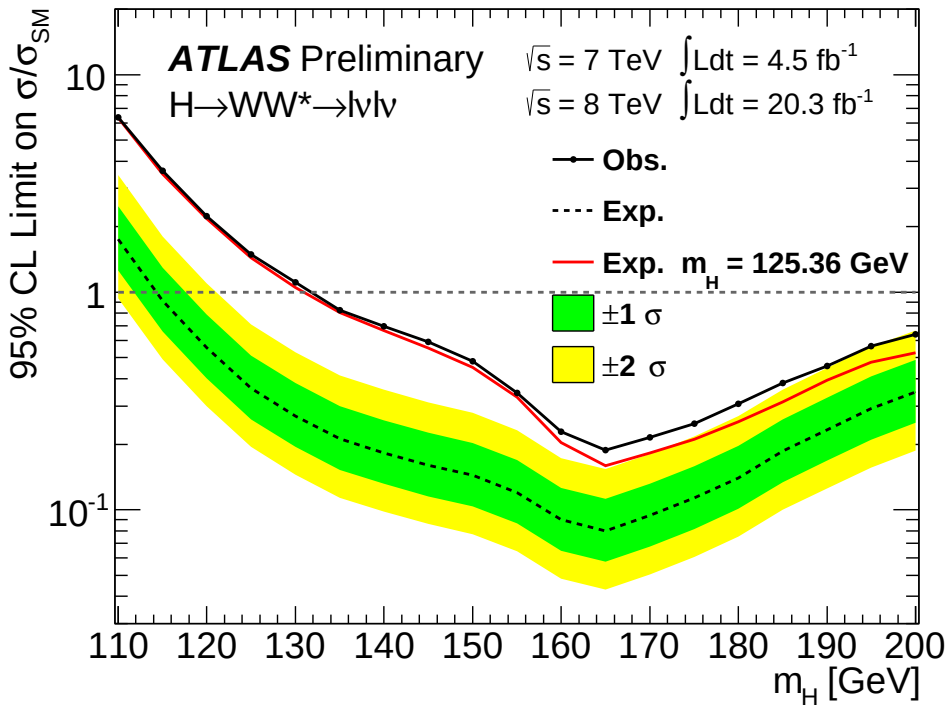

Figure 10.4.: CL_S exclusion limits obtained from the low mass analysis. The solid black line represents the observed exclusion limit and the dashed black line represents the expected exclusion limit. The yellow (green) bands around the expected limit represent the 2 (1) σ uncertainties on the expected value. The solid red line corresponds to the expected exclusion limit given the presence of a SM Higgs with a mass of 125.36 GeV.

11. Results of the high mass analysis

The high mass analysis is designed to search for new physics beyond the Standard Model. As shown in section 6.4.2 no excess in the observed data over the background expectation is seen. Therefore, upper limits on the signal strength as well as on the production cross section times branching ratio at the 95 % confidence level (C.L.) using the CL_S are derived for the following scenarios: Additional Standard Model Higgs (SM-like), the narrow width approximation (NWA) and the real electroweak single scenario (EWS). The results for the high mass analysis are obtained from the 2012 dataset only. All results of the high mass analysis can be found in Ref. [63].

11.1. Exclusion limits for the SM-like scenario

In Figure 11.1 the exclusion limits on the signal strength μ for a SM-like Higgs boson are shown separately for the ggF category (Fig. 11.1a), the VBF (Fig. 11.1b) category and the combination of both (Fig. 11.1c). To obtain the limits for the ggF (VBF) production mechanism separately, the signal-strength parameter for VBF (ggF) is profiled to a value of $\mu = 1$ and the signal arising from the VBF (ggF) production is treated as a background. In each of the presented results of the high mass analysis, all high mass signal regions are incorporated (see section 6.4.2). The slight lack of data for the ggF limits as presented in Fig. 11.1a (also visible in Fig. 6.14b) has been studied in detail and was found to be a statistical downward fluctuation of data in the different flavor, 0 jet category. The observed limit agrees with the expected limit over the full mass range at the 2σ level. A SM-like Higgs boson with a mass of $m_H \leq 661\,\text{GeV}$ can be excluded at 95 % confidence level and no statistical significant excess was found.

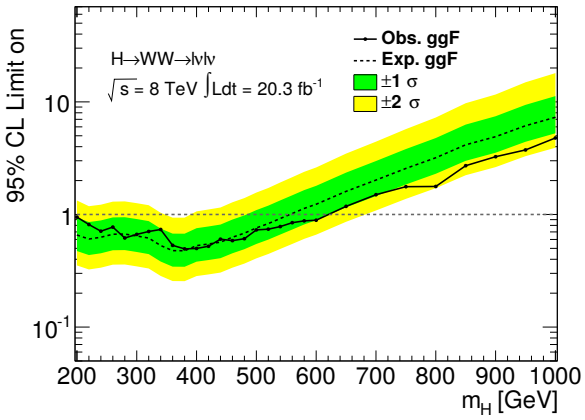

Limits on μ for a SM-like Higgs in the ggF category.

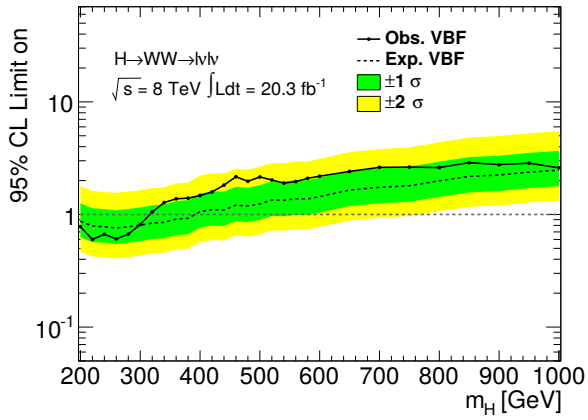

Limits on μ for a SM-like Higgs in the VBF category.

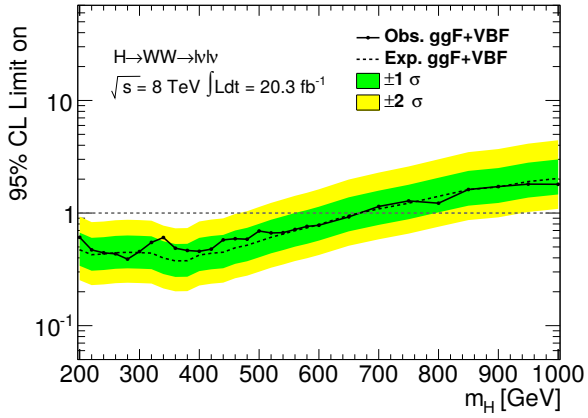

Limits on μ for a SM-like Higgs for the combination of the ggF and VBF category.

Figure 11.1.: The plots show the 95 % C.L. upper limits on μ for a SM-like Higgs separately for the ggF category, the VBF category and the combination of both. The dashed black line represents the expected values, the solid black line represents the observed limits. The yellow (green) bands around the expected limit represent the 2 (1) σ uncertainties on the expected value.

The limits on the signal strength μ for the SM-like scenario can be interpreted in a different way given that the signal strength μ represents the ratio of production cross sections $\frac{\sigma}{\sigma_{\text{Th.}}}$ where $\sigma_{\text{Th.}}$ is the theoretical value predicted by the SM. Multiplying the limit on μ with the theoretical value of the production cross section times branching ratio of the SM-like signal processes, allows to put upper limits on the Higgs boson production cross section times branching ratio. In Figure 11.2 the obtained limits on the Higgs boson production cross section times branching ratio are presented for the ggF

category (Fig. 11.2a), the VBF category (Fig 11.2b) and for the combination of both categories (Fig 11.2c). The theoretical prediction of the Higgs boson production cross section times the branching ratio is shown as a blue line with the corresponding $\pm 1\sigma$ uncertainties.

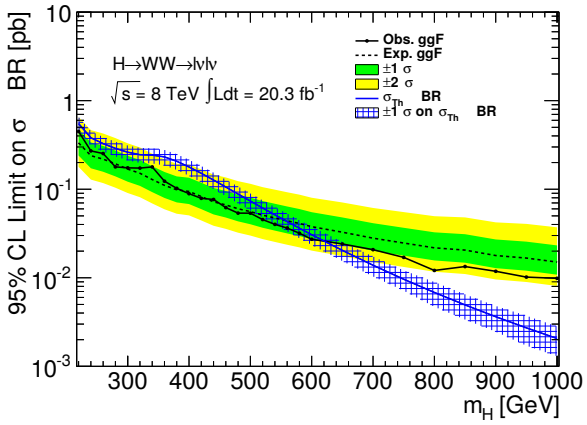

Limits on the Higgs boson production cross section times branching ratio for a SM-like Higgs in the ggF category.

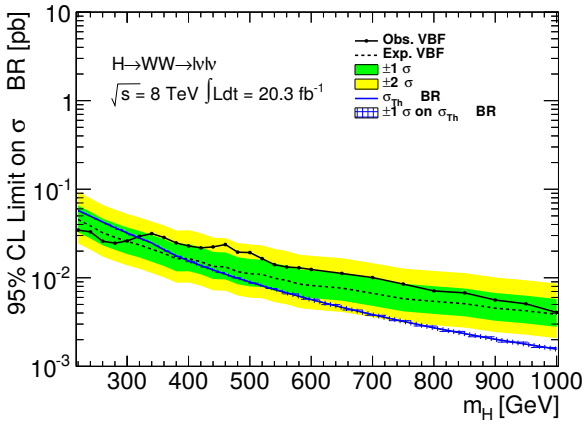

Limits on the Higgs boson production cross section times branching ratio for a SM-like Higgs in the VBF category.

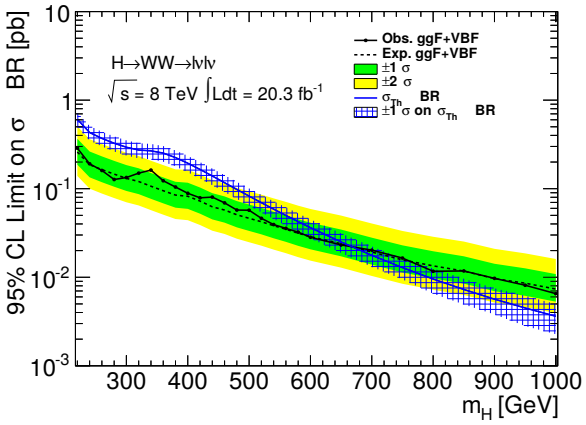

Limits on the Higgs boson production cross section times branching ratio for a SM-like Higgs for the combination of the ggF and VBF category.

Figure 11.2.: The plots show the 95 % C.L. upper limits on Higgs boson production cross section for a SM-like Higgs separately for the ggF category, the VBF category and the combination of both. The dashed black line represents the expected values, the solid black line represents the observed limits. The yellow (green) bands around the expected limit represent the 2 (1) σ uncertainties on the expected value. The theoretical cross predicted by the SM times the branching ratio is shown as a blue line.

11.2. Exclusion limits for the NWA scenario

In the NWA scenario, only the limits on the Higgs-like production cross section times branching ratio are shown and no combination of the ggF and VBF category is performed. The latter is because the scaling of the couplings to fermions and to bosons from a NWA Higgs-like boson are not predicted by the SM. A combination of the ggF and VBF category would assume a certain value of the scaling. The branching ratios of the NWA Higgs-like boson are assumed to be the same as for the SM Higgs boson. A NWA Higgs-like boson is searched in the region $200\,\text{GeV} \leq m_{\text{H}}^{\text{NWA}} \leq 2\,\text{TeV}$. In Figure 11.3 the upper limits on the production cross section times branching ratio for a NWA Higgs-like boson are presented separately for the ggF and the VBF category. No statistical significant excess of the observed limit over the expected limit was found. The slight lack of data present in both the ggF and VBF category was analyzed and found to be a statistical downward fluctuation of data. The sharp rise of the observed limits at around $m_{\text{H}}^{\text{NWA}} = 1.6\,\text{TeV}$, present in both the ggF and VBF category was also found to be a statistical fluctuation of data.

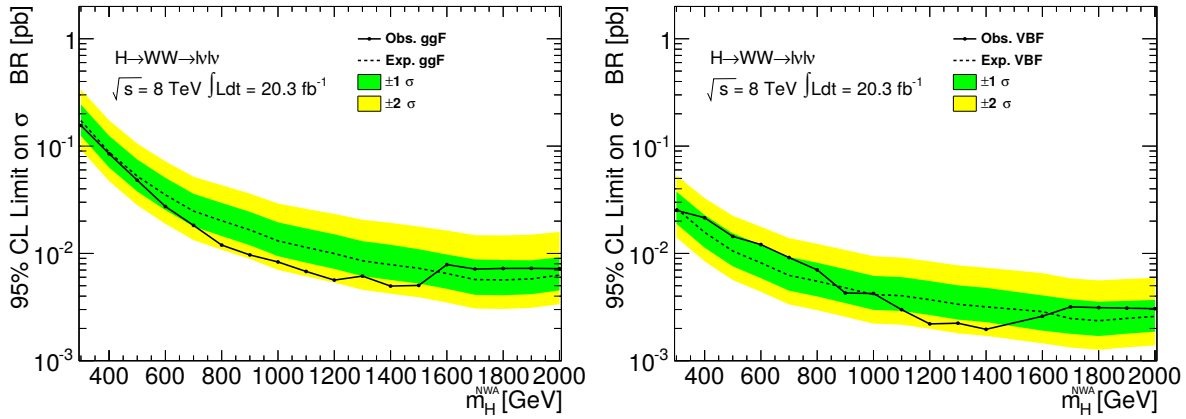

Limits on the NWA Higgs-like boson production cross section times branching ratio in the ggF category.

Limits on the NWA Higgs-like boson production cross section times branching ratio in the VBF category.

Figure 11.3.: The plots show the 95 % C.L. upper limits on the NWA Higgs-like boson production cross section times branching ratio separately for the ggF category and the VBF category. The dashed black line represents the expected values, the solid black line represents the observed limits. The yellow (green) bands around the expected limit represent the 2 (1) σ uncertainties on the expected value.

In Table 11.1 the 95 % upper limits on $\sigma \cdot \text{BR}$ are presented for $m_H^{\text{NWA}} = 300\,\text{GeV}$, 600 GeV, 900 GeV, 1.2 TeV, 1.6 TeV and 2 TeV separately for the ggF and VBF cate-

gories.

Table 11.1.: 95% C.L. upper limits on the production cross section times branching ratio corresponding to several Higgs mass hypotheses, when the Higgs has a narrow lineshape.

m_H^{NWA} (GeV)	300	600	900	1200	1600	2000
	$\sigma \cdot \mathrm{BR}$ (fb)					
ggF	156	27.3	9.68	5.64	7.87	7.21
VBF	25.2	12.1	4.28	2.20	2.60	2.59

11.3. Exclusion limits for the EWS scenario

The electroweak singlet scenario is introduced in section 2.4. The limits are obtained as a function of m_h and got evaluated for the width range $0.2 \cdot \Gamma_{\mathrm{SM}} \leq \Gamma_h \leq 1.0 \cdot \Gamma_{\mathrm{SM}}$ with a step size of 0.2. The additional branching ratio of the heavy scalar resonance $\mathrm{BR}_{h,\mathrm{new}}$ is assumed to be equal to zero. The ggF and VBF categories got combined, which is valid since the scaling parameter κ is known. In Figure 11.4 the upper limits on the production cross section times branching ratio are shown for the additional electroweak singlet Higgs-like bosons h, for five different width scenarios. No statistical significant excess of the observed limit over the expected limit was found. The observed limit agrees with the expected limit at the 1σ level over the full mass range.

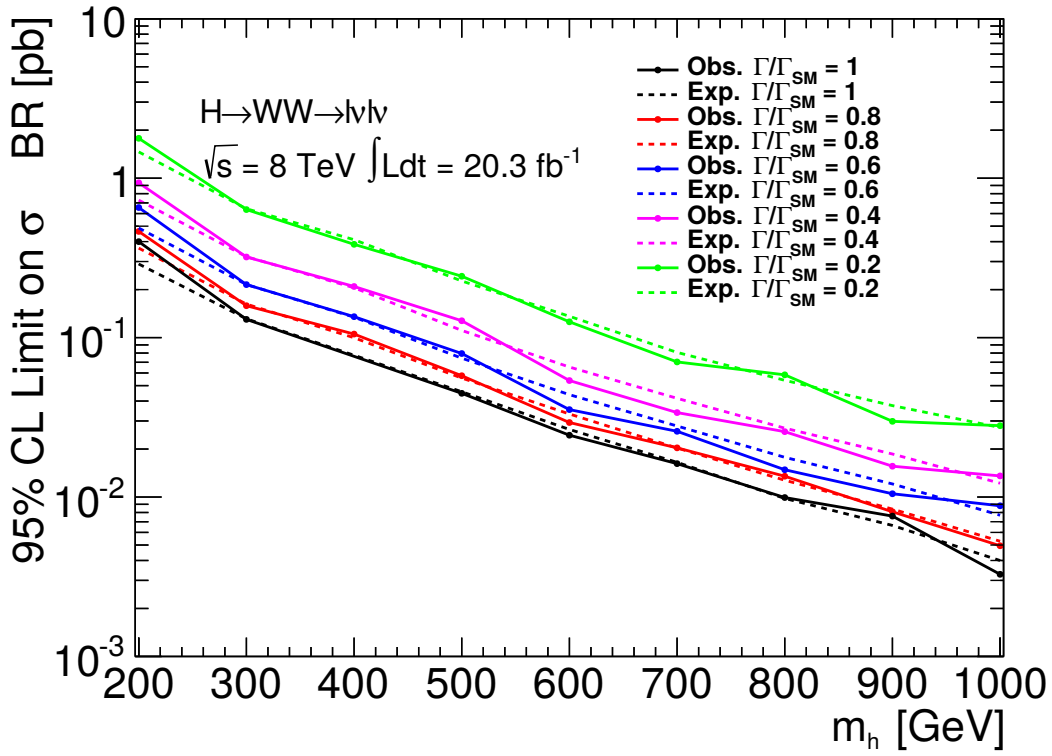

Figure 11.4.: The plots show the 95 % C.L. upper limits on EWS Higgs boson production cross section. The dashed, colored lines represent the expected limit while the solid, colored lines represent the observed limit.

12. Summary and outlook

After a century-long pursuit, a resonance at $\approx 125\,\text{GeV}$ was detected which is to this day in agreement with the predictions of the Standard Model Higgs boson. The subsequent detailed measurements of the properties of this new state increased the probability that the new resonance is indeed the long sought Higgs boson.

This thesis presents the measurement of the fermionic and bosonic couplings of the Higgs boson via the $H \to WW^{(*)} \to \ell\nu\ell\nu$ decay channel as well as the search for heavier Higgs like particles in the same decay channel. Data driven estimations of the various Standard Model background processes are used to minimize the dependence on generator modeling of the background processes. A cut based approach is used to define signal regions from which the signal strength and coupling scaling factors for the resonance at $\approx 125\,\text{GeV}$ are obtained. Furthermore, signal regions are defined using also a cut based approach, in order to obtain exclusion limits for scenarios with heavier, Higgs like particles. A signal strength μ of

$$\begin{aligned} \mu &= 1.08\,^{+0.16}_{+0.15}(\text{stat.})\,^{+0.16}_{-0.14}(\text{syst.}) \\ \mu &= 1.08\,^{+0.22}_{+0.20} \end{aligned} \tag{12.1}$$

could be measured for a resonance at $m_{\text{H}} = 125.36 \pm 0.41\,\text{GeV}$ with the signal strengths of the individual dominant production mechanisms

$$\begin{aligned} \mu_{\text{ggF}} &= 1.01 \pm 0.19(\text{stat.})\,^{+0.19}_{-0.16}(\text{syst.}) \\ \mu_{\text{VBF}} &= 1.28\,^{+0.44}_{-0.40}(\text{stat.})\,^{+0.29}_{-0.20}(\text{syst.}). \end{aligned} \tag{12.2}$$

Figure 12.1 shows the measured signal strength of the $H \to WW^{(*)} \to \ell\nu\ell\nu$ decay channel in comparison with the $H \to \gamma\gamma$, $H \to ZZ \to 4\ell$, $VH \to b\bar{b}$ and the $H \to \tau\tau$ analysis. The individual decay channels show a good agreement with the SM predictions and no clear trend is observed.

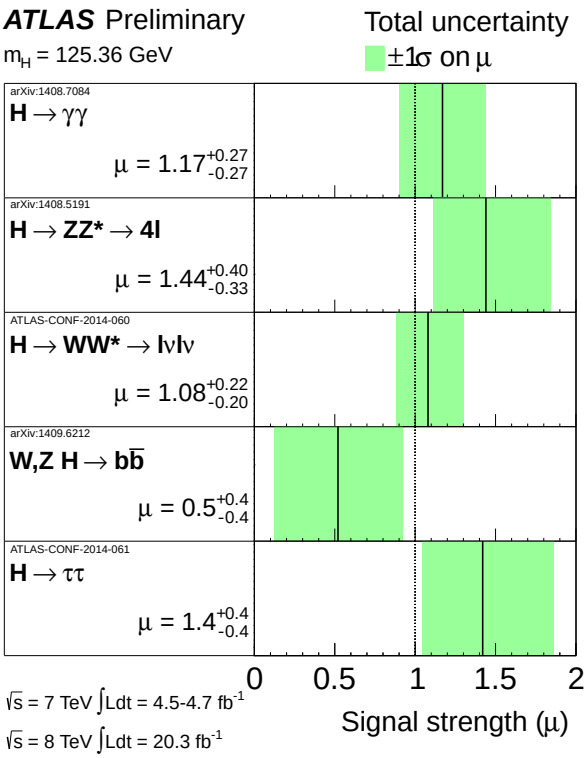

Figure 12.1.: Signal strengths of individual Higgs boson decay channels measured with the ATLAS data. The results of the individual decay channels are published in the references quoted within the plot [86].

The signal strength parameter of the individual production mechanisms μ_{ggF} and μ_{VBF} can be utilized to measure the scaling of the couplings of the SM Higgs boson to fermions and bosons. The measured values are

$$\begin{aligned} \kappa_F &= 0.92\,^{+0.30}_{-0.23} \\ \kappa_V &= 1.04\,^{+0.10}_{-0.11}, \end{aligned} \tag{12.3}$$

which shows also a good agreement of the data and the SM predictions.

The observation of the $H \to WW^{(*)} \to \ell\nu\ell\nu$ signal with a statistical significance of 6.1σ combined with the good agreement of the measured signal strengths and couplings scaling factors κ with the SM predictions, confirm the presence of the SM Higgs boson.

The $H \to WW^{(*)} \to \ell\nu\ell\nu$ decay channel is very well suited for the search of heavier Higgs like particles under the assumption that the branching ratio of a new, heavier state shows a similar distribution as for the SM Higgs. The total decay width Γ of such a heavier Higgs like state is a free parameter in the search for heavy Higgs like bosons. Upper limits on the production cross section times branching ratio have been derived for three

different scenarios.

In the electro weak singlet (EWS) scenario, the SM Higgs sector is incorporated and a real electroweak singlet is added to the theory. A EWS Higgs was searched in the mass range $200\,\text{GeV} \leq m_\text{H} \leq 1\,\text{TeV}$ while the decay width of the signal was varied from $0.2 \cdot \Gamma_\text{SM} \leq \Gamma \leq 1.0 \cdot \Gamma_\text{SM}$ with Γ_SM being the decay width of a SM like Higgs with mass m_H. No statistically significant excess of the data over the expectation has been observed.

In order to perform a model independent search, a hypothetical, additional Higgs with a fixed decay width of $\Gamma_\text{NWA} = 1\,\text{GeV}$ was searched in the mass range $200\,\text{GeV} \leq m_\text{H} \leq 2\,\text{TeV}$ an no statistical significant excess could be seen over the full mass range. As a third test, a Higgs boson with a width and lineshape of a SM Higgs was searched in the mass range $200\,\text{GeV} \leq m_\text{H} \leq 1\,\text{TeV}$ and also in this search no statistical significant excess of the data over the expectation has been observed. Moreover, a SM-like Higgs could be excluded up to a mass of $m_\text{H} = 661\,\text{GeV}$. The absence of any evidence of additional Higgs like particles confirm the predictions of the Standard Model.

The search for CP-even high mass states will be one of the main tasks during the second run (Run 2) of the LHC with a center of mass energy of $\sqrt{s} = 13\,\text{TeV}$. It is expected that the sensitivity for masses $m_\text{H} \geq 1\,\text{TeV}$ during Run 1 as presented in this thesis, is overtaken with $6-7\,\text{fb}^{-1}$ at $\sqrt{s} = 13\,\text{TeV}$ [87]. Figure 11.3 shows the upper limits on the product of production cross and branching ratio for a Higgs like particle with a decay width of 1 GeV. The sensitivity of the presented analysis does not get worse at the 2 TeV scale hence the search for a NWA Higgs could be extended to 3 TeV or more.

Over the last years a *very* complex analysis framework has been developed in a team of ≥ 30 scientists from all around the globe, which allowed it to observe the decay of a Standard Model Higgs boson with a mass of $m_\text{H} = 125.36\,\text{GeV}$ into two W bosons, which subsequently both decay into a lepton neutrino pair. The sensitivity of the coupling measurements of the SM Higgs boson in $H \to WW^{(*)} \to \ell\nu\ell\nu$ decays is (also) limited by theoretical uncertainties hence further exploiting those observables can help to achieve a better understanding of nature.

Part IV.

Appendix

Bibliography

[1] Georges Aad et al. Observation of a new particle in the search for the Standard Model Higgs boson with the ATLAS detector at the LHC. *Phys.Lett.*, B716:1–29, 2012.

[2] Serguei Chatrchyan et al. Observation of a new boson at a mass of 125 GeV with the CMS experiment at the LHC. *Phys.Lett.*, B716:30–61, 2012.

[3] Georges Aad et al. Evidence for the spin-0 nature of the Higgs boson using ATLAS data. *Phys.Lett.*, B726:120–144, 2013.

[4] CMS Collaboration. Study of the Mass and Spin-Parity of the Higgs Boson Candidate via Its Decays to Z Boson Pairs. On the mass and spin-parity of the Higgs boson candidate via its decays to Z boson pairs. *Phys. Rev. Lett.*, 110(arXiv:1212.6639. CMS-HIG-12-041. CERN-PH-EP-2012-372):081803. 25 p, Dec 2012. Comments: Submitted to Phys. Rev. Lett. Final version.

[5] Georges Aad et al. Measurement of the Higgs boson mass from the $H \to \gamma\gamma$ and $H \to ZZ^* \to 4\ell$ channels with the ATLAS detector using 25 fb^{-1} of pp collision data. *Phys.Rev.*, D90:052004, 2014.

[6] Precise determination of the mass of the Higgs boson and studies of the compatibility of its couplings with the standard model. Technical Report CMS-PAS-HIG-14-009, CERN, Geneva, 2014.

[7] Georges Aad et al. Measurements of Higgs boson production and couplings in diboson final states with the ATLAS detector at the LHC. *Phys.Lett.*, B726:88–119, 2013.

[8] S.L. Glashow. Partial Symmetries of Weak Interactions. *Nucl.Phys.*, 22:579–588, 1961.

[9] J.R. Oppenheimer, M. Gell-Mann, J. Schwinger, J. Tiomno, J.M. Cassels, et al. Strange particles and weak interactions. pages IX.1–52.

[10] Steven Weinberg. A model of leptons. *Phys. Rev. Lett.*, 19:1264–1266, Nov 1967.

[11] David J. Gross and Frank Wilczek. Ultraviolet behavior of non-abelian gauge theories. *Phys. Rev. Lett.*, 30:1343–1346, Jun 1973.

[12] H. David Politzer. Reliable perturbative results for strong interactions? *Phys. Rev. Lett.*, 30:1346–1349, Jun 1973.

[13] Cliff Burgess. *The Standard Model: A Primer*. Cambride University Press, 2007.

[14] A. Einstein. Zur allgemeinen relativitẗstheorie. *Ständiger Beobachter der Preussischen Akademie der Wissenschaften*, pages 778–786, 799–801, 1915.

[15] M. Gell-Mann. The interpretation of the new particles as displaced charge multiplets. *Nuovo Cim.*, 4(S2):848–866, 1956.

[16] Kazuhiko Nishijima. Charge independence theory of v particles. *Progress of Theoretical Physics*, 13(3):285–304, 1955.

[17] K.A. Olive et al. *Particle Data Group*, volume 38. 2014.

[18] Nobel Media AB 2014. The nobel prize in physics 2013, url: `http://www.nobelprize.org/nobel_prizes/physics/laureates/2013/`, October 2014.

[19] F. Englert and R. Brout. Broken Symmetry and the Mass of Gauge Vector Mesons. *Physical Review Letters*, 13:321–323, August 1964.

[20] P. W. Higgs. Broken Symmetries and the Masses of Gauge Bosons. *Physical Review Letters*, 13:508–509, October 1964.

[21] S Dittmaier and C et al. Mariotti. *Handbook of LHC Higgs Cross Sections: 1. Inclusive Observables*. CERN, Geneva, 2011. Comments: 153 pages, 43 figures, to be submitted to CERN Report. Working Group web page: https://twiki.cern.ch/twiki/bin/view/LHCPhysics/CrossSections.

[22] Durham University. The durham hepdata project, url: `http://hepdata.cedar.ac.uk/pdf/pdf3.html`, October 2014.

[23] Csaba Csaki. The Minimal supersymmetric standard model (MSSM). *Mod.Phys.Lett.*, A11:599, 1996.

[24] HSG6 working group. Benchmarks for heavy higgs boson searches in the electroweak bosons decay channels in the atlas detector. Technical Report ATL-COM-PHYS-2014-258, CERN, Geneva, May 2014.

[25] A. Hill and J.J. van der Bij. STRONGLY INTERACTING SINGLET - DOUBLET HIGGS MODEL. *Phys.Rev.*, D36:3463–3473, 1987.

[26] R. Bouamrane. Radiative corrections to ww scattering in the standard model. 233:533–542, 1990.

[27] T Binoth and J J Bij. Influence of strongly coupled, hidden scalars on Higgs signals. Technical Report hep-ph/9608245. FREIBURG-THEP-96-15, Freiburg Univ. Inst. Theor. Phys., Freiburg im Breisgau, Aug 1996.

[28] I. Belikov. Physics of the ALICE experiment. 2006.

[29] Monica Pepe Altarelli and Frederic Teubert. *B* Physics at LHCb. *Int.J.Mod.Phys.*, A23:5117–5136, 2008.

[30] S. Redaelli. The operation of the lhc accelerator complex, Apr 2010.

[31] Christiane Lefevre. The CERN accelerator complex. Complexe des accélérateurs du CERN. Dec 2008.

[32] Lyndon Evans and Philip Bryant. LHC Machine. *Journal of Instrumentation*, 3(08):S08001, 2008.

[33] The ATLAS Collaboration. The atlas experiment at the cern large hadron collider. *Journal of Instrumentation*, 3(08):S08003, 2008.

[34] *ATLAS detector and physics performance: Technical Design Report, 1.* Technical Design Report ATLAS. CERN, Geneva, 1999. Electronic version not available.

[35] J Mitrevski. Electron and Photon Reconstruction with the ATLAS Detector. Technical Report ATL-PHYS-PROC-2014-189, CERN, Geneva, Oct 2014.

[36] Expected electron performance in the ATLAS experiment. Technical Report ATL-PHYS-PUB-2011-006, CERN, Geneva, Apr 2011.

[37] Muon reconstruction efficiency in reprocessed 2010 LHC proton-proton collision data recorded with the ATLAS detector. Technical Report ATLAS-CONF-2011-063, CERN, Geneva, Apr 2011.

[38] Matteo Cacciari, Gavin P. Salam, and Gregory Soyez. The Anti-k(t) jet clustering algorithm. *JHEP*, 0804:063, 2008.

[39] Jet energy measurement with the atlas detector in proton-proton collisions at a center of mass energy of 7TeV. *The European Physical Journal C*, 73(3), 2013.

[40] M. Lichtnecker. *Determination of α_s via the Differential 2-Jet-Rate with ATLAS at LHC*. Ludwig-Maximilians-Univeristät München, 2011.

[41] I Bird, P Buncic, F Carminati, M Cattaneo, P Clarke, I Fisk, M Girone, J Harvey, B Kersevan, P Mato, R Mount, and B Panzer-Steindel. Update of the Computing Models of the WLCG and the LHC Experiments. Technical Report CERN-LHCC-2014-014. LCG-TDR-002, CERN, Geneva, Apr 2014.

[42] Performance of the ATLAS Electron and Photon Trigger in p-p Collisions at sqrts = 7 TeV in 2011. Technical Report ATLAS-CONF-2012-048, CERN, Geneva, May 2012.

[43] HWW HSG3. Object Selections in the H →WW(*) analysis with 20.3 fb-1 of data collected with the ATLAS detector at $\sqrt{s} = 8$ TeV. Technical Report ATL-COM-PHYS-2013-1504, CERN, Geneva, Nov 2013.

[44] T. Binoth, M. Ciccolini, N. Kauer, and M. Kramer. Gluon-induced W-boson pair production at the LHC. *JHEP*, 0612:046, 2006.

[45] G. Corcella, I.G. Knowles, G. Marchesini, S. Moretti, K. Odagiri, et al. HERWIG 6: An Event generator for hadron emission reactions with interfering gluons (including supersymmetric processes). *JHEP*, 0101:010, 2001.

[46] Torbjorn Sjostrand, Leif Lonnblad, and Stephen Mrenna. PYTHIA 6.2: Physics and manual. 2001.

[47] Torbjorn Sjostrand, Stefan Ask, Jesper R. Christiansen, Richard Corke, Nishita Desai, et al. An Introduction to PYTHIA 8.2. 2014.

[48] Michelangelo L. Mangano, Mauro Moretti, Fulvio Piccinini, Roberto Pittau, and Antonio D. Polosa. ALPGEN, a generator for hard multiparton processes in hadronic collisions. *JHEP*, 0307:001, 2003.

[49] Borut Paul Kersevan and Elzbieta Richter-Was. The Monte Carlo event generator AcerMC versions 2.0 to 3.8 with interfaces to PYTHIA 6.4, HERWIG 6.5 and ARIADNE 4.1. *Comput.Phys.Commun.*, 184:919–985, 2013.

[50] T. Gleisberg, Stefan. Hoeche, F. Krauss, M. Schonherr, S. Schumann, et al. Event generation with SHERPA 1.1. *JHEP*, 0902:007, 2009.

[51] Stefano Frixione, Paolo Nason, and Carlo Oleari. Matching NLO QCD computations with Parton Shower simulations: the POWHEG method. *JHEP*, 0711:070, 2007.

[52] T. Binoth, N. Kauer, and P. Mertsch. Gluon-induced QCD corrections to pp → ZZ → l anti-l l-prime anti-l-prime. page 142, 2008.

[53] S. Agostinelli et al. GEANT4: A Simulation toolkit. *Nucl.Instrum.Meth.*, A506:250–303, 2003.

[54] Nikolas Kauer and Giampiero Passarino. Inadequacy of zero-width approximation for a light Higgs boson signal. *JHEP*, 1208:116, 2012.

[55] G.Passarino S. Goria and D.Rosco. The Higgs Boson Lineshape. 2012.

[56] Giampiero Passarino. Higgs Interference Effects in $gg \to ZZ$ and their Uncertainty. *JHEP*, 1208:146, 2012.

[57] J. Campbell, K. Ellis, and C. Williams. Vector boson pair production at the LHC. *JHEP*, 07:018, 2011.

[58] J. Campbell, K. Ellis, and C. Williams. Gluon-Gluon Contributions to W^+W^- Production and Higgs Interference Effects. *JHEP*, 1110:005, 2011.

[59] LHC Higgs Cross Section Working Group, S. Heinemeyer, C. Mariotti, G. Passarino, and R. Tanaka (Eds.). Handbook of LHC Higgs Cross Sections: 3. Higgs Properties. 2013.

[60] J. Campbell and K. Ellis. Mcfm-monte carlo for femtobarn processes. http://mcfm.fnal.gov, 2010.

[61] K. Arnold, J. Bellm, G. Bozzi, F. Campanario, C. Englert, et al. Release Note – Vbfnlo-2.6.0. 2012.

[62] K. Arnold, J. Bellm, G. Bozzi, M. Brieg, F. Campanario, et al. VBFNLO: A parton level Monte Carlo for processes with electroweak bosons – Manual for Version 2.5.0. 2011. * Temporary entry *.

[63] P Calpin, S Diglio, J Jovicevic, L Kashif, C Meineck, J Qian, R Sandstroem, T Taylor, I Tsukerman, S Wu, and Z Zhang. $H \to WW \to l\nu l\nu$ high-mass analysis with 20 fb^{-1} of data collected with the ATLAS detector at $\sqrt{s} = 8$ TeV. (ATL-COM-PHYS-2014-193), Mar 2014.

[64] Luminosity Determination in pp Collisions at sqrt(s) = 7 TeV using the ATLAS Detector in 2011. Technical Report ATLAS-CONF-2011-116, CERN, Geneva, Aug 2011.

[65] S Ask, D Malon, T Pauly, and M Shapiro. Report from the Luminosity Task

Force. Technical Report ATL-GEN-PUB-2006-002. ATL-COM-GEN-2006-003. CERN-ATL-COM-GEN-2006-003, CERN, Geneva, Jul 2006.

[66] The HSG3 Working Group. Analysis of $H \to WW \to \ell\nu\ell\nu$ ggF and VBF production modes with 20 fb^{-1} and 5 fb^{-1} of data collected with the ATLAS detector at $\sqrt{s} = 8$ and 7 TeV. Technical Report ATL-COM-PHYS-2014-466, CERN, Geneva, May 2014.

[67] J Alison, K Brendlinger, S Heim, J Kroll, and C M Lester. Description and Performance of the Electron Likelihood Tool at ATLAS using 2012 LHC Data. Technical Report ATL-COM-PHYS-2013-378, CERN, Geneva, Apr 2013.

[68] B Resende. Muon identification algorithms in ATLAS. Technical Report ATL-PHYS-PROC-2009-113, CERN, Geneva, Sep 2009.

[69] M Chelstowska, J Machado Miguens, D Schaefer, K Yoshihara, and L Yuan. Background estimation in the $H \to WW^{(*)} \to \ell\nu\ell\nu$ analysis with 20.7 fb^{-1} of data collected with the ATLAS detector at $\sqrt{s} = 8$ TeV. Technical Report ATL-COM-PHYS-2013-1630, CERN, Geneva, Dec 2013.

[70] Observation and measurement of Higgs boson decays to WW^* with ATLAS at the LHC. (ATLAS Conference Contribution, ATLAS-CONF-2014-060), Oct 2014.

[71] Data-Quality Requirements and Event Cleaning for Jets and Missing Transverse Energy Reconstruction with the ATLAS Detector in Proton-Proton Collisions at a Center-of-Mass Energy of $sqrts = 7$ TeV. Technical Report ATLAS-CONF-2010-038, CERN, Geneva, Jul 2010.

[72] Search for a high-mass Higgs boson in the $H \to WW \to l\nu l\nu$ decay channel with the ATLAS detector using 21 fb^{-1} of proton-proton collision data. Technical Report ATLAS-CONF-2013-067, CERN, Geneva, Jul 2013.

[73] Measurements of the properties of the Higgs-like boson in the $WW^{(*)} \to \ell\nu\ell\nu$ decay channel with the ATLAS detector using 25 fb^{-1} of proton-proton collision data. (ATLAS Confernce Contribution, ATLAS-CONF-2013-030), Mar 2013.

[74] I. Narsky. StatPatternRecognition: A C++ Package for Statistical Analysis of High Energy Physics Data. *arXiv:physics.data-an/0507143*, July 2005.

[75] J. Friedman and N. Fisher. Bump hunting in high dimensional data. *Statistics and Computing*, 9:123–143, 1999.

[76] I. Tsukerman. Study of kinematics in $\mu\mu$ and ee events for $H \to WW \to \ell\nu\ell\nu$

analysis in the region 200 GeV$\leq m_H \leq$ 1000 GeV. Technical Report ATL-COM-PHYS-2013-1580, ITEP, Moscow, Dec 2013.

[77] B. Mellado, X. Ruan, and Z. Zhang. Extraction of top backgrounds in the Higgs boson search with the $H \to WW^{(*)} \to \ell\ell + \not{E}_{\mathrm{T}}^{\mathrm{miss}}$ decay with a full-jet veto at the LHC. *PhysRevD*, 84(9), November 2011.

[78] Sayipjamal Dulat, Tie-Jiun Hou, Jun Gao, Joey Huston, Pavel Nadolsky, et al. Higgs Boson Cross Section from CTEQ-TEA Global Analysis. *Phys.Rev.*, D89:113002, 2014.

[79] A.D. Martin, W.J. Stirling, R.S. Thorne, and G. Watt. Parton distributions for the LHC. *Eur.Phys.J.*, C63:189–285, 2009.

[80] Richard D. Ball, Valerio Bertone, Stefano Carrazza, Christopher S. Deans, Luigi Del Debbio, et al. Parton distributions with LHC data. *Nucl.Phys.*, B867:244–289, 2013.

[81] K. Joshi E. Nurse C. Gutschow, G. Jones and A.D. Pilkington. Measurement of the electroweak z-boson plus dijet production cross section and distributions sensitive to the vector boson fusion production process in *pp* collisions at sqrts = 8 tev with the atlas detector. Technical Report ATL-COM-PHYS-2013-331, CERN, Geneva, November 2013.

[82] Iain W. Stewart and Frank J. Tackmann. Theory Uncertainties for Higgs and Other Searches Using Jet Bins. *Phys.Rev.*, D85:034011, 2012.

[83] S. Dittmaier, S. Dittmaier, C. Mariotti, G. Passarino, R. Tanaka, et al. Handbook of LHC Higgs Cross Sections: 2. Differential Distributions. 2012.

[84] G. Cowan, K. Cranmer, E. Gross, and O. Vitells. Asymptotic formulae for likelihood-based tests of new physics. *European Physical Journal C*, 71:1554, February 2011.

[85] Alexander L. Read. Presentation of search results: The CL(s) technique. *J.Phys.*, G28:2693–2704, 2002.

[86] The ATLAS collaboration. Summary plots from the atlas higgs physics group, 2014.

[87] S. Diglio. CP-even H → WW Searches for Run II, url: `https://indico.cern.ch/event/328392/other-view?view=standard`. October 2014.

Danksagung

Ich bedanke mich bei

- Prof. Dr. Dorothee Schaile für die Möglichkeit diese Dissertation in der experimentellen Teilchenphysik zu erstellen. Sowie für die Korrektur und die vielen Anregungen.

- Prof. Dr. Martin Faessler für das Erstellen des Zweitgutachtens.

- PD Dr. Johannes Elmsheuser für die vielen Ratschläge, Tipps, die Geduld und die ausgezeichnete Betreuung!

- der gesamten Higgs Gruppe des Lehrstuhls für die wöchentlichen Impulse im Higgs-Meeting

- Bonnie Chow und Friedriech Hönig für das außerordentlich gute Büroklima und für das Aushalten meines geistigen Ergusses!

- Frau Grimm-Zeidler, die bei administrativen Problemen immer eine äusserst freundliche Hilfe war.

- bei Josephine Wittkowski und Dr. Philippe Calfayan für die unvergessliche Zeit am und außerhalb des CERNs.

- der HSG3 Arbeitsgruppe des ATLAS Experiments!

- dem Rest des Lehrstuhls sowie bei einigen ehemaligen Mitgliedern für das ausgesprochen sehr gute Arbeitsklima: Dr. Stefanie Adomeit, Dr. Sebastian Becker, Katharina Behr, Michael Bender, Prof. Dr. Otmar Biebel, Dr. Jona Bortfeldt, Dr. Günter Duckeck, Dr. Julien de Graat, Nikolai Hartmann, Dr. Ralf Hertenberger, Dr. Federica Legger, Dr. Johannes Ebke, Dr. Markus Lichtnecker, Dr. Jeanette Lorenz, Thomas Maier, Dr. Alexander Mann, Dr. Michiel Sanders, Dr. Felix Rauscher, Alexander Ruschke, Balthasar Schachtner, Christopher Schmitt, Nicola Tyler, Attila Varga, Josipa Vujaklija, Dan Vladoiu, Dr. Rod Walker, Dr. Jonas Will und Dr. Andre Zibell.

- bei meiner Tante Michaela für das Korrekturlesen

- bei meiner Freundin Carina Schüle, die mir nicht nur über die letzten drei Jahre ein starker Rückhalt war und auch sonst einfach unersetzlich ist!

- und vor allem bei meinen Eltern dir mir das Studium der Physik erst ermöglichten und mich immer unterstützten. Danke!

NCSP